Filament-based Material Extrusion Additive Manufacturing of composites and ceramics

Original Citation:
Filament-based Material Extrusion Additive Manufacturing of composites and ceramics / Morfini, Luigi. - ELETTRONICO. - (2024). [10.60576/poliba/iris/morfini-luigi_phd2024]

Availability:
This version is available at http://hdl.handle.net/11589/264802 since: 2024-01-17

Published version
DOI:10.60576/poliba/iris/morfini-luigi_phd2024

Publisher: Politecnico di Bari

Department of Mechanics, Mathematics and Management

AEROSPACE SCIENCE AND ENGINEERING

Ph.D. Program

SSD: ING-IND/16–Manufacturing technology and systems

Final Dissertation

Filament-based Material Extrusion Additive Manufacturing of composites and ceramics

by

Luigi Morfini

Supervisors:

Prof. Luigi Maria Galantucci

Prof. Roberto Spina

Coordinator of Ph.D. Program:

Prof. Marco Donato De Tullio

Course n°36, 01/11/2020-31/10/2023

Department of Mechanics, Mathematics and Management

AEROSPACE SCIENCE AND ENGINEERING

Ph.D. Program

SSD: ING-IND/16–Manufacturing technology and systems

Final Dissertation

Filament-based Material Extrusion Additive Manufacturing of composites and ceramics

by

Luigi Morfini

<u>Referees:</u>

Prof. Pierpaolo Carlone

Prof. Michele Moretti

<u>Supervisors:</u>

Prof. Luigi Maria Galantucci

Prof. Roberto Spina

Coordinator of Ph.D. Program:

Prof. Marco Donato De Tullio

Course n°36, 01/11/2020-31/10/2023

ABSTRACT

This doctoral thesis explores filament-based Material Extrusion Additive Manufacturing (MEX) processes to improve mechanical and thermal properties in industrial, aerospace, and aviation components. The research uses experimental methodologies and literature analysis to explore various materials, including polymers, techno-polymers, composites, and ceramics.

The study reveals a correlation between infill percentage and layer count in polymer samples using MEX for thermal properties, and more research is needed to understand anisotropy's effect on thermal properties and surface layers.

In order to determine the impact of heat treatments on the mechanical properties, the study compares oven annealing and direct annealing methods for the mechanical characterization of PEEK material and finds that temperature is the primary determining factor. The ideal temperature is 300 degrees Celsius, with a 16% gain with oven annealing and 6% with direct annealing.

The study evaluates the tensile and flexural performance of Onyx specimens using various filling patterns and printing orientations. The gyroid-type infill yields the highest tensile strength, regardless of print orientation.

Using ceramics as a composite feedstock, the study demonstrates the use of MEX to fabricate dense zirconia components with high mechanical properties and low thermal conductivity.

The study demonstrates a strong correlation between printing parameters and material testing, which significantly improves the mechanical properties of parts produced through Material Extrusion Additive Manufacturing.

INDEX

LIST OF FIGURES

LIST OF TABLES

OVERVIEW OF THE DISSERTATION

The thesis is structured into eight chapters, with a comprehensive overview of the global context within which this research is situated being presented in this first chapter. Specifically, the technology of Material Extrusion Additive Manufacturing based on filament is described. The groundwork for understanding the significance and relevance of the subsequent research presented in this thesis is laid.

In the first chapter, an in-depth exploration of the current state of the art in optimizing process parameters to manufacture components using polymer, composite, and ceramic materials is undertaken. This critical review of existing knowledge and methodologies serves as the foundation for the research conducted in this thesis.

From chapters 2 to chapter 5, there is the core of the experimental work of this thesis.

The second chapter conducts a thorough examination of the thermal properties of polymers and how these properties are affected by changes in certain process parameters. This rigorous assessment is an important component of the whole inquiry.

The third chapter investigates the impact of thermal treatments on techno-polymers and how such treatments can improve their mechanical properties. This investigation is critical to comprehending the link between heat treatments and mechanical performance of these materials.

The fourth chapter investigates the thermal and rheological properties of fiber-reinforced engineered polymers in depth. Furthermore, the impact of process factors on the production of lightweight structures, particularly tensile and flexural mechanical characteristics, is investigated.

The fifth chapter includes a thorough examination of the complete process of manufacturing ceramic components. This includes filament research, the printing process, debinding, sintering, mechanical testing, and the creation of complicated structures. There are useful insights into the challenges of ceramic component manufacture.

The final chapter serves as a platform for reflections and ultimate conclusions drawn from the results achieved in this research. A summary of key findings and their implications is offered, bringing closure to the thesis and paving the way for future work in the field.

INTRODUCTION

Additive manufacturing, also known as 3D printing (3DP), is a revolution in contemporary production [1–3] . It works on the premise of layer-by-layer item fabrication from digital design data. This cutting-edge method brings in a fundamental shift in the way products are imagined and created, enabling the production of intricate and complex geometries like honeycombs and lattices that were previously unattainable using traditional manufacturing techniques.

Traditional manufacturing paradigms are drastically altered by 3D printing's ability to build complex geometrical structures. It enables the development of parts and goods that defy the restrictions imposed by traditional manufacturing, opening up fresh possibilities for design freedom and technological innovation. In essence, it gives designers and engineers the freedom to imagine and create items that go beyond what was previously thought to be possible.

Additionally, additive manufacturing techniques have the distinct advantage of utilizing resources efficiently. Existing items can be modified and reconfigured to be produced utilizing AM techniques with less raw material use. This sustainable feature highlights 3D printing as a key instrument in developing more environmentally friendly production techniques, which is in line with worldwide initiatives to reduce environmental effect and resource depletion. Additionally, this adaptability may improve product qualities by increasing functional attributes as well as weight reduction, ushering in a new era of product optimization and performance development.

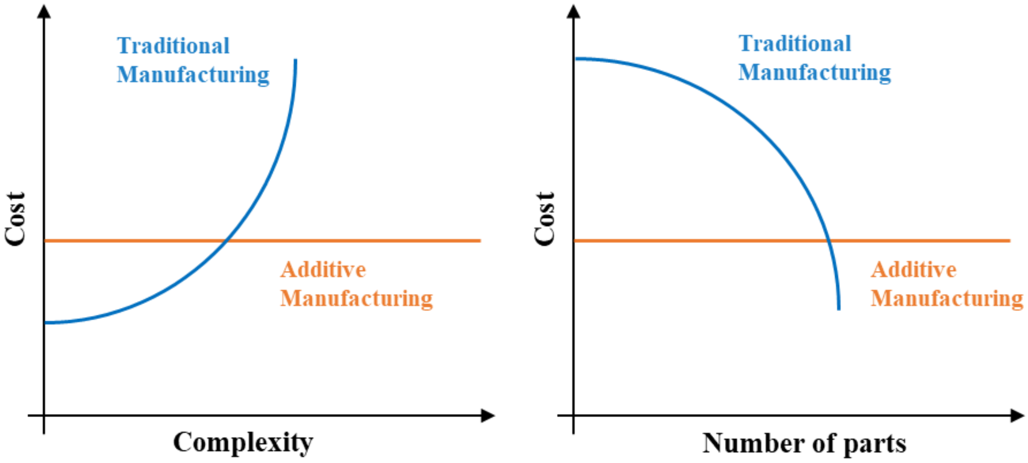

Figure 1. Additive manufacturing versus traditional manufacturing cost graph

This advancement has been made possible thanks to enabling technologies such as computer-aided design (CAD), computer-aided manufacturing (CAM), and computer numerical control (CNC). These three technologies together facilitated the development of rapid prototyping [4].From 2015, Additive Manufacturing is standardized and consists of a set of seven technologies, as defined by the ASTM/ISO 52900 [5], categorized according to the type of process, see Figure 2.

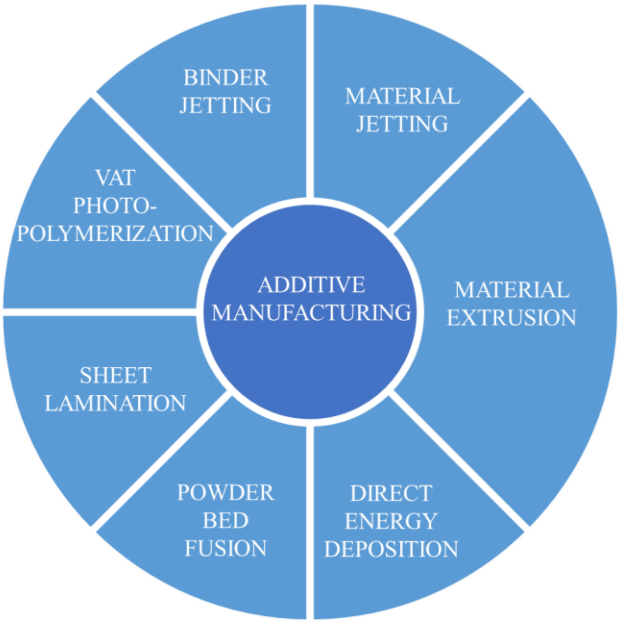

Figure 2. Additive Manufacturing Technologies as defined by ASTM/ISO 52900

Material Extrusion Additive Manufacturing

Material extrusion additive manufacturing (AM) is recognized as one of the most prevalent 3D printing methodologies, owing to its cost-effectiveness and adaptability in contrast to alternative AM methodologies [6–8]. In Material Extrusion Additive Manufacturing (MEX), material in the form of pellets, paste, or filament is pushed through a nozzle under pressure. When the pressure remains constant, the resulting extruded material, often referred to as "roads," maintains a consistent flow rate and cross-sectional diameter. This diameter remains steady as long as the nozzle's movement across the deposition surface maintains a constant speed that matches the flow rate. The material being extruded must be in a semisolid state when it exits the nozzle and must fully solidify while retaining the deposited shape. Additionally, it must bond with previously extruded material to create a solid structure.

Given the extrusion process, the additive manufacturing (AM) machine must be capable of both horizontal movement and the ability to start and stop material flow during movement. After completing one layer, the machine must either move upward or lower the part to enable the creation of the next layer.

Two primary approaches are used in the MEX processes. The most common approach involves using temperature control to manage the material's state. Molten material is liquefied within the nozzle, allowing it to flow out through the nozzle's tip, bond with adjacent material, and solidify. This approach resembles traditional polymer extrusion processes, except that the extruder is mounted vertically on a plotting system rather than remaining in a fixed horizontal position.

An alternative approach involves inducing solidification through a chemical change. In such cases, curing agents, residual solvents, reactions with air, or the drying of "wet" materials enable bonding. Parts may then cure or dry to achieve full stability. This approach can be applied to paste materials and may be particularly relevant in biochemical applications where material choices are limited due to the need for biocompatibility with living cells. However, it may also find industrial applications, possibly using processes related to reaction injection molding rather than relying solely on thermal effects.

Depending on the specific extruder employed, MEX can be categorized into three distinct types: filament-based, plunger-based, and screw-based (see Figure 3) [9].

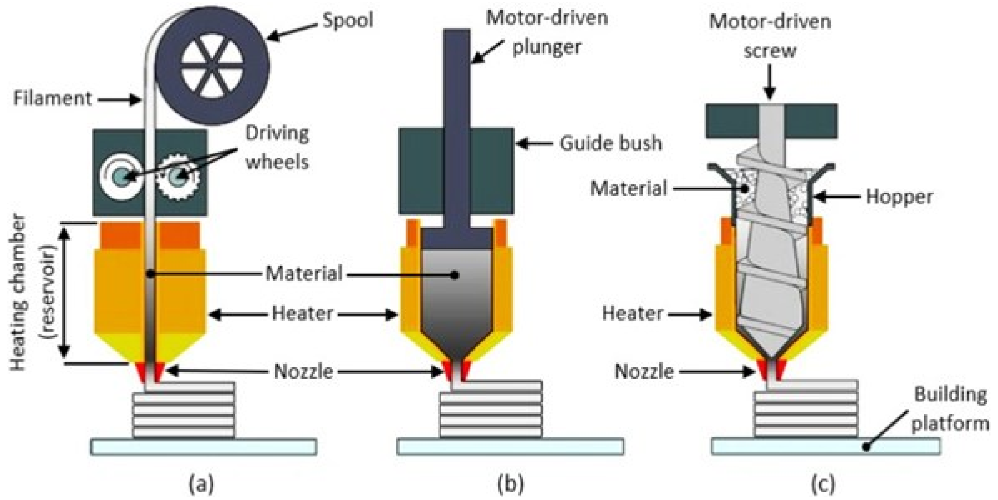

Figure 3. Different type of MEX processes: (a) filament-based: (b) plunger-based; (c) screw-based (adapted from [9])

a. Filament-based process

Filament-based extrusion has been firmly established within the 3D printing community [10]. In filament-based processes, also known as Fused Filament Fabrication (FFF) or Fused Deposition Modeling (FDM), the filament, which can have a diameter of 1.75 mm or 2.85 mm, is conveyed through an extruder comprised of two driving wheels driven by a stepper motor, allowing the filament to be extruded through the nozzle. The prevailing choice for feedstock filament materials predominantly comprises amorphous thermoplastics. FFF has emerged as the most extensively employed straightforward material extrusion procedure, accessible to both hobbyists and industrial users. This accessibility is attributed to the ready availability of filament materials, the cost-effectiveness of the process, and the absence of constraints on build size.

b. Plunger-based process

Instead of using drive wheels like in the filament-based process, a motor-driven plunger or syringe is used in the plunger-based MEX to help the flow of materials. This method works well for printing pastes and other fluid-like materials that are frequently used in additive manufacturing [11–13]. The feedstock material is pushed into the print head's heating chamber via the plunger or syringe, which also expels a fluid-like material onto the building platform or the layer that has already been printed. It's important to note that this technique does not require complete melting of the material because the high pressures used allow extrusion to occur at temperatures lower than the substance's melting point. Since the feedstock employed has a very low melting point, this approach enables the deposition of additive manufacturing materials even at lower process temperatures.

c. Screw-based process

Within screw-based systems, pellets are housed within a hopper positioned at the uppermost portion of the barrel. These pellets are introduced into the space situated between the stationary barrel and the rotating screw. The relative motion between the barrel and the screw serves to propel the material along the length of the barrel. Adequate heat is supplied to these pellets via a band heater located near the nozzle. Consequently, the pellets undergo a transformation into a viscoelastic state due to the heat application. The extrusion of material then occurs in this viscoelastic state through a nozzle. The pellet extruder offers enhanced material versatility and ensures a consistent printing process [14,15]. In [16], the transition from filament-based to screw-based extrusion became necessary to produce parts using flexible materials. These flexible materials posed challenges in the filament-based extrusion process.

Multi-step MEX processes for ceramics

A multi-step process is necessary when the feedstock material contains sinterable powder; two additional phases are introduced into the process chain, known as debinding and sintering, with the initial step being referred to as printing or shaping. The resulting product following the printing stage is referred to as the "green part," which is a combination of sinterable powder (such as metals or ceramics), a polymeric binder (comprising the main binder and backbone binder), and additives.

The binder system employed for preparing feedstock usually comprises a blend of one or more thermoplastic polymer components. Careful selection of both the binder constituents and the production method is crucial, as these factors can significantly impact the final sintered parts, even though they are entirely removed during the debinding process. The binder components can be categorized into three groups [17,18]:

- Primary Binder: This polymer, typically a thermoplastic, constitutes most of the binder system and serves as its principal element. During the debinding phase, it is the first component to be eliminated. Typically, a low-molecular-weight substance is chosen to maintain lower viscosity, thus preventing interactions with the powder and heavier components. Examples of commonly used binders include polyoxymethylene (POM), polypropylene (PP), polyethylene glycol (PEG), low-density polyethylene (LDPE), thermoplastic elastomers (TPE), stearic acid (SA), paraffin wax (PW), and polyolefin-based binders [19–21].
- Backbone (up to 50%): The second component, referred to as the backbone, remains unchanged throughout the debinding process. It contributes to the structural integrity of the brown part following debinding. Thermal degradation of the backbone occurs either before or during the sintering process.
- Additives (up to 10%): To facilitate the uniform dispersion of powder particles within the binder, various additives are employed, including dispersing agents,

compatibilizers, plasticizers, waxes, and stabilizers. These additives help prevent the segregation and agglomeration of constituents.

Following the debinding process, the component is referred to as the "brown part." Typically, at this stage, the primary binder has been eliminated. There are primarily three methods for debinding: solvent, thermal, and catalytic. Solvent debinding relies on dissolution and diffusion phenomena, and the treatment temperature and duration depend on factors like particle distribution and the shape and size of the printed components. Catalytic debinding is a process where the primary binder is effectively eliminated through direct interaction with catalytic acid vapor, causing the binder to transform into vapor and disperse due to the catalyst's action [19].

During thermal debinding, exposure to heat leads to slight shrinkage. In some instances, solvent and thermal debinding can be performed sequentially. The remaining polymer component (the backbone) is removed during the sintering process.

When weighing the advantages and disadvantages of the debinding methods, both solvent and catalytic debinding are chemical-based, but catalytic debinding poses safety hazards, whereas solvent-based debinding has a lower environmental impact. Thermal debinding consumes a significant amount of energy. Both thermal and solvent debinding can be adjusted to be more environmentally friendly, often referred to as "green methods."

Ultimately, following the initial removal of the primary binder, the brown part undergoes a sintering process. Typically carried out in a furnace, sintering involves the combustion of the remaining polymer, causing the powder particles to fuse together, resulting in a fully formed metal or ceramic component known as the "sintered part." The sintering temperature typically falls within the range of approximately 70-90% of the melting point of the sinterable powder.

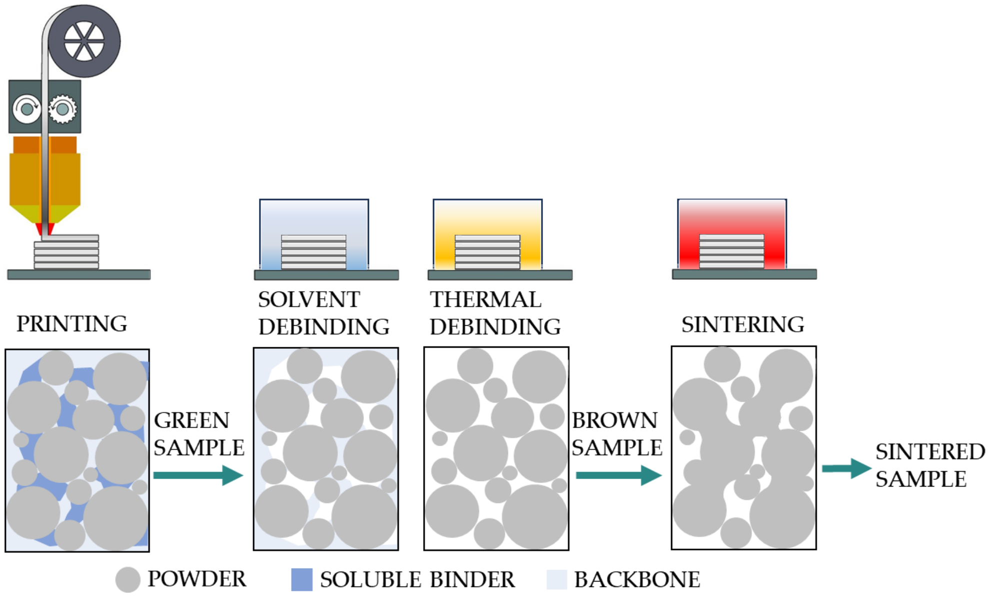

Figure 4. Printing, Debinding and Sintering process-chain (adapted from [17]**)**

One critical consideration prior to producing a metal or ceramic part using this multi-step method is accounting for the part's enlargement during the printing process. The elimination of the polymeric portion during debinding and sintering leads to a reduction in both the volume and weight of the final part due to shrinkage effects [22]. Therefore, to achieve the desired dimensions in the final product, a deliberate oversizing is necessary. This can be incorporated into the part's design or implemented during the slicing process.

Based on the patented Fused Deposition Modelling (FDM) process created by Stratasys Inc., Fused Deposition of Ceramics (FDC) was initially introduced in 1995 by Danforth [23]. FDC technique was created to manufacture ceramic components using filament made from the same or a related feedstock used in injection molding. Ceramics as a class of materials are challenging to shape because they cannot bend plastically. Complex shapes for ceramics have not been easily attainable using conventional shaping techniques. However, the development of AM has completely changed this industry by making it possible to produce complex ceramic components with greater accuracy [24,25].

With little literature on the subject, multi-material part production by material extrusion is still in its early phases. Specific requirements, including similarity in shrinkage behavior, sintering conditions, and coefficient of thermal expansion (CTE), must be met to produce successful multi-material components. A component with several properties, including electrical, thermal, optical, magnetic, and mechanical, may be created by combining metals and ceramics [26].

Scope of the research

Within the examined "Global Context," this research work is positioned with the purpose of proposing experimental methodologies for characterizing filament-based Material Extrusion Additive Manufacturing (MEX) processes based on adequate literature analysis.

The major goal is to improve the mechanical properties thorough a full characterization of process parameters, materials rheology and thermal characteristics of the feedstock. These materials are widely used in industrial, aerospace, automotive and aviation applications. This approach is used to numerous sorts of materials in this work, investigating the complete range of possibilities. It starts with commodity polymers, then moves onto techno-polymers, composites, and finally ceramics. This diversification in material discovery enables a thorough examination of the possible benefits that this technology can provide in a variety of industrial and aerospace situations.

Chapter 1

STATE OF THE ART

In this chapter, an analysis will be conducted of the current state of the art in filament-based MEX, divided by material type, ranging from polymers to composites and ultimately ceramics. The study of the state of the art has been deemed essential for the experiments subsequently carried out in the thermophysical domain to optimize the printing parameters of the parts manufactured through MEX.

1.1 Polymers and techno-polymers

Polylactic Acid

Research in the field of MEX AM has focused on the feasibility and processability of commodity polymers such as Polylactic Acid (PLA), Acrylonitrile Butadiene Styrene (ABS), Polyethylene Terephthalate Glycol (PETG), and subsequently transitioned to techno-polymers like Polyamide 6 (PA6), Polypropylene (PP), Polyether Ether Ketone (PEEK), and Polyetherimide (PEI), which find applications in sectors such as automotive, aerospace, and naval industries. The primary investigations in this sector have centered on the influence of process parameters on the mechanical properties of the aforementioned polymers and engineering polymers [27–31]. Additionally, researchers have explored the significance of creating lightweight structures, one key aspect of AM. Numerous studies have delved into how these lightweight structures respond to various stresses, leveraging the flexibility of employing diverse infill patterns [32–35]. It is crucial to highlight that the properties can vary significantly compared to counterparts processed through traditional manufacturing due to the inherent anisotropy in MEX technology [36–41]. The convergence of adjacent polymer lines, referred to as "roads," significantly influences the microstructure and functional characteristics of the final component [31,42,43]. This merging procedure relies on a range of process variables and material attributes. Each parameter that can have an impact on the printing process was thoroughly investigated and assessed in terms of its impact on the quality attributes of the finished component by Bähr et al [44]. According to what is known currently, important elements affecting component quality include material composition, slicing and depositing tactics, and most significantly, the cooling procedure. The quality of the component is significantly impacted by the road's cooling process as it goes from extrusion temperature to ambient environmental temperature. The cooling process was divided into five distinct phases, each of which was distinguished by certain temperature thresholds deriving from the configuration of the process and the qualities of the materials. According to the research, the mechanical properties of the components are mostly influenced by the sintering phenomena and crystallization at the printed roadways' interface. The semi-solid material's rheological behavior and consequent shrinkage can affect geometric features like dimensional accuracy, form, and positioning. Shrinkage features of printed components are controlled by the glass transition temperature, and warping is attributed to growing residual stress.

Bardiya et al. [45] investigated the influence of three key input parameters on the impact properties of FFF printed PLA components. The build orientation, infill density, and layer thickness are some of the chosen input factors. Research findings indicate that an increased layer thickness is associated with higher average impact strength in the samples. Specimens exhibiting a greater degree of building orientation display superior impact strength compared to those with a 0° building orientation. Furthermore, compared to parts made with lower infill densities, parts with higher infill densities demonstrate stronger impact strength. In conclusion, a mid-level layer thickness (0.2 mm), a mid-level orientation (30°), and a maximum infill density (80%) can be used to produce PLA components with the best impact strength.

Techno-polymers

When discussing techno-polymers, one typically refers to polymers that must exhibit a range of specific properties. These include robust mechanical strength, which enables them to withstand demanding mechanical loads and challenging environmental conditions. Additionally, they are expected to demonstrate exceptional resistance to chemical degradation when exposed to various chemicals and solvents. Moreover, these polymers possess a remarkable ability to maintain their structural integrity at elevated temperatures, ensuring good thermal stability. They are valued for their electrical insulating properties, making them well-suited for applications within the electronics and electrical industries. Furthermore, their low friction characteristics make them effective in applications requiring reduced friction, such as bearing materials. These polymers also excel in dimensional stability, retaining their shape and size across diverse environmental conditions. Additionally, they exhibit flame resistance, which prevents rapid ignition and flame propagation, rendering them suitable for fire safety applications. Furthermore, techno-polymers can endure prolonged exposure to ultraviolet radiation without significant degradation. Finally, some applications, such as optical lenses and display screens, demand transparency or optical clarity, a key attribute that these polymers can provide.

PEEK, which is a linear, aromatic, semicrystalline thermoplastic, serves as a notable example of a techno-polymer [46]. When referring to PEEK, specific properties that are often emphasized include:

1. High Temperature Resistance: PEEK exhibits exceptional thermal stability, allowing it to maintain its mechanical and chemical properties at elevated temperatures, even surpassing 250°C (482°F).

2. Chemical Resistance: PEEK is highly resistant to a wide range of chemicals, including acids, bases, and organic solvents, making it suitable for applications in aggressive chemical environments.

3. Mechanical Strength: It possesses excellent mechanical strength and stiffness, making it suitable for structural components in industries such as aerospace and automotive.

4. Wear and Friction Resistance: PEEK's low friction coefficient and wear resistance make it an excellent choice for bearing and sliding applications.

5. Electrical Insulation: It is an excellent electrical insulator, which is valuable in electrical and electronic applications.

6. Biocompatibility: PEEK is biocompatible and widely used in medical implants and devices.

7. Radiolucency: It has the property of being radiolucent, which means it doesn't interfere with X-ray or other imaging techniques, making it suitable for medical implants.

8. Dimensional Stability: PEEK maintains its dimensional stability, even in challenging environments, making it suitable for precision components.

9. Flame Resistance: It has good flame resistance and low smoke emission properties.

These characteristics make PEEK a versatile material with a wide range of applications, including aerospace components, medical implants, automotive parts, and industrial components where high performance under demanding conditions is required [47–51].

While FFF technology is becoming more widely recognized for its user-friendly attributes, achieving satisfactory printing outcomes with PEEK demands substantial dedication owing to the distinctive characteristics of the material and the printing process. Numerous factors exert an influence on the outcomes, with primary emphasis on the printing temperature, layer height, and printing speed [52–57].

In 2018, Rinaldi et al. [58] presented a comprehensive investigation into FFF printing of PEEK, commencing with the preparation of the filament from Victrex 450 PF [59]. Initially, a comparison between the thermal and microstructural properties of PEEK filaments and printed parts was conducted, revealing negligible differences in terms of Tg, Tm, and crystallinity. Cold crystallization phenomena were observed in the printed samples, likely stemming from the rapid melting and subsequent cooling during nozzle deposition.

Notably, significant variations in mechanical performance were observed in the printed samples, contingent upon the printing direction (see Table 1). Samples printed with 100% infill in the XY plane exhibited mechanical properties akin to those of extruded or injection-molded samples, whereas those printed in the Z direction (also with 100% infill) displayed extreme brittleness and premature failures. These results were expounded upon by considering fracture mechanisms and the presence of internal porosity resulting from the printing process. The former was attributed to the orientation of the deposited material in relation to the direction of tensile stress, with Z-printed samples demonstrating brittle fracture due to bonding failure between layers.

Table 1. Main mechanical properties of printed PEEK sample compared with literature and data (adapted from [58]).

Sample	Build orientation	E [GPa]	σ [MPa]	Ref.
PEEK-XY-100	flat	3.98 ± 0.78	98.9 ± 2.3	[58]
PEEK-Z-100	vertical	1.6 ± 0.99	19.6 ± 6.1	[58]
PEEK data sheet	-	4.0	98	[59]
Injection moulded PEEK	-	4.0	100	[60–62]

Furthermore, it is noteworthy to mention that the influence of infill density was found to be substantial, with a tensile strength value of 60.6 ± 4.8 MPa. This represents a reduction of approximately 40% when compared to the tensile strength in the case of a 50% reduction in infill density. It was demonstrated that the diminished mechanical properties in samples with less than 100% infill could be attributed to a reduction in the effective resistant cross-section. This reduction, as observed through CT scan analysis, resulted from both the reduced material deposition and the deposition pattern, which is associated with the printer. Consequently, it is evident that the slicing and printing pattern play a pivotal role, particularly when working with lower infill densities, prompting a discussion on the significance and appropriate methodology for mechanical characterization in FFF-printed specimens. It is important to underscore the significance of leveraging these findings to engineer lightweight components while maintaining their structural integrity.

The impacts of printing temperature, infill rate, layer thickness, and printing speed, on tensile properties were investigated by Deng et al. [63]. Through comprehensive analysis, the most favorable combination of printing parameters emerged as follows: a printing speed of 60 mm/s, a layer thickness of 0.2 mm, a temperature of 370 °C, and an infill ratio of 40%. The optimal combination of printing parameters led to the following mechanical properties: a tensile strength of 40.0 MPa and an elongation of 14.3%. Examination of SEM images exhibited excellent fusion effects, as well as filament-to-filament and interlayer bonding, at these specified parameters. Additionally, bending and impact tests were conducted on printed specimens with optimized parameters, resulting in satisfactory flexural strength of 68.2 MPa and impact strength of 101.2 KJ/m^2.

Geng et al. [53] emphasized the pivotal role of extrusion speed and printing speed in 3D printing PEEK. Their research explored how these parameters affect the microstructure and dimensions of extruded PEEK filaments. They conducted a comprehensive extrusion process analysis, measuring extrusion force and resistance. This analysis illuminated the intricacies of maintaining a continuous extrusion process while highlighting potential challenges like surface defects and melt die swelling. To address discrepancies in filament dimensions compared to ideal models, they devised an optimized control algorithm linking extrusion speed and filament diameter. This approach enhances FDM part quality, ensuring higher accuracy and desired PEEK sample properties with precise parameter application.

In 2020, Zanjanijam et al. [64] investigated the FFF 3D-printing of PEEK, with a specific focus on its potential application in producing 3D printed PEEK components intended for use on the International Space Station. The primary objective of their study was to gain a deeper understanding of the intricate relationships among the printing process, material structure, and resulting properties of this high-performance plastic. The research deals with the impact of various printing parameters, including building orientation, nozzle temperature, ambient temperature, bed temperature, layer thickness, print speed, and heat treatment, on both the physical and mechanical properties, as well as the overall print quality. To provide practical guidance, the review extracted recommended parameter settings from existing research, with a particular emphasis on tensile mechanical performance, as presented in Table 7.

Table 2. Recommended values of the printing parameters of PEEK (adapted from [64])

Parameter	Value/Type	Ref.
Raster angle	0°	[65]
Layer thickness	0.1-0.3 mm	[66]
Printing temperature	420-440 °C	[55]
Chamber temperature	150-200 °C	[67]
Printing speed	20 mm/s	[68]
Infill	100%	-
Heat treatment methods	Annealing	[67]

It is crucial to note that these recommendations primarily pertain to tensile properties. While the review of the literature revealed promising mechanical results for PEEK samples printed through the FFF process, several challenges persist within the domain of 3D printing with PEEK, warranting careful consideration.

From a technical standpoint, optimizing the temperature differential between the nozzle and the bed/chamber in 3D printers emerged as a critical factor. Minimizing thermal gradients across printed layers has resulted to be necessary to produce parts endowed with desirable mechanical properties and dimensional stability.

Following these studies, El Magri et al. [69–72] conducted various studies on the printability of PEEK specimens through FFF technology. Their research determined that printing temperature wielded the most profound influence over the tensile properties and crystallinity degree of 3D printed PEEK. In addition to the parameters investigated by Rinaldi et al. [58] and Deng et al. [63], these factors assume crucial significance as they directly impact interlayer adhesion.

PEEK has been the subject of extensive research, including Differential Scanning Calorimetry (DSC) studies and other approaches targeted at creating a thermal profile for the material. Jin et al. [73] identified the dual melting peaks in DSC analysis as arising from the reorganization of PEEK crystals due to the material's rapid recrystallization rate compared to the imposed heating and cooling rates. According to Liaw et al. [74], the analysis of crystallinity levels underscored the importance of achieving high values to enhance interlayer bonding adhesion, resulting in superior mechanical properties. Increased crystallinity was achieved by raising nozzle temperature and layer height while decreasing wait time before part removal and print speed.

In 2022, Lee et al. [75] explored how the temperature history during 3D printing of PEEK parts influences crystallinity and morphology. To control convection during printing, a variable-speed nozzle fan was used. Combining experimental and numerical approaches, the study analyzed convection's impact on cooling rate, Degree of Crystallinity (DOC), and crystal morphology. Fast melt cooling rates were achieved regardless of convection due to PEEK's high melting point. This resulted in a minimal DOC (around 10%) with extremely small crystal structures not visible under light microscopy. With a 0% fan speed, a secondary heat cycle led to cold crystallization, raising DOC to approximately 20%, making crystal morphology visible under light microscopy. However, even at 20% DOC, the crystalline structure remained distinct from slower-cooled materials. At 100% fan speed, the material bypassed this secondary heat step, maintaining a low DOC.

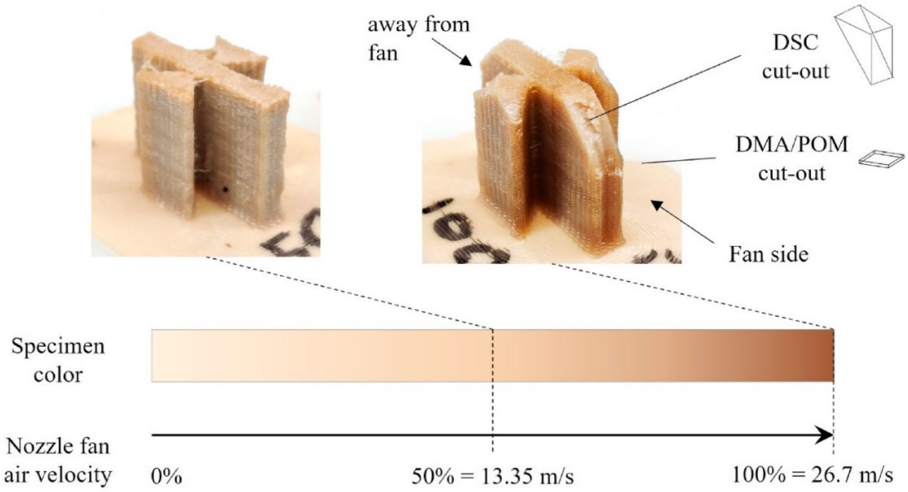

Figure 5. Color band as a function of fan speed percentage on PEEK samples (adapted from [75]).

Given that PEEK is a semi-crystalline polymer, it is critical to investigate the possibility of increasing the crystallinity of 3D printed PEEK components using post-printing heat treatment. Yang et al. [67] investigated the influence of different heat treatment procedures on PEEK crystallinity, which had localized effects on mechanical characteristics. The findings reveal a direct correlation between ambient temperature and crystallinity, with crystallinity levels increasing from 17% to 31% as the ambient temperature rises from 25°C to 200°C. Air cooling, furnace cooling, quenching, annealing, and tempering were among the heat treatment procedures used. Furnace cooling and annealing methods proved to be superior and more efficient approaches, resulting in higher degrees of crystallinity (36% and 38%) and improved mechanical performance compared to tempering or quenching methods, as shown in Figure 6.

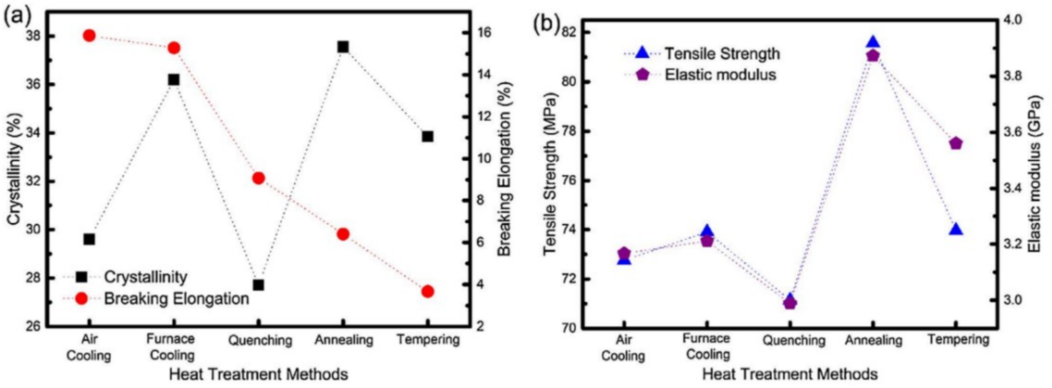

Figure 6. Results of different heat treatment methods on the (a) crystallinity and (b) mechanical properties of different PEEK samples (adapted from [67]).

Basgul et al. [76] investigated how the pore structure of PEEK pieces altered after annealing without a reduction in unwanted porosity caused by interlayer debonding.

Jiang et al. [77] found that annealing had a favorable effect on mechanical, tribological, and viscoelastic properties and causes slower creep and stress relaxation.

As gleaned from the conducted studies, the optimization of printing parameters is intricately linked to the enhancement of crystallinity and interlayer bonding. These factors have a direct influence on the mechanical properties of the printed components [74,78–81].

In 2023, Rendas et al. [82] examined the impact of 3D printing parameters on the tensile and flexural properties of PEEK samples, manufactured on an Apium 3d printer with Apium PEEK 450 Natural [83]. The optimal values for PEEK's tensile strength were found to be 485°C for Nozzle Temperature (NT), 130°C for Zone Heater Temperature (ZHT), 0.2 mm for Layer Height (LH), and 1 for Extruder Multiplier (EM), with a minimum layer height of 0.1 mm recommended for tensile modulus. For flexural modulus and strength, the ideal parameters were 495°C for NT, 150°C for ZHT, 0.3 mm for LH, and 1.1 for EM. These findings were validated through tensile and flexural tests on samples printed with these optimal parameters. Various infill configurations were explored to reduce void volume in the samples by up to 65%, leading to improvements in both tensile and flexural properties. The alternating infill line angle configuration (+45°/-45°) resulted in the highest tensile strength (89.8 MPa) and modulus (3.82 GPa). Annealing treatments were applied to enhance the mechanical properties of the samples, resulting in a maximum increase of 29.9% in tensile modulus and 16.6% in flexural strength. These findings emphasize the importance of focusing on interfacial adhesion between printed lines and layers for enhanced strength and stiffness in PEEK 3D prints.

So far, the emphasis has predominantly been on mechanical properties, but it is important to also analyze thermal properties and how they interact with anisotropy and bonding between layers to develop comprehensive prototypes capable of replacing traditional manufacturing counterparts [84,85].

Thermal properties

The heat conductivity of the MEX part differs from that of the original material, and it is expected to fluctuate depending on the raster and construction directions. This necessitates a detailed measurement of the thermal properties of the completed item. Printing process errors may cause variations in thermal properties. Low thermal conductivity can be caused by insufficient heat flow, incorrect adhesion, and poorly planned process parameters.

Chung et al. [86] have conducted measurements to investigate the impact of random voids on thermal properties using a Hot Disk device and finite-element simulation. The obtained results show that the material's material properties are greatly influenced by the existence of anisotropic voids aligned in particular orientations inside the material. Notably, it was found that appropriately placed anisotropic ellipsoidal gaps significantly reduce thermal conductivity along their principal axes. In addition, while keeping the same void ratio, bigger void clusters positioned perpendicular to the direction of heat flow can significantly improve the insulating effectiveness of the material. Furthermore, it was demonstrated that the existence and orientation of these anisotropic voids had a significant impact on the directional modulus of insulating medium. These results highlight the major impact of anisotropic voids on the mechanical and thermal characteristics of insulating medium. As a result, properly planned anisotropic voids can significantly enhance the material's thermal and mechanical performance.

A one-dimensional heat flux approach was employed by Ravoori et al. [87] to measure the thermal conductivity in the build direction as they investigated the influence of process factors on the thermal characteristics of AM parts. Their examination of the relationship between thermal conductivity, raster speed, and layer thickness was significantly influenced by these factors, which was further confirmed by high-speed photography of the printing process carried out at various levels of these factors. According to Prajapati et al. [88], the anisotropy in AM components and its influence on thermal properties are difficult to deal with. According to their research, the significant interfacial thermal contact resistance in the build direction is the main cause of this anisotropy. They offer insightful information on how this metric is influenced. The thermal conductivity in the Z-direction is much lower than in the X-direction, according to the data, indicating significant anisotropy in heat conduction. The air gap between roadways during deposition affects this anisotropy (see Figure 8 and Figure 9).

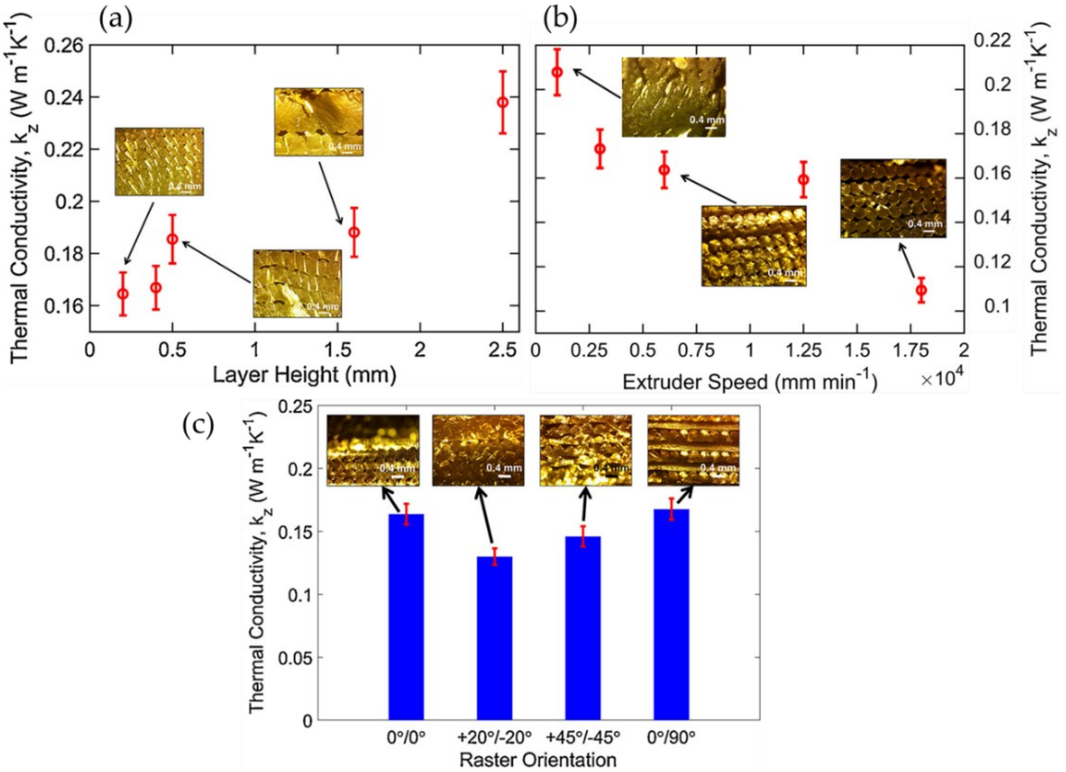

Figure 7. Plot showing the variation of build direction thermal conductivity with (a) layer height; (b) estruder speed; (c) raster orientation for the same overall sample size (adapted from [87]).

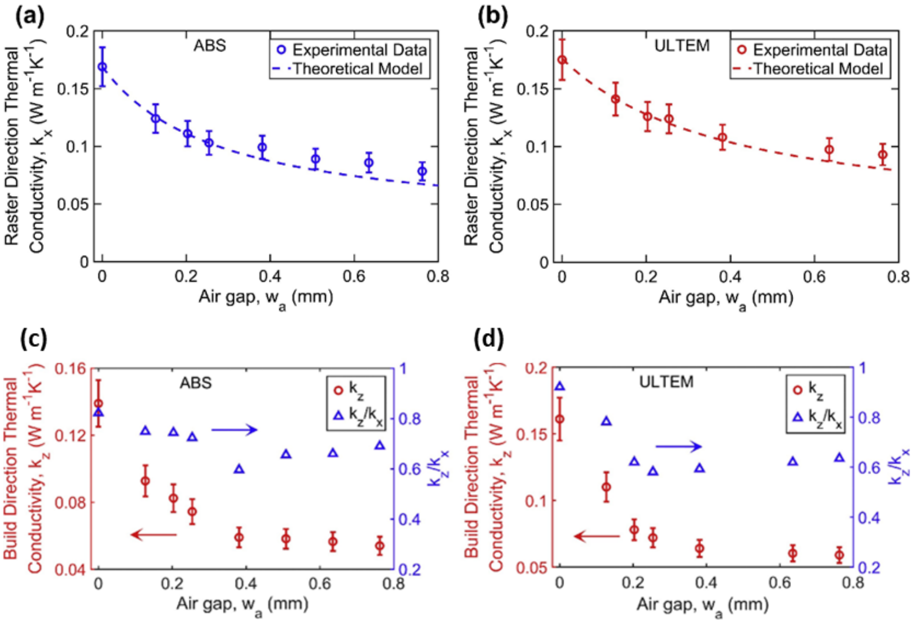

Figure 8. Measured thermal conductivity in the raster direction, k_x, as a function of air gap for (a) ABS; and (b) ULTEM filament materials. Measured thermal conductivity in the build direction, k_z, as a function of air gap for (c) ABS; and (d) ULTEM filament materials. The ratio k_z/k_x, which represents the degree of anisotropy is also plotted in each case (adapted from [88]).

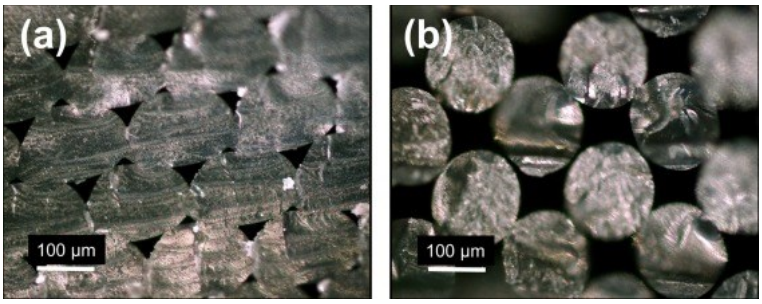

Figure 9. Cross section images of two ABS samples with (a) zero; and (b) 0.25 mm air gap, showing significant difference in microstructure. In each case, the raster direction, x, is normal to the plane of the image (adapted from [88]).

This paper provides important information on the dependence of this critical parameter on process conditions and demonstrates that strong interfacial thermal contact resistance in the build direction is the fundamental cause of such anisotropy.

The crystallinity and molecular orientation of semi-crystalline polymers significantly influence the thermal conductivity (TC) of polymeric materials. As highlighted by Bai et al. [89] crystalline materials have a higher TC than amorphous materials due to the regularity of lattice arrangement, which affects the mean free path (kph). The random conformation of chains causes scattering of phonons, leading to an infinite mean free path in an ideal crystal lattice. Molecular orientation increases parallel to the direction of orientation (k∥) with increasing uniaxial stress or stretching orientation, while perpendicular to the direction of orientation (k⊥) decreases slightly. Semi-crystalline polymers, such as PE, PP, PET, and POM, can achieve a significant increase in TC up to 1 W/ m × K. For amorphous polymers like PMMA, PET, PEMA, PVC and PC, the increase is smaller, approximately 0.10–0.22 W/ m × K at temperatures higher than 100 K. At lower temperatures, the TC values are even smaller due to the relatively low achievable draw ratio [90].

In filament fabrication, molecular orientation occurs during extrusion when the molten polymer is stretched due to natural stress applied to the macromolecules. If the filament cools rapidly, this orientation is largely maintained, but once the filament is reheated to a temperature that allows the molecular chains to return to their relaxed state, the orientation is not maintained, potentially affecting the properties of the final 3D printed part.

The orientation of macromolecules can be achieved via FFF 3D printing, but there is limited research on this topic. During the manufacture of 3D printed plastic parts, polymer chains are often not oriented due to the narrow temperature range in which orientation can be carried out effectively. Shear effects in an FFF 3D printer can induce a certain molecular orientation that depends entirely on the available time and temperature. At temperatures below the melting or flowing temperature, the force required for mechanical deformation is too high, and at temperatures close to the melting or flowing temperature, the polymer macromolecules can quickly relax to a random state, making it difficult to achieve molecular orientation via 3D printing.

Several studies have focused on molecular orientation in FDM 3D printing. Ghodbane et al. [91] aimed to increase the mechanical properties of Poly(Desaminotyrosyl-Tyrosine Dodecyl Dodecanedioate) by moving the print head at sufficiently high speeds. By optimally combining printing condition parameters such as the print speed, nozzle diameter, filament extrusion pressure, and temperature, it is possible to keep the polymer in a semi-solid state at the nozzle tip, allowing the polymer to be stretched before cooling to a solid.

Verbeeten et al. [92] found that the highest degree of orientation for ABS was achieved at the highest speed. They also evaluated the dimensional changes after a thermal treatment and found that the orientation of the printed part is slightly less noticeable than the orientation of the filament itself. In all cases, a contraction of test specimens occurred: for the filament itself by 30.5% in length, 20.6% in width, and 20.6% in height. At a speed of 35 mm/s, the contraction of the printed samples was 19.9% in length, 3.6% in width, and 26.7% in height.

Higher orientation with higher print speed (9.6 mm/s and 35 mm/s, respectively) was also reported by Verbeeten et al. [93] when PLA was evaluated. However, the used printing speeds used could still be marked as still relatively slow. The authors concluded that the printing speed is not the only important parameter for the molecular orientation and elongation of the polymer chain. High temperature of the substrate is crucial for the printing of engineering or hi-tech polymers with high heat resistance and may be preferred for applications where TC is required.

Ghodbane et al. [91] confirmed that printing speed is not the only important parameter in determining molecular orientation in Poly(Desaminotyrosyl-Tyrosine Dodecyl Dodecanedioate) printing. They found that the final molecular orientation of PLLA (Poly-l-Lactide) was significantly lower at a speed of 4 mm /s and that the resulting molecular orientation depends more on the combination of all parameters, not solely on the printing speed. The crucial criterion for the orientation of the polymer is the flow-induced orientation and the ability to maintain the orientation during polymer cooling. The authors attribute worse results in PLLA to a sharper melting transition compared to Poly(Desaminotyrosyl-Tyrosine Dodecyl Dodecanedioate).

Liu et al. [94] found that the TC of samples with 20 wt% h-BN increased slightly when the printing speed was increased in several intervals from 10 to 200 mm/s (see Figure 10). More studies on crystallinity and molecular orientation are needed, as the influence of printing parameters/conditions on TC for various polymers is still unknown.

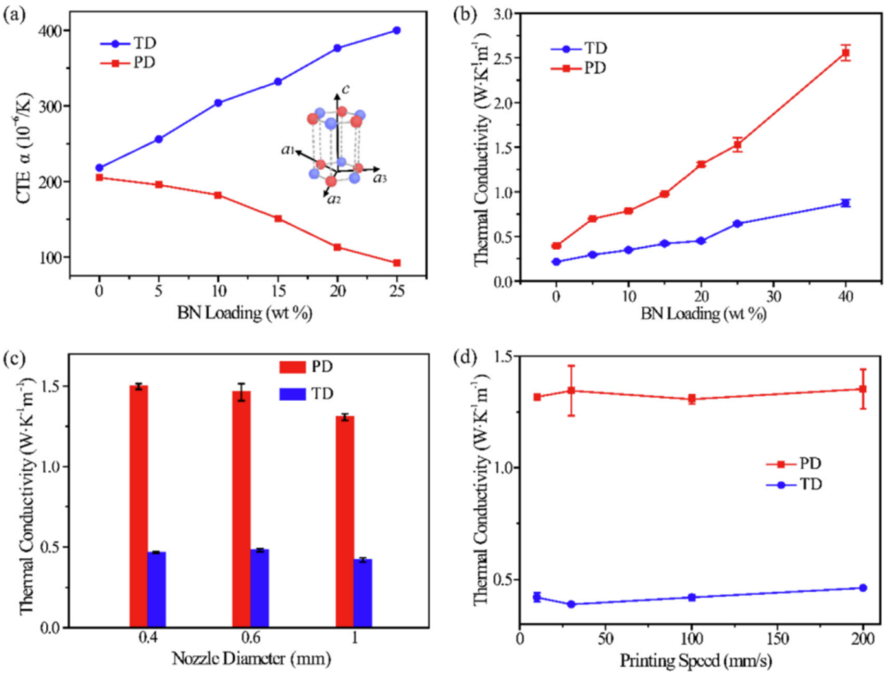

Figure 10. (a) Coefficient of thermal expansion (CTE) of the hBN/TPU composites with different hBN loading. The inset image is a diagram of hexagonal cell and its a and c axis. (b) Thermal conductivity of the hBN/TPU composites with different hBN loading. The thermal conductivity of composites printed using (c) different nozzle diameter and (d) printing speed. The BN loading of samples is 20 wt% (adapted from [94])

1.2 Composites

A composite material is typically defined as a material composed of two or more distinct substances, such as fibers or particles, combined to create a new material with enhanced properties, often surpassing those of the individual components.

Composite materials containing a substantial proportion of fillers have recently gained significant attention in the realm of Material Extrusion (MEX) Additive Manufacturing (AM). This recent interest can be attributed to filament-based technologies that enable the continuous deposition of fibers. These technologies draw inspiration from Fused Filament Fabrication (FFF) in that they feature a nozzle-based material deposition mechanism. However, they distinguish themselves by permitting the construction of components using composite materials [95–97]. Printers equipped with Continuous Filament Fabrication (CFF) technology are equipped with two nozzles for the printing process: one is dedicated to forming the polymeric matrix, while the other is responsible for depositing the reinforcement material [98–100]. These composite materials find application across various industries, including automotive, mechanical engineering, biomedical, and aviation. Carbon Fiber Reinforced Polymers (CFRP) are of particular interest, especially for replacing metal components.

One noteworthy example is Onyx®, a material produced by Markforged Inc., which consists of a Nylon PA6 [101] matrix reinforced with chopped carbon fibers [102]. The incorporation of carbon fibers imparts superior mechanical properties to this material compared to its purely polymer-based counterparts. Numerous researchers have conducted tests on structures made from Onyx with continuous carbon fiber reinforcement, yielding favorable results, particularly in terms of tensile properties. The utilization of continuous fiber reinforcement further enhances the mechanical characteristics by creating a material composed of both a composite matrix and continuous fiber reinforcement [103,104]. The ability to manufacture lightweight composite components is highly desirable, offering numerous advantages to exploit. Given that lightweight structures have always been a focal point of study in MEX technology [105–109], the opportunity to fabricate them using composite materials is a highly attractive prospect for many researchers.

Dorčiak et al. [110] conducted a comprehensive investigation into the impact of inner structure size and shape on the mechanical properties of 3D-printed specimens, employing both numerical and experimental methods. Their study underscores the significance of closely observing and analyzing the outcomes or solutions. It becomes evident that as the size of a structure enlarges, there is a concurrent reduction in the volume of material, resulting in a natural decrease in mechanical properties. These findings play a pivotal role in ascertaining the optimal configuration and density for the internal structure. Their research identifies a square-shaped infill type (rectangular infill) as the most effective in this context.

Similar conclusions have been corroborated by the research of Bárnik et al. [111]. In their study, Bárnik et al. analyzed various inner structure configurations (see Figure 11), including hexagonal, triangular, and rectangular structures, utilizing tensile tests. Their findings indicated that the rectangular infill type exhibited an increase in ultimate load force per unit volume when compared to other infill types. Furthermore, they observed that specimens with higher infill densities consistently yielded higher ultimate tensile loads.

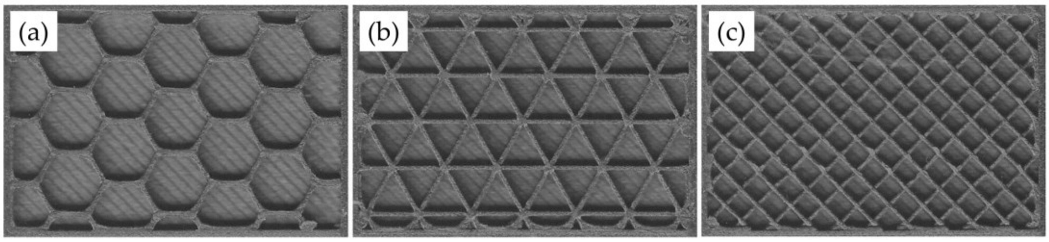

Figure 11. Different infill patterns at 20%: (a) hexagonal; (b) triangular; (c) rectangular.

In the work from Ahmadifar et al. [112], polymer-based composites were fabricated using a Markforged Mark Two 3D printer and subjected to both tensile and three-point bending fatigue loadings. Ahmadifar's study observed the homogeneous distribution of carbon fiber within the Onyx filament through microscopy. Remarkably, when printed in a solid infill pattern, samples displayed excellent stiffness and mechanical properties when subjected to tension. The findings indicated that the solid infill pattern exhibited the highest tensile strength, while the triangular infill pattern had the lowest. Notably, transitioning from the triangular to the solid infill pattern resulted in a substantial increase in tensile strength. Changing the infill pattern from triangular to either rectangular or hexagonal showed a slight improvement in tensile strength.

Regarding fatigue, the study analyzed the impact of reinforcement. The results revealed that the presence of reinforcement led to increased induced temperature and, consequently, a reduced fatigue life for not reinforced samples. This phenomenon, referred to as self-heating, offers insights into the viscous behavior of the polymer, especially in the vicinity of the glass transition zone (around 60°C). Therefore, an in-depth examination of the viscoelastic behavior of Onyx becomes imperative.

Pipalla et al. [113] conducted a comprehensive study on the hexagonal infill pattern, thoroughly characterizing it both mechanically and thermally. The primary focus of their investigation was to explore the potential for achieving lightweight structures by varying the infill percentage. Observations revealed that the number of hexagon cells decreased as the thickness and length of the hexagon cell increased. Void space and weight also had significant effects on the properties of the printed product. Upon analyzing the results, it became evident that the optimal hexagonal cell side length to thickness ratio for achieving ultimate tensile strength was 3:1. This could be attributed to the fact that if the cell thickness deviated from one-third of the side length, the specimen tended to break easily. Therefore, to attain superior properties, the cell thickness ideally should have been one-third of the side length.

For achieving the best High Deflection Temperature (HDT) properties, a hexagonal cell length to thickness ratio of 3.5:1 was recommended. This ratio contained a higher volume of material, enhancing resistance to maximum temperature, and exhibited a reduced deflection rate.

To maintain appropriate void space and achieve good compression properties, a hexagonal cell length to thickness ratio of 4:1 was preferable. This ratio ensured even load distribution on the cells. Specimens with a 3:1 ratio, on the other hand, compressed at lower values due to their higher void space.

In the context of the three-point bending test, the ideal ratio for showcasing good flexural properties was 3:1. Specimens with this ratio demonstrated strong flexural strength, which increased with the enlargement of cell dimensions, leading to higher load-bearing capacity.

Specimens reached their maximum load-bearing capacity at a ratio of 3.6:1.2 due to the substantial wall thickness on the load-bearing side. Therefore, to achieve maximum impact strength and lower overall weight, it was advisable for the hexagonal cell side length to be three times greater than the wall thickness.

Hexagonal structures could effectively replace solid parts without compromising their strength, offering advantages across a wide range of industrial applications. These structures were particularly suitable for pillars due to their impressive impact and compression strength.

Furthermore, observations had revealed the formation of holes on the top layer of specimens due to the absence of support in the hollow part of the honeycomb structure. The material had projected upward, forming a convex shape, because of pressure within the hollow part of the honeycomb. To address this issue, increasing the thickness of the top layer had been an option, although this might have affected the results.

Wang et al. [35]investigated the impact of unit pattern, infill density, and strain rate on the mechanical characteristics of 3D-printed structures. By observing morphological alterations and heat maps at various tensile strain rates, they investigated deformation and failure modes. The results showed that composites with hexagonal units displayed higher tensile modulus and strength but poorer elongation at break when compared to composites with triangular units at the same infill density. Deformation and failure modes, mostly because of printing path faults, were significantly influenced by the choice of infill pattern. For triangular-unit architectures, failure started at internal nodes and expanded to others, probably because of manufacturing flaws brought on by overlapping printing routes. The collapse of composites made of hexagonal units, on the other hand, began at the circumferential wall. This was because the cellular junctions of the hexagonal units with overlapped printing routes were less defective and the circumferential wall was under more strain. According to the results of the experiment, increased infill densities resulted in better tensile and Young's strengths, indicating improved deformation resistance in composite structures. The study also found that strain rates had a substantial impact on the tensile stiffness of composite materials, with greater rates leading to higher Young's modulus and ultimate tensile stress, primarily as a result of filament stiffening. However, deformation and failure modes, when flaws remained the deciding factor, were only moderately affected by the strain rate. Finally, it was discovered that relative energy absorption capabilities in composites were minimally affected by infill pattern and density, but increased as strain rates increased across all materials.

Ali et al. [114] investigated the tensile mechanical properties of 3D-printed carbon fiber-reinforced nylon composites. They considered several influencing factors, including infill density, fill patterns, build direction, composite type, and heat treatment. The combination of a 50% infill density and a triangular fill pattern resulted in the highest tensile strength at 153 MPa, a Young's modulus of 7188 MPa, and a toughness of 5.37 MJ/m^3, surpassing the performance of rectangular and hexagonal fill patterns. This superiority was attributed to the improved performance of the triangular lattice structure, resulting in lower void content in the struts and stronger bonds. Additionally, the increase in infill density contributed to higher tensile strength, Young's modulus, and toughness, as more matrix material enhanced adhesion. Comparing build directions, the side build direction in both pure and reinforced composites exhibited higher tensile strength and Young's modulus but lower toughness compared to the flat build direction. This was due to the availability of more thermoplastic layers for side build printing, resulting in increased material and time consumption during printing, ultimately enhancing the tensile mechanical properties.

Regarding heat treatment, pure and reinforced composites in the side build direction displayed the highest tensile strength and Young's modulus, albeit with lower toughness compared to flat build direction composites. The strength of side build composites increased by 8% for pure and reinforced composites after heat treatment, while flat build composites increased by 23.40% for pure and 4.72% for reinforced composites. This improvement was attributed to the complete absorption of the matrix material by the reinforcing material, reducing porosity, and strengthening interfaces, resulting in enhanced tensile mechanical properties.

In summary, the study emphasizes the substantial impact of infill density, infill pattern, build direction, composite type, and heat treatment on the tensile mechanical properties of 3D-printed composites. These improved mechanical properties have the potential for applications in complex structures and high-performance objects, particularly in the aerospace industry.

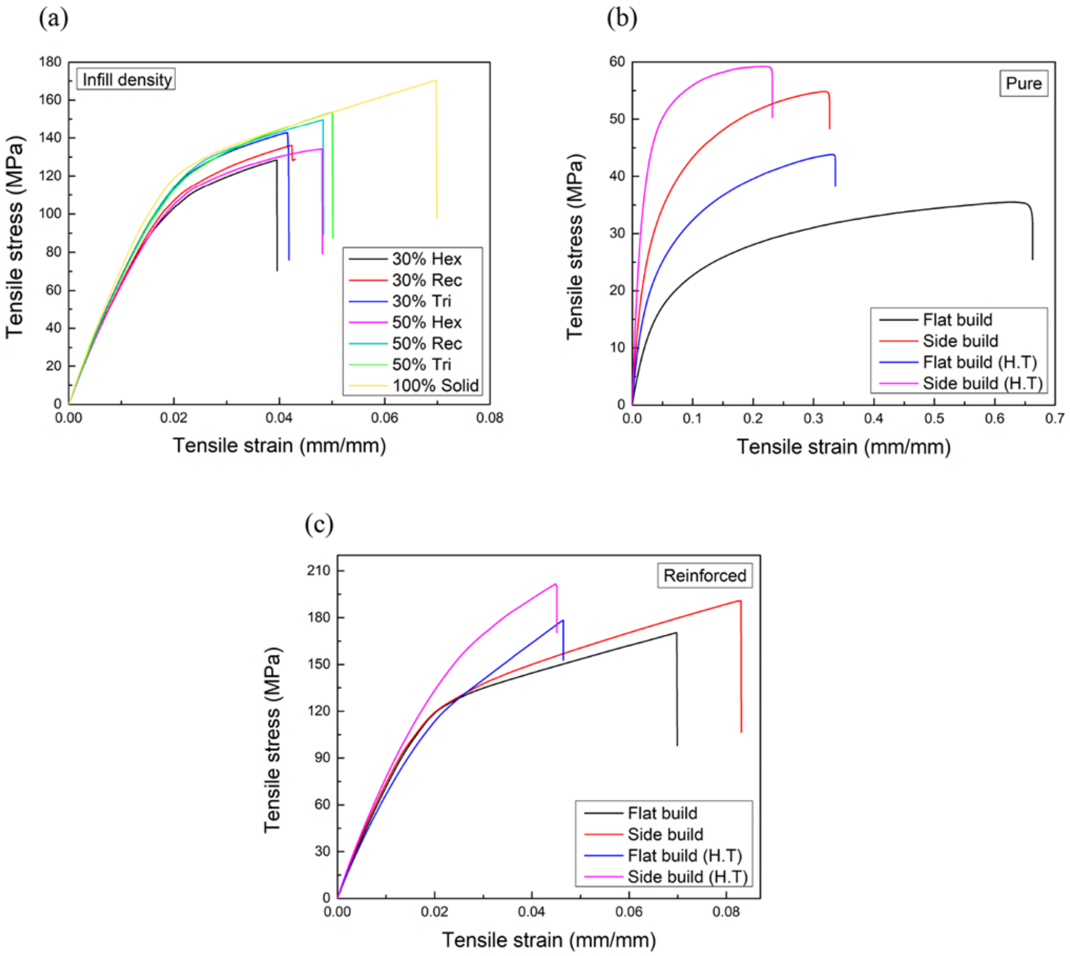

Figure 12. Stress–strain curves of varying infill density along with various infill patterns and different build direction of pure and reinforced AM Onyx specimens. (a) Infill density along with different fill patterns, (b) Pure flat and side build direction before and after heat treatment, (c) Reinforced flat and side build direction before and after heat treatment. (adapted from [114]).

1.3 Ceramics

Historically, additive manufacturing (AM) was primarily linked to polymers and metals. However, recent progress has expanded its capabilities to encompass ceramic materials, heralding a new era of opportunities. Ceramics find utility in diverse applications, spanning the chemical industry, manufacturing, electronics, aerospace, and biomedical engineering, owing to their numerous exceptional attributes. Their material adaptability is a result of their remarkable characteristics, encompassing high mechanical strength and hardness, robust thermal and chemical stability, as well as the potential for remarkable thermal, optical, electrical, and magnetic performance [25,115].

Dadkhah et al. [116] focuses on the challenges and advancements in AM of ceramics compared to polymers and metals in a review article. It provides a comprehensive overview of recent AM technologies for producing ceramic components with complex shapes. Ceramics pose unique challenges in AM due to their high melting temperatures and brittleness. Layer thickness, building orientation, and filament width are some of the process parameters that have an impact on the quality of printed ceramic items. It could be necessary to perform post-processing to get a smooth surface. Despite these difficulties, FFF has found use in a variety of industries, including as sensors, pharmaceutical delivery, aerospace, and orthotics. The process chain for creating ceramic AM parts primarily comprises five key steps [117,118]:

a. Material Selection: This involves choosing the appropriate ceramic material, which can be in the form of either powder with binders, fillers, and surfactants or as a commercially available filament.
b. Compounding and Rheological Characterization: Before proceeding, it's crucial to ensure that the material possesses the desired flow properties. This

step involves compounding and rheological characterization to verify the material's suitability.

c. Filament Extrusion: In cases where a mixture of ceramic powder and binder is employed, filament extrusion is employed to create a feedstock suitable for 3D printing.
d. 3D Printing: The prepared feedstock is then used for 3D printing, where layer-by-layer deposition takes place to build the desired ceramic part.
e. Debinding and Sintering: Following the 3D printing phase, the part undergoes debinding and sintering processes. These steps are essential to achieve the final ceramic part with the desired properties.

This process chain represents a comprehensive approach to ceramic AM, encompassing material selection, preparation, and the actual printing and post-processing steps required to produce high-quality ceramic components. The study of process parameters, coupled with the analysis of the rheological and thermal characteristics of ceramic filaments, constitutes pivotal aspects in the successful fabrication of high dense ceramic parts through MEX [119,120]. This is essential to prevent cracking during debinding and sintering processes and to achieve components with superior mechanical properties [121–124]. Once the optimal process parameters have been determined for achieving desired mechanical properties, it becomes essential to validate these parameters for printability across various shapes and assess their effectiveness in successfully sintering complex geometries as investigated in [125].

Particularly in engineering applications demanding high mechanical and thermal insulation performance, Zirconium Oxide (ZrO_2), also known as Zirconia, emerges as the most suitable ceramic material choice. A small amount of yttrium oxide unlocks the tetragonal polymorph and improves the mechanical properties, allowing for the formation of materials suitable for advanced ceramic applications [115,126].

The flexural characteristics of TZ-3YS-E tetragonal zirconia powder stabilized with 3 mol% yttria were studied by Cano et al. [127]. The powder had a specific surface area of 7.2 m^2/g and an average particle size of 90 nm [128]. A multicomponent binder system made of a commercial thermoplastic elastomer compound (TPE) and polyolefin grafted with a polar component was added to the powder to promote adhesion. The impact of raster orientation on the characteristics of MEX zirconia pieces was examined by the researchers. Different characteristics of the ceramic feedstock and sintered pieces were measured as bending bars with raster orientations of 0°, 4°, and 90° were produced. The rheological properties and thermal degradation behavior were altered by the powder's inclusion into the organic binder. At a shear stress of approximately 0.25 MPa, pressure oscillations were seen during the rheological measurements of the feedstocks, leading to porosity inside the roads during MEX shaping. Inter-road faults, under- and over-extrusion defects, and shearing-off flaws of the deposited material in the first layer were the three types of defects created during the printing phase (see Figure 13). The shape and position of these faults were altered by the variation in filament diameter, which in turn had an impact on the specimens' bending strength. The first layer's quality was significant for the bending behavior of the parts, with surfaces normal to the applied stress, poor bed leveling, changes in filament diameter, and shearing-off of deposited material leading to fluctuations in strength values. Compared to parts printed with a 90° orientation, those created with a 0° orientation were less dependent on these defects. Pores within the specimens led to failure when the tensile side was fault-free. The direction of infill roads in relation to the applied loads must be taken into consideration to construct sturdy and dense components utilizing MEX. By reducing inter-road faults, using filaments with strict dimensional tolerances, and controlling over-extrusion, flaws can be minimized.

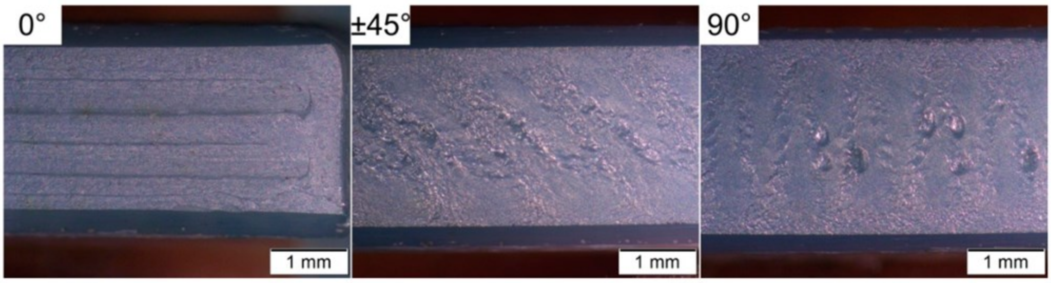

Figure 13. Defects on bottom layer of sintered bending specimens with 0°, ±45° and 90° raster orientation (adapted from [127]**).**

In pursuit of optimizing printing parameters to achieve high-density components, Nötzel et al. conducted extensive research in the realm of ceramic additive manufacturing [129,130]. Their investigations encompassed not only alumina but also zirconia, culminating in the establishment of a well-defined process chain. Nötzel et al. in [118] developed a comprehensive process for creating sintered zirconia components, which involved several stages: material selection, compounding and rheology analysis, filament extrusion, 3D printing, debinding, and sintering. Precise control of printing parameters, such as filament diameter within ±0.1 mm tolerance, was crucial for quality. Highly filled filaments were used to minimize the impact of viscoelastic polymers on extrudate swelling. The following FFF printing parameters were assessed to ensure optimal component quality, including bulk, surface, and corners:

- Print head extruder temperature: Below 170°C
- Printing speed: 10 mm/s
- Platform temperature: 70°C
- Smallest nozzle diameter: 0.4 mm
- Layer height: 0.1 mm

It's worth noting that some of these parameters have a very narrow operating range. Decreasing the print head extruder temperature leads to extrusion difficulties, including grinding and filament fracture. Conversely, elevated temperatures result in the evaporation or decomposition of wax and SA. The platform temperature is ideally maintained within the range of 60–75°C, and the printing speed should not exceed 10 mm/s. Exceeding this speed can necessitate higher pressure for material conveyance in the nozzle, potentially leading to filament fracture or grinding issues. Importantly, no clogging was observed within the prescribed printing parameters.

After printing debinding and sintering, was carefully executed at controlled heating and cooling rates of 0.2 °C/min and 5 °C/min for thermal debinding and sintering respectively. Small heating rates are essential to prevent the development of internal stress caused by the thermal expansion coefficient mismatch between the ceramic and the binder, as well as the evolution of gaseous decomposition products and the associated significant volume increase. The resulting sintered zirconia parts exhibited various structural features, analyzed for density using the Archimedes method, with approximately 99% density achieved, indicating successful void filling. The geometry of the sintered specimens have been measured and an average value of 20.90% of shrinkage was registered. Microscopic examination revealed the presence of irregularly shaped voids due to changing printing directions (45°), but these were partially filled.

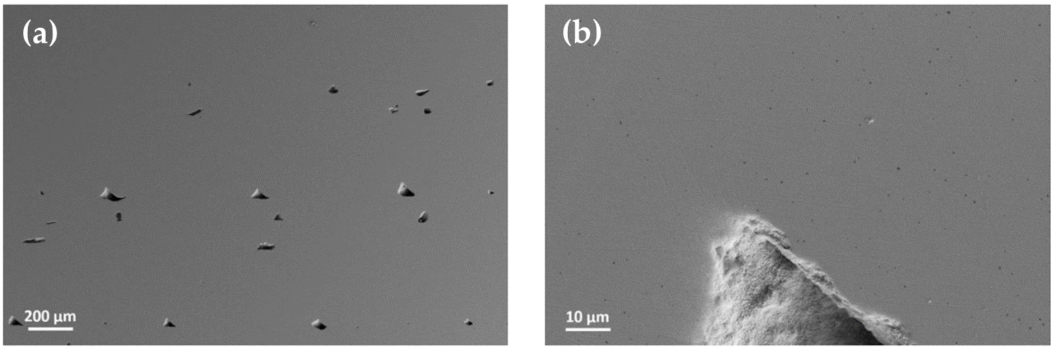

Figure 14. Micrograph of a sintered disc with 99 % of sintered filaments density: (a) voids; (b) pores. (adapted from [118]).

Surface quality examination of green zirconia parts showed well-packed filaments without visible defects. In summary, the study demonstrated the feasibility of using MEX for high-density zirconia parts, offering design flexibility and rapid prototyping as an alternative to traditional powder injection molding.

Hadian et al. [125,131,132] have also conducted extensive research in the field of ceramic manufactured through MEX, with a particular focus on Zirconia. Like Nötzel et al., Hadian utilized zirconia powder from Tosoh Corporation (Japan) [128] for the feedstock preparation. However, distinguishing their work, Hadian explored the use of different binders, further expanding the repertoire of binder materials for ceramic MEX processes. The study's primary goal in 2021 was to streamline the entire production process for massive ceramic structures, from 3D printing to debinding and sintering. The investigation began with the creation of filaments from zirconia powder that had been partially stabilized by yttria and an EVA-based binder. Various EVA grades were carefully chosen to modify the filament's properties. Critical variables like nozzle temperature, printing speed, and extrusion multiplier were extensively optimized. Viscosity is known to be inversely related to temperature in thermoplastic ceramic feedstocks. A higher viscosity requires more force to push the filament, which might cause buckling or filament fracture [133]. The printing studies indicated no filament buckling at nozzle temperatures of 180 °C. However, buckling was seen above a printing speed of 10 mm/s at this nozzle temperature, thus a printing speed of 8 mm/s was chosen. According to Gorjan et al. [20], stearic acid breakdown begins at 200 °C, which was another reason why 180 °C was chosen as the optimal nozzle temperature. Dynamic infill approaches, defined as an individual extrusion multiplier for each layer, were also implemented to increase the flow rate for the initial layers (40% for first layer and 20% for second one) to reduce errors and improve printing quality. Biaxial flexural strength experiments were performed on sintered zirconia disks to determine their mechanical properties. The results of these tests were impressive, with an average biaxial flexural strength of 91 MPa and a modulus of 5.7.

For the fabrication of large zirconia structures, a 12 cm tall vase structure was designed and printed (see Figure 15-a). The weight and dimension were investigated before and after each stage of debinding. The relative mass loss values for solvent extraction and filaments showed similar binder losses, indicating no obstacles to suppress solvent access. However, a significant difference was observed for the wicking debinding stage, indicating that the efficiency of the partial debinding step is influenced by the dimensions of the vase structure. The filament had a higher surface to volume ratio than the vase structure, which facilitated diffusion during wicking debinding.

To investigate this effect, six printed disks (40 mm diameter and 2.5 mm thickness) were solvent debound and placed inside an alumina powder bed. After wicking debinding, a similar color gradient was observed in partially debound disks. Weight loss calculations showed that a higher binder removal occurred in disks placed at the top of the powder bed with a darker color after debinding, as shown in Figure 16-b. No structural defects were observed in the final sintered structure, but further investigations are needed to study color change during the wicking debinding stage.

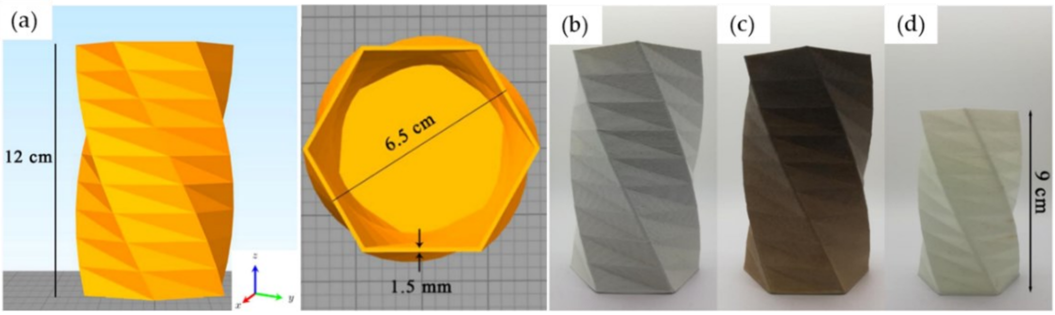

Figure 15. (a) large vase structure view from slicer; vase structure after: (b) printing; (c) debinding and (d) sintering at 1400 °C (adapted from [132]).

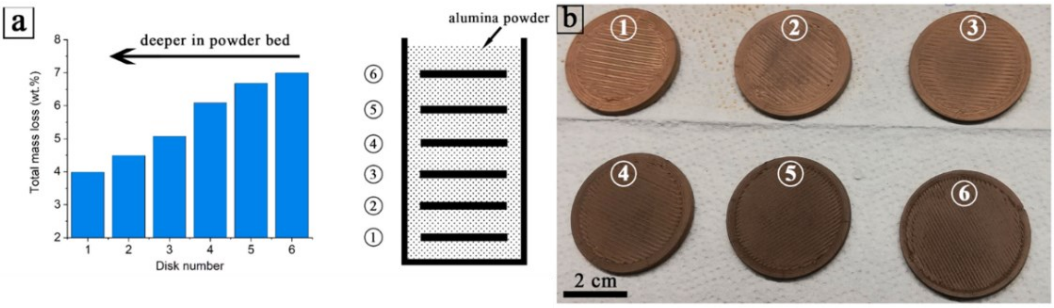

Figure 16. (a) Mass loss wt% of printed disks placed in different position inside the crucible after solvent and wicking debinding (b) color gradient of disks after wicking (adapted from [132]**).**

The shrinkage values show that the structure experienced a higher shrinkage than the net shrinkage observed in [22], which was due to the use of a ceramic powder content. It was discovered that the material had a shrinkage value of 23%.

In 2022, Hadian et al. [131] conducted a study on the use of Ceramic Injection Molding (CIM) binder compositions for creating feedstocks with 45 vol% ceramic powder loading for MEX of zirconia samples. They used a screw-based printing head to produce dense disk structures for mechanical ring-on-ring analysis. The study found that feedstocks based on Embemould K83G and Embemould K84G exhibited phase separation during processing and were excluded from 3D printing experiments. Instead, Embemould CC and Embemould M-based pellets were utilized. For comparison, disk samples were printed using a 1.75 mm-diameter commercial zirconia filament from Fabru GmbH (Switzerland).

A new characterization of printing parameters was conducted utilizing feedstock formulated with the Embemould CC binder composition (EmCC-P). It was observed that the slope is steeper at lower flow rates compared to higher ones, and that higher temperatures led to decreased material output because of increased leakage flow and bridging of partially melted feedstock pellets close to the hopper area. However, material output could be maintained consistently even with low-cost commercial pellet extruders by adjusting the multiplier before printing parts.

During solvent debinding, the integrity of printed disks based on the Embemould M binder composition was compromised due to delamination of the printed layers. By employing a post-printing process involving solvent debinding, partial debinding, thermal debinding, and sintering, zirconia disks were successfully manufactured without the introduction of cracks and blisters.

For mechanical ring-on-ring analysis, all printed disks exhibited a low Weibull modulus (EmCC-P m=4.3, filament m=3.5), primarily attributed to sample setup and surface roughness. Disks fabricated with EMCC-P binder composition displayed also significantly lower flexural strength (EmCC-P σ=203 MPa, filament σ=531 MPa). Fractography studies revealed failures near the loading ring area, indicating uneven stress distribution during ring-on-ring measurements. Scanning Electron Microscopy (SEM) fractography confirmed poor fusion between the printed layers as the main reason for inferior mechanical performance, particularly in samples fabricated with the EmCC-P composition (see Figure 17). The researchers suggest that the commercial CIM binder composition is suitable for fabricating ceramic feedstock for MEX technology, but it may have lower mechanical strength compared to conventionally shaped ceramics.

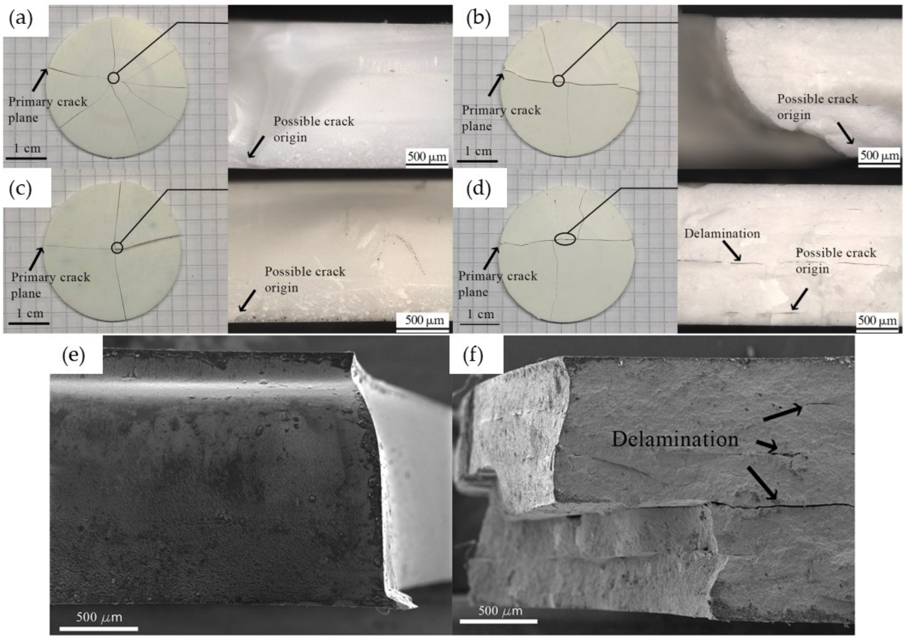

Figure 17. Image Analysis on disks printed with (a, c) filament and disk printed with (b, d) EmCC-P. Images (a, b) show the specimens with the highest flexural strength and images (c, d) the specimens with the lowest. SEM images of lowest flexural strength value of specimen manufactured with (e) filament and (f) EmCC-P (adapted from [131]).

To improve mechanical properties, they recommend customizing the CIM binder composition to enhance fusion during the printing process, making the ceramic parts more competitive.

Guan et al. [124] investigated the effect of different powder solid load on filament mechanical properties. Zirconia powder used in the study containing 3 mol% yttria had an average particle size of 0.5 μm and a specific surface area of 7.2 m^2/g. A multi-component organic binder was created using several formulas of high-density polyethylene, SEBS, paraffin wax, stearic acid, and dibutyl phthalate. Three distinct solid loadings of zirconia powder (78 wt%, 80 wt%, and 82 wt%) were evaluated. The filament with a solid loading of 82 wt% was the best among the three for producing complex-shaped zirconia components, with 20% SEBS and 45% PE in a complete organic binder. The rheology and stress-strain behavior of the filament with various solid loadings were compared. The debinding temperature was set at 40 C to provide fast solvent debinding while avoiding swelling and cracking. Pores or cracks caused by insufficient interlayer bonding and triangular voids generated at the junction of three extrusion routes were two faults associated with the FFF method. For the 82 wt% feedstock, 3Y-TZP with a relative density of 99.1%, shrinkage of 26.7%, and three-point flexural strength of 492.8 40 MPa was produced. Density and mechanical properties of all the specimens are shown Table 3.

Table 3. Density and mechanical properties of the zirconia ceramic with different solid loading from [124].

Solid	Relative density of	Shrinkage	Flexural	Vickers
78%	97.2%	29.7%	206.3±25	10.94
80%	97.9%	28.4%	311.1±36	12.12
82%	99.1%	26.7%	492.8±40	13.14

Three commercial YSZ (Yttria-Stabilized Zirconia) filaments from SiCeram GmbH, PT+A GmbH, and Fabru GmbH were investigated by Clemens et al. [134] to determine the printing and post-processing behavior while using a cup as a benchmark. This cup's design has various wall thicknesses, which might cause varied solvent debinding behaviors and thermal treatment-induced deformation. The density and bending radius before break of the filaments were all examined. Diameter of the filaments were found to be all the same at 1.75±0.05 mm. All data are reported in Table 4.

Table 4. Characterization of the YSZ filaments from [134]

	SiCeram GmbH	PT+A GmbH	Fabru GmbH
Density [g/cm^3]	3.52 ± 0.01	3.52 ± 0.01	3.20 ± 0.01
Bending radius [mm]	60±5	60±5	<16

The flow behavior of the three different thermoplastic YSZ materials was evaluated using a rotational rheometer, with rheological behavior tested at three different temperatures. Based on all the findings, it can be concluded that the SiCeram and

PT+A filaments behave similarly. Also the mass loss beginning and offset temperatures for both YSZ filaments are comparable, according to the STA (Simultaneous Thermal Analysis) studies, which is noteworthy. It's also worth highlighting that debinding and sintering parameters are readily available for SiCeram and Fabru filaments, whereas the datasheet for the PT+A YSZ filament includes just temperature windows. As a result, SiCeram and Fabru filaments were selected for the creation of cups for the future printing assessments. Cup were printed on an FFF printer with certain parameters kept constant, while others were adjusted based on the analysis done on each filament, see Table 5. The constant parameters included a 0.6 mm nozzle diameter, a 0.2 mm layer height, a 0.75 mm extrusion width, a 20% infill percentage, and a 30mm/s printing speed.

Table 5. Variable printing parameters based on thermal and rheological analysis.

	SiCeram	**Fabru**
Extrusion multiplier	0.92	0.95
Nozzle temperature [°C]	145	180
Bed temperature [°C]	45	40
Cup size [mm] (due to different shrinkage)	77.65 × 85 × 65	81.7 × 89.4 × 68.4

Due to the brittleness of SiCeram filament, which frequently broke during extrusion, printing SiCeram filament presented challenges. Only one sample larger than a 1 kg spool was successfully produced. As shown in Figure 18, the ceramic cup printed with SiCeram filament failed after 24 h solvent debinding, showing cracks on bottom surfaces and walls. The shrinkage value for the only sintered cup (Fabru filament) was determined to be 24.3%, little more compared to 23.7% determined on the filament.

In conclusion, as excessive viscosity can cause problems like buckling and filament abrasion, the viscosity of printing materials is crucial to the success of 3D printing. When users choose the ideal printing temperature for new filaments, viscosity data is invaluable. The 3D printing of ceramic things like cups is possible regardless of how brittle or flexible ceramic filaments are. However, brittle filaments frequently have a high rejection rate because of filament breaks, which makes it difficult to print continuously without adding faults.

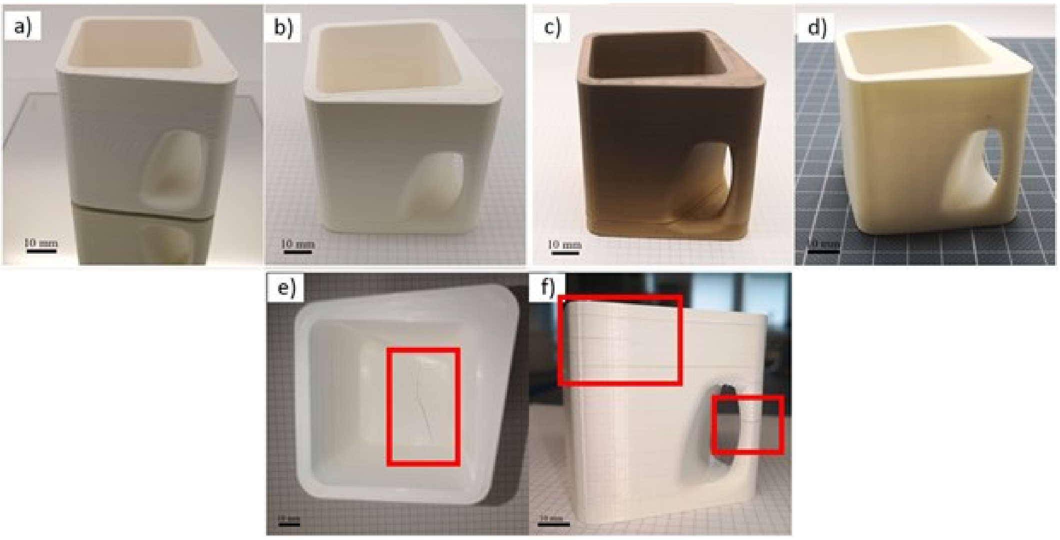

Figure 18. Picture of the printed 3D cup using YSZ Fabru filament after a) printing, b) solvent debinding, c) wick debinding and d) sintering. e) and f) show crack on cup printed using SiCeram filament (adapted from [134]**).**

Chapter 2

INFLUENCE OF PRINTING PARAMETERS ON THE THERMAL PROPERTIES OF POLYMERS

This chapter focuses on thermal characterization of 3D-printed parts produced via Material Extrusion Additive Manufacturing with variable printing parameters. Notably, thermal conductivity measurements reveal how factors like infill percentage and layer number impact thermal behavior. As a result of this research, "Effect of process parameters on the thermal properties of material extruded AM parts" has been published to disseminate these findings [135].

2.1 Materials and methods

A complete 4^2 factorial Design of Experiments (DoE) was used to investigate how the number of layers and infill percentage affected the thermal conductivity of $70 \times 40 \times 10$ mm^3 prismatic parts, as shown in Table 6.

Table 6. Complete factorial Design of Experiments for thermal conductivity analysis.

Factor	Level			
Layer number	2	4	6	8
Infill percentage [%]	20	40	60	80

The specimens were made using commercial black PLA 1.75 mm filament (AzureFilm d.o.o., Slovenia). Before beginning the printing process, the filament underwent a 4-hour drying process at 40°C in an oven and was then stored inside a vacuum-sealed enclosure to ensure the mitigation of any potential moisture-related issues. The samples were manufactured with a commercial 3D printer, the Flying Bear Ghost 4S, developed by Zhejiang Flying Bear Intelligent Technology Co., Ltd. This printer boasts a voluminous build space measuring 255 × 210 × 210 mm^3. Employing a 0.4 mm brass nozzle and a Polyetherimide (PEI) print bed, it was configured to ensure robust adhesion while minimizing undesirable warping phenomena. A variety of initial evaluations were made before choosing the printing parameters. To maintain dimensional accuracy and achieve acceptable quality, the line width was set at 0.4 mm to match the nozzle's 0.4 mm diameter. The layer height was then adjusted at half the line width. Anisotropy between the top and lower layers was only slightly reduced by using a crosshatch raster approach with angles of 45°, as shown in Figure 19. A wall layer value of three was configured in the slicer (Ultimaker Cura) to enable secure bonding of the shell and ensure its resistance to outside forces. Lower numbers are considered insufficient, whereas higher values can increase the part's longevity and ability to endure external stresses. The number of top and bottom layers as well as the infill percentage were changeable variables during the printing of the samples, but all other process variables remained constant. Notably, "infill percentage" refers to the amount of material used to fill the interior of the object, while "top and bottom layers" refer to the layers that make up the upper and lower surfaces of the printed object, respectively. A complete list of the values for the process parameter is shown in Table 7.

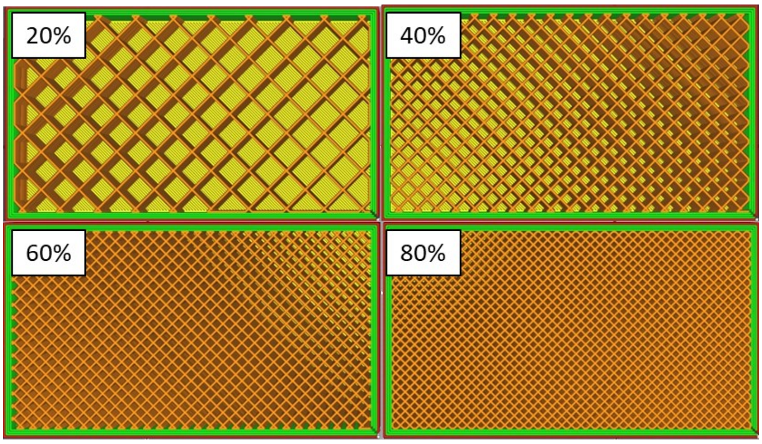

Figure 19. Infill layer raster strategy and percentage, 20% to 80%.

Table 7. Optimized process parameters.

Process parameter	Value	Unit size
Nozzle temperature	210	[°C]
Bed temperature	60	[°C]
Printing speed	60	mm/s
Layer height	0.2	mm
Line width	0.4	mm
Infill strategy	Grid	-
Layer raster strategy	-45°/+45°	-

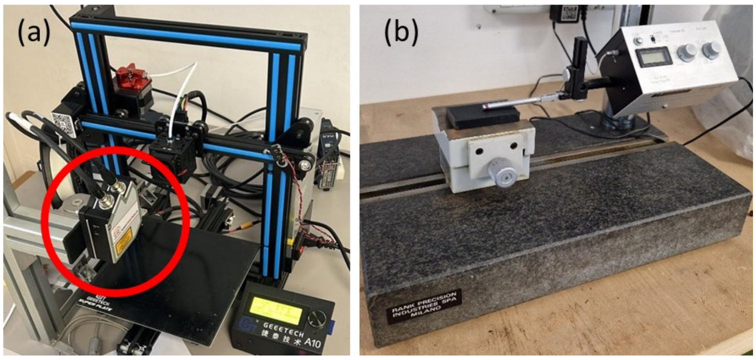

Figure 20. (a) Micro-Epsilon scanControl 2900-50 BL used to acquire 3D profile; (b) Taylor-Hobson Surtron 3P surface roughness profilometer.

The scanControl 2900-50 BL (Micro-Epsilon Messtechnik GmbH & Co. KG), a 2D/3D blue laser scanner and profilometer designed for measuring semi-transparent, red-hot glowing, and organic materials with a 405 nm wavelength laser, was used to measure the sample surface due to the characteristics of the material. Given the direction in which the object's height is growing, the scanner has a resolution of 4 µm on the Z-axis and 1,280 points/profiles on the X-axis. To confirm the earlier measurements, the top surface roughness Ra of the specimens was again measured using the Surtronic 3P surface roughness profilometer (Taylor-Hobson, UK) with a cut-off value of 0.8mm (see Figure 20).

Without sample preparation, the Linseis Messgeräte GmbH (Germany) Transient Hot Bridge (THB) equipment detected the thermal conductivity. The THB technique calculated the amount of time needed for a thermal signal to go through a sample of material. By giving the thermal bridge, which exchanged heat with the sample, a brief heat pulse, the measurement was carried out dynamically. The material's thermal characteristics were then determined using the length of time it took for the thermal signal to travel through the sample. The instrumentation included a flexible sensor (THB-B type) that was manually clamped between two flat specimen surfaces to guarantee good thermal contact without air inclusions (see Figure 21). The sensor's dimensions are 42 mm by 22 mm, its thermal conductivity range is 0.1 to 2 W/m × K, and its temperature range is -150 to 200 °C.

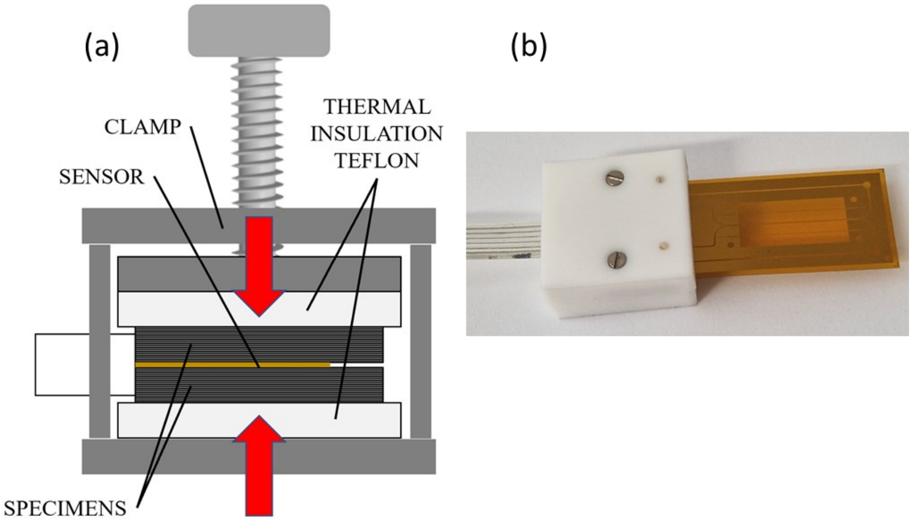

Figure 21. (a)the functioning scheme of the THB system; (b) flexible sensor THB-B used.

According to the UNI EN ISO 22007 [136], the tests were carried out at room temperature with an execution duration of 160 s and a pulse supply current of 50 mA. To create an offset-free output, a Wheatstone bridge is forced out of balance by a non-uniform temperature profile. A heater *RH* produced a temperature field that was time- and distance-dependent along the sensor and the test object. Additional resistors were connected to a Wheatstone bridge with a bridge voltage *UB* dependent on the temperature difference ΔT. Measuring the temperature difference ΔT enabled the calculation of thermal conductivity λ using the following formula:

$$\boldsymbol{\lambda} = \frac{\boldsymbol{\Phi}}{\mathbf{2} \times \boldsymbol{\pi} \times \Delta \boldsymbol{T}} \times \boldsymbol{k} \tag{1}$$

The heater *RH* generated the applied thermal power Φ supplied with current, while k was the sensor calibration factor. The direction-dependent thermal diffusivity of anisotropic materials can be measured thanks to the improvement of the THB evaluation. The determination of thermal diffusivity in all three directions is possible with this novel technique, which simply calls for plate-shaped specimens [137,138]. It is significant to note that due to warping phenomena seen during the printing process, the tests were carried out on the specimen's top surface, which corresponds to the last printed layer. Using four different infill percentages and doing the experiments on the top surface, more precise results were obtained.

2.2 Experimental results and discussion

Roughness analysis

It was important to conduct some preliminary research on the roughness of the surfaces prior to conducting tests to ascertain the thermal properties of the specimens. According to the relevant literature, this study was necessary to make sure that the specimen roughness values were within allowable bounds to prevent any potential influence on the measurement of thermal properties.

The UNI EN ISO 21920 [139] was followed for all measures to guarantee precision and consistency. To determine the effect of roughness on the thermal conductivity values, preliminary tests were run on specimens with 100% infill (see Table 8). Three sections (20×20 mm^2) of the object were sampled, and a roughness profile was obtained using laser scanning and measured. To prevent measurement mistakes caused by edge effects in the 3D-printed specimens, the sections were obtained in areas far from the edges. The specimens with increased roughness from contact with the rough-textured PEI plate exhibited lower heat conductivity data, indicating that roughness was a significant effect. The greatest values of the three measurements, like those obtained from printed top layers, were instead reported by specimens printed on the PEI plate with a smooth texture. This surface roughness study also checked the general quality of the samples and the distribution of roughness values.

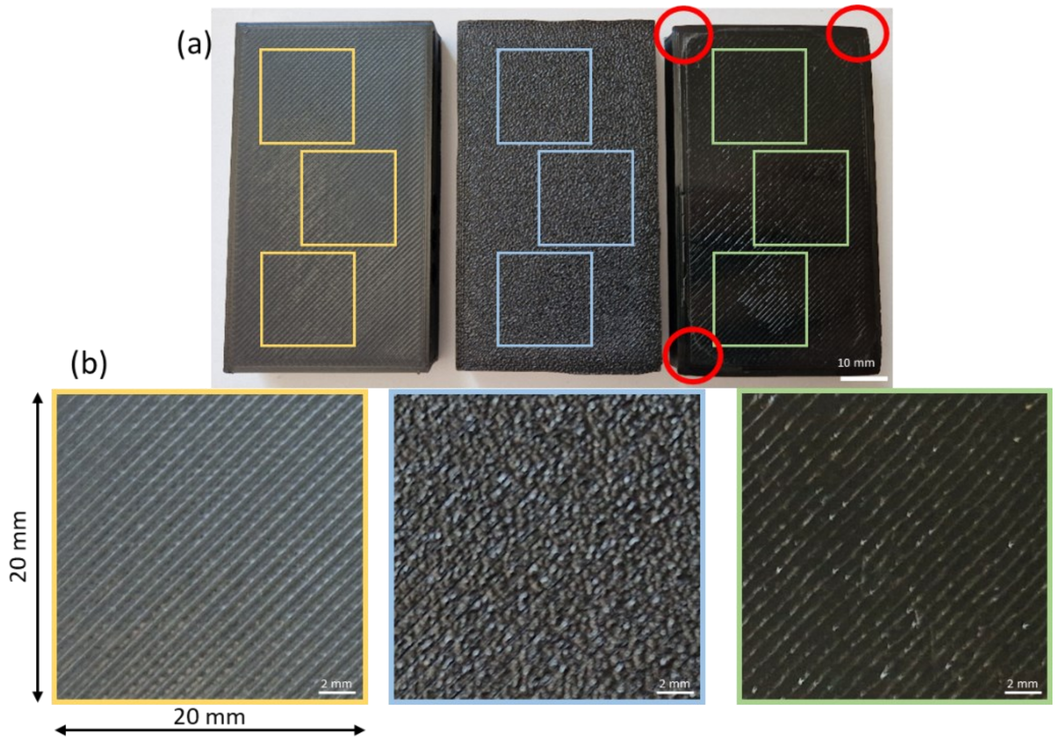

Figure 22. Roughness evaluation, areas analyzed are highlighted. (a) picture of the three different textures with warping phenomena highlighted in red on Smooth PEI sample. (b) zoom of measured area, from left to right, Top layer, Rough PEI, Smooth PEI.

Table 8. Roughness and thermal conductivity values of 100% filled samples.

	Top	Rough	Smooth	Injection	Unit
Roughness R_a	3.62	7.96	2.19	1.06 Ref.[140]	[μm]
Thermal conductivity	0.186	0.141	0.189		[W/m×K]

Considering the non-homogeneity of the results on the smooth PEI, caused by the warping phenomena, top layer surface was selected as the surface to analyze for the thermal conductivity tests. Inspection of the printed samples was then conducted on DoE samples. The roughness values were Rz = 15.6 μm and Ra = 3.61 μm (see Figure 23), respectively. Measurements using the Surtronic 3P profilometer, which produced similar Ra values to those obtained with the scanControl 2900-50 BL, were conducted to compare these data.

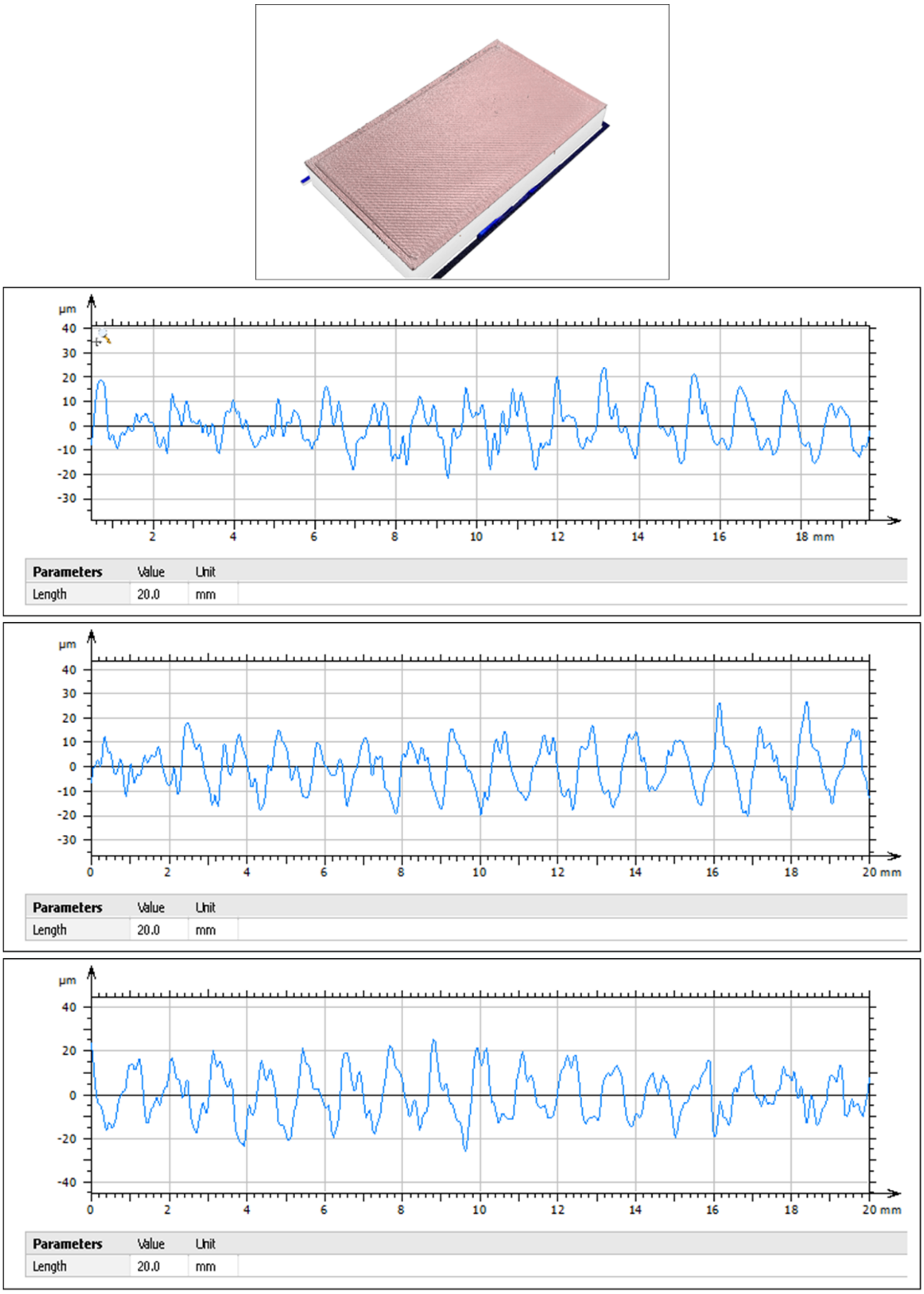

Parameters	Value	Unit
Length	20.0	mm

Parameters	Value	Unit
Length	20.0	mm

Parameters	Value	Unit
Length	20.0	mm

Figure 23. Surace acquisition of top layer surface from scanControl 2900-50 BL and roughness profiles (3 area of 20 × 20 mm^2)

Thermal properties evaluation

It was important to conduct some preliminary research and calibration on a full 100% infill PLA sample to determine the penetration depth value and so verify if the selected sample thickness was acceptable to determine the thermal properties.

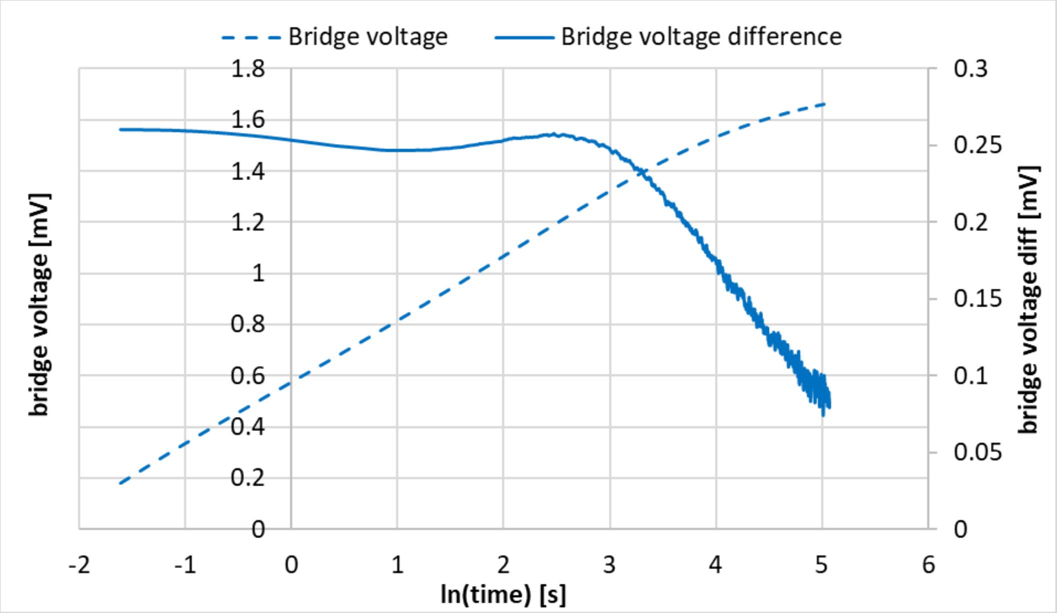

Figure 24. The graph represents the voltage generated at the ends of the bridge as a function of time on 100% infill sample, thickness 10mm.

The value of penetration depth found was of 7.2071 mm, the thickness of 10 mm was correctly selected. The selection of the infill type was another crucial factor considered. Because the fundamental benefit of MEX is the ability to generate complicated or lightweight structures, test samples weren't printed entirely full. Therefore, it was crucial to investigate the thermal conductivity of lightweight samples with various infill percentages and top/bottom layer counts to see how the measured values correlated with one another and to reduce material waste while improving optimization. Results are shown in Table 9

Table 9. Thermal conductivity results from DoE.

Sample ID	n. of layers	Infill percentage [%]	Thermal conductivity
PLA L2 R20	2	20	0.0690
PLA L2 R40	2	40	0.0946
PLA L2 R60	2	60	0.1109
PLA L2 R80	2	80	0.1381
PLA L4 R20	4	20	0.0908
PLA L4 R40	4	40	0.1128
PLA L4 R60	4	60	0.1342
PLA L4 R80	4	80	0.1415
PLA L6 R20	6	20	0.1047
PLA L6 R40	6	40	0.1314
PLA L6 R60	6	60	0.1461
PLA L6 R80	6	80	0.1607
PLA L8 R20	8	20	0.1343
PLA L8 R40	8	40	0.1535
PLA L8 R60	8	60	0.1693
PLA L8 R80	8	80	0.1736

Table 10. Statistical analysis results.

	Estimate	Lower 95%	Upper 95%
Intercept	0.12985	0.12501	0.13468
layer_number(2,8)	0.02726	0.02501	0.0295
layer_number×layer_number	0.00318	-0.0015	0.00782
infill_percentage(20,80)	0.02642	0.02417	0.02867
infill_percentage×infill_percentage	-0.0044	-0.0091	0.00023
layer_number×infill_percentage	-0.0073	-0.0099	-0.0048
R^2	0.9928		
Mean squared error	0.0034		

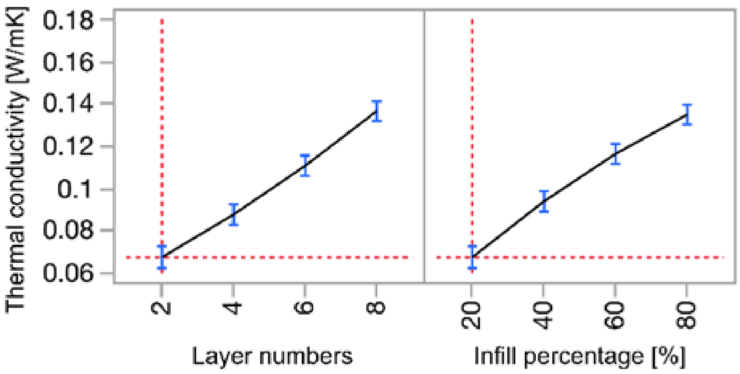

Figure 25. Statistical analysis results.

Table 10 and Figure 25 present the statistical analysis findings graphically. The regression model's R^2 coefficient is 99.28%. The analysis of the expected values in comparison to the observed values is shown in the figure. The fact that these variables were linear suggests that the model that was used to produce the anticipated values was a good match for the observed data. The proximity of the data points to the regression line demonstrated this linearity. The slope of the regression line also indicates that although the difference was not statistically significant, the observed values tend to be slightly higher than the expected values. Figure 26 demonstrates that the model correctly anticipated the values that were observed. Thermal conductivity and the percentage of infill were found to be linearly correlated. As the infill % increased, the rate of change in thermal conductivity likewise increased at an increasing rate, as seen by the trend line for the data having a convex growing structure. This study indicated that increasing the infill % might greatly enhance the thermal conductivity of the material. This conclusion matched those in the literature, and it may be explained by the fact that air has a very poor thermal conductivity. The volumetric proportion of air grew as the infill percentage increased, decreasing the specimen's overall thermal conductivity (at the price of the PLA component).

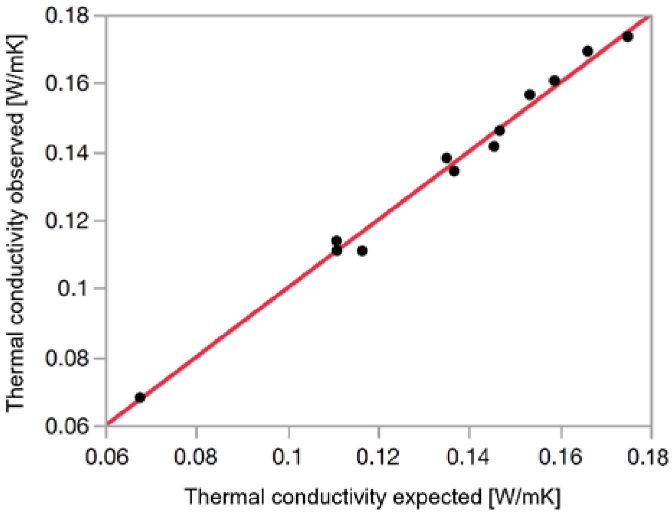

Figure 26. Thermal conductivity expected vs. observed analysis.

Similar to how heat contacted the insulating layer of air later, as the number of surface layers increased, the thermal conductivity increased. It is important to note that the data's trend line has a concave rising shape, indicating that as the number of layers rose, the rate of rise in thermal conductivity slowed down. As a result, it could be concluded that the more the component was filled, the better it could transmit heat through its thickness.

Mathematical Model

In the pursuit of understanding thermal conductivity in specimens with variable infill, experimental analysis serves as guiding light. Through systematic experimentation, intricate relationships governing heat transfer within the material are studied. Distilling observations, a concise mathematical model is constructed.

The thermal conductivity, denoted as k, the cross-sectional area of the specimen, denoted as A, the temperature difference across the specimen, denoted as ΔT, and the length of the specimen, denoted as L, define the parameters of interest.

The fundamental equation governing heat conduction, according to Fourier's Law, is expressed as:

$$\boldsymbol{Q = -k \cdot \frac{A \cdot \Delta T}{L}} \tag{2}$$

Where:

- Q is the heat transfer through the material.
- k is the thermal conductivity.
- A is the cross-sectional area.
- ΔT is the temperature difference.
- L is the length of the specimen.

In specific cases of AM, involving specimens with variable infill and top layers, one may encounter scenarios where the thermal conductivity varies within the specimen. In such instances, it becomes imperative to account for local variations in thermal conductivity. Let *k(x)* symbolize the thermal conductivity as a function of the position within the specimen, with *x* representing the position coordinate.

The heat transfer through an infinitesimally small element of the specimen can be articulated as:

$$\boldsymbol{dQ = -k(x) \cdot A \cdot \frac{dT}{dx} \cdot dx} \tag{3}$$

By integrating this expression across the length of the specimen *0* to *L*, the total heat transfer can be determined as:

$$\boldsymbol{Q = -\int_0^L k(x) \cdot A \cdot \frac{dT}{dx} \cdot dx} \tag{4}$$

This integral equation considers variations in thermal conductivity along the length of the specimen.

In the specific case analyzed, with variable infill and variable top layers the equation can be written as:

$$\boldsymbol{Q = -\left(\int_0^{L_{top}} k_{top}(x) \cdot A \cdot \frac{T_{mat} - T_{air}}{L_{top}} \cdot dx\right) - \int_{L_{top}}^{L} k(x) \cdot A \cdot \frac{T_{mat} - T_{air}}{L} \cdot f(x) \cdot dx} \tag{5}$$

Where:

- *Q* is the heat transfer through the material.
- *k(x)* is the thermal conductivity as a function of position within the specimen.

- A is the cross-sectional area.
- T_{mat} is the temperature within the material.
- T_{air} is the temperature within the air-filled portion of the specimen.
- L_{top} is the length of the top layers of the specimen.
- $k_{top}(x)$is the thermal conductivity of the material in the top layers.
- $f(x)$ is the infill factor, varying between 1 for 100% infill and 0 for 0% infill.

$k_{top}(x)$ and $k(x)$ can be considered as the weighted sum of the thermal conductivities of the material k_{mat} and air k_{air}

For the top layers, the formula is:

$$\boldsymbol{k_{top}(x) = f_{top} \cdot k_{mat} + (1 - f_{top}) \cdot \ k_{air}} \qquad (6)$$

where f_{top} represents the infill fraction of the top layers, equal to 1.

For the variable infill section, the formula is:

$$\boldsymbol{k(x) = f(x) \cdot k_{mat} + (1 - f(x)) \cdot \ k_{air}} \qquad (7)$$

Equation (5) is employed to assess the heat flux, enabling the calculation of the average thermal conductivity of the specimen. The formula for the average thermal conductivity k_{avg} in the specimen can be expressed considering the presence of materials with different thermal conductivities and their fillings.

The average thermal conductivity can be written as:

$$\boldsymbol{k_{avg} = f(x) \cdot k_{mat} + (1 - f(x)) \cdot \ k_{air} + \frac{L_{top}(x)}{L} \cdot k_{mat}} \qquad (8)$$

Where:

- $f(x)$ is the infill factor, varying between 1 for 100% infill and 0 for 0% infill.
- k_{mat} is the thermal conductivity of PLA.

- K_{air} is the thermal conductivity of air inside the specimen.
- $L_{top}(x)$ is the length of the top layers of the specimen.

This formula takes into account the composition of the specimen, where one part is composed of PLA, divided into a full 100% forming top layers and a variable infill percentage part, and the other part is composed of air. The average thermal conductivity is therefore a weighted combination of the thermal conductivities of these two components based on the material fraction present in the specimen.

2.3 Conclusions

In this study, the thermal conductivity characteristics of samples manufactured with filament-based MEX in PLA were examined. Keeping the other process variables constant, the impact of infill percentage and layer count on thermal characteristics was investigated. According to the findings, there is a linear relationship between thermal conductivity and both the number of layers and infill percentage. To completely understand the effect of anisotropy on thermal characteristics and its relationship with the number of surface layers, additional research is also required. Thermal conductivity measurements were quick and accurate thanks to the transient hot-bridge sensor. These results can be used to refine the additive manufacturing procedure and produce items with the desired internal thermal characteristics. For engineering applications with high heat generation and flow, this element is essential.

Chapter 3

INFLUENCE OF HEAT TREATMENTS ON THE MECHANICAL PROPERTIES OF PEEK PARTS

Techno-polymers are processed using a variety of methods, including additive manufacturing, and have wide uses in the aerospace, automotive, aviation, and biomedical industries. Polyether Ether Ketone (PEEK) is a semi-crystalline techno-polymer known for its exceptional mechanical properties and high-temperature endurance. Given that PEEK is semi-crystalline, heat treatments can be employed to improve its qualities. These treatments can be carried out in a standard oven or using the built-in annealing system within Fused Filament Fabrication (FFF) equipment. This study's main goal is to provide a better knowledge of how annealing procedures and the flexural characteristics of PEEK specimens made using FFF technology relate to one another. In this study, a direct annealing method used during the printing process is compared to a conventional oven annealing method that is carried out for a comparable amount of time. An evaluation of the relationship between flexural properties and annealing type and temperature is part of the assessment of flexural properties. "Preliminary test on the effect of direct annealing on additive manufactured PEEK bending properties" was published as a result of this study to share the results [141].

3.1 Materials and methods

To examine the effects of the direct annealing process and contrast it with the traditional one carried out in the oven, a factorial 2^2 DoE was utilized. Because the technique was still in the discovery stage, a 2^2 DoE was selected. The factors and relative levels chosen for the analysis are listed in Table 11, with three replications for each combination. The maximum temperature and the annealing type were factors that were investigated.

Table 11. Factorial design

Factor	Level	
Process	Direct Annealing (DA)	Oven Annealing (OA)
Temperature (°C)	200	300

PEEK KetaSpire® MS NT1 AM 1,75mm from Solvay SA (Brussel, Belgium), a natural filament capable of long-term performance up to 240°C, was the substance employed. Due of its strong resistance to corrosion, chemicals, heat, ductility, and dimensional stability, it can be used in places like oil and gas, aerospace, and automobiles as a metal alternative. The glass transition temperature is roughly 145°C, but the supplier's stated melting temperature is 343°C [142]. The spool was vacuum-packed until printing and dried for eight hours at 150°C in an air-circulating oven. The bending specimens' dimensions were 80 × 10 × 4 mm^3, as stated in UNI EN ISO 178 [143]. In a completely enclosed heated chamber, specimens were created using a Creatbot PEEK-300 (Henan Suwei Electronic Technology Co. Ltd., Zhengzhou, China), a coreXY 3D printer with a build volume of 300400300 mm3. A dual extruder system was included. The platform, chamber, and nozzles had maximum temperatures of 500°C, 200°C, and 120°C, respectively. The Direct Drive System was one of the machine's additional key characteristics. A commercial technology called Annealing System (DAS) is used to anneal the part during deposition. The supplier claimed that only CreatBot machines could use DAS technology because it was patent-protected. The region around the deposition nozzle on the final layer was kept at a predetermined temperature using a corona-shaped heating element (Figure 27).

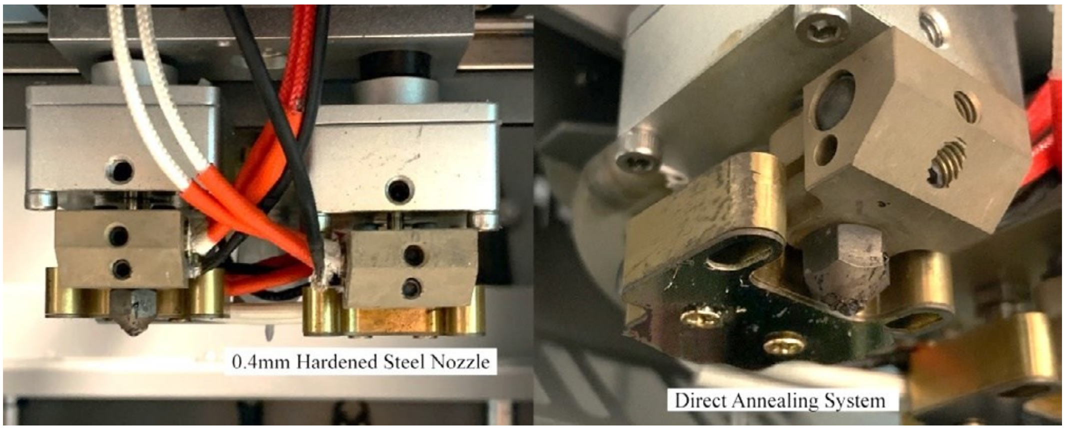

Figure 27. Direct Annealing System (DAS).

Table 12. PEEK specimen optimized printing parameters

Parameter	Value	Unit
Nozzle Temperature	430	°C
Platform Temperature	150	°C
Chamber Temperature	100	°C
Layer Height	0.2	mm
Line Width	0.4	mm
Wall Layer Count	3	-
Infill Density	100	%
Infill Angle Offset	-45°/+45°	-
Printing speed	20	mm/s

The direct benefit of annealing was strengthening the link between layers and preventing issues with layer delamination. A 0.4 mm hardened steel nozzle and a carbon fiber plate were used during the experiments. The adherence to the printing platform was tested in preliminary printing experiments. 15 brim lines were assured to adhere to the printing platform thanks to a special high-temperature glue. Using parameters from the literature, the first printing experiments were conducted and are shown in Table 12.

A total of fifteen samples were produced (see Figure 28-a). Six underwent direct annealing (DA), and the other six underwent a further oven treatment (OA). Three specimens were left untreated (UNT). The printing process took 40 minutes for each specimen. Because the hot crown performed the treatment as the tip deposited the fused filament, the direct annealing process time coincided with the printing time. To make the experiment findings comparable, the oven treatment time and the direct annealing time were used. The heating and the cooling rate used were equal to 5°C/min. The thermal cycle is reported in Figure 28-b.

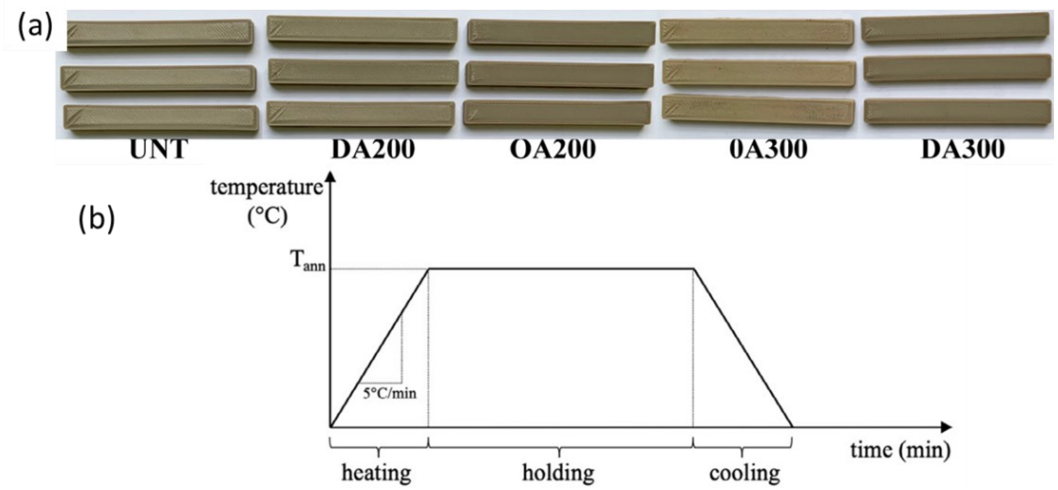

Figure 28. (a) PEEK bending specimens. (b) oven annealing thermal cycle.

Time and cost analysis

Additionally, time and cost concerns were examined (see Table 13).

Table 13. Table of printing and annealing times.

	Direct Annealing		Oven Annealing	
Time (min)	**200°C**	**300°C**	**200°C**	**300°C**
ID	DA200	DA300	OA200	OA300
Annealing time (t_{oven})	-	-	75	95

For each specimen and treatment, the printing time (t_{print}) was the same. The heating and holding times made up the annealing time in the oven. Hourly rates were correlated with 3D printing (C_p), direct annealing (C_a, C_{ca}), printing (C_{cp}), and ovens (C_o, C_{co}). The material's purchase price, which was the same for both techniques, was viewed as neglectable. A machine hour rate is an hourly cost in terms of factory overheads to operate a particular machine. It is obtained by dividing the factory expenses associated with the machine for a given period by the number of hours worked by the machine during that period. For this reason, the hour rates were the following:

$$C_p = \frac{printer\ purchase\ cost}{machine\ hours}$$

$$C_a = \frac{annealing\ equipment\ purchase\ cost}{machine\ hours}$$

$$C_o = \frac{oven\ purchase\ cost}{machine\ hours}$$

$$C_{cp} = \ printer\ electrical\ consumption$$

$$C_{ca} = \ direct\ annealing\ electrical\ consumption$$

$$C_{co} = \ oven\ electrical\ consumption$$

The production costs of a part with direct annealing C_{DA} and oven annealing C_{OA} were:

$$C_{DA} = C_p \times t_{print} + C_{cp} \times t_{print} + C_a \times \ t_{print} + C_{ca} \times t_{print} \qquad (1)$$

$$C_{OA} = C_p \times t_{print} + C_{cp} \times t_{print} + C_o \times t_{oven} + C_{co} \times t_{oven} \tag{2}$$

The formulas (1) and (2) have several elements in common (C_p, C_{cp}) that can be ignored to highlight the difference in cost between the two processes. The specific costs of the single treatments are, therefore:

$$C_{DAS} = C_a \times \ t_{print} + C_{ca} \times t_{print} \tag{3}$$

$$C_{OAS} = C_o \times t_{oven} + C_{co} \times t_{oven} \tag{4}$$

Assuming an hourly cost of 0.5 €/h for the direct annealing equipment, a direct annealing system power consumption of 80 Wh, a heat treatment oven hourly cost of 10.0 €/h, and an oven power consumption of 2,200 Wh, the treatment of the oven was significantly more expensive, with equation (2) greater than equation (1).

3.2 Experimental results and discussion

Mechanical Test

Three-point bending tests were performed to see how two different annealing processes affected the material's mechanical characteristics. Figure 29 show how much the heat treatment affected the results, make it evident that there were considerable differences in the flexural strength between the treated and untreated specimens. The untreated specimens' average flexural strength (designated as UNT) was calculated to be 124.43 MPa on average, with a standard variation of 6.75 MPa. The mechanical characteristics of thermoplastics were noticeably improved by the annealing procedure at high temperatures. This observation is consistent with the results of Butt and Bhaskar's [144] investigation on the effects of annealing on frequently used polymers. As a result, it was anticipated that PEEK's material properties would be enhanced. In comparison to the untreated specimens (UNT), the specimens that underwent annealing treatment in an oven at 300°C (referred to as OA300) showed a significant 16% increase in flexural strength. It is imperative to emphasize that interlayer bonding adhesion plays a pivotal role in mechanical testing for stress evaluation. The improvement in bonding adhesion translated into a reduction in material porosity, approaching the properties of the same material processed via injection molding [6].

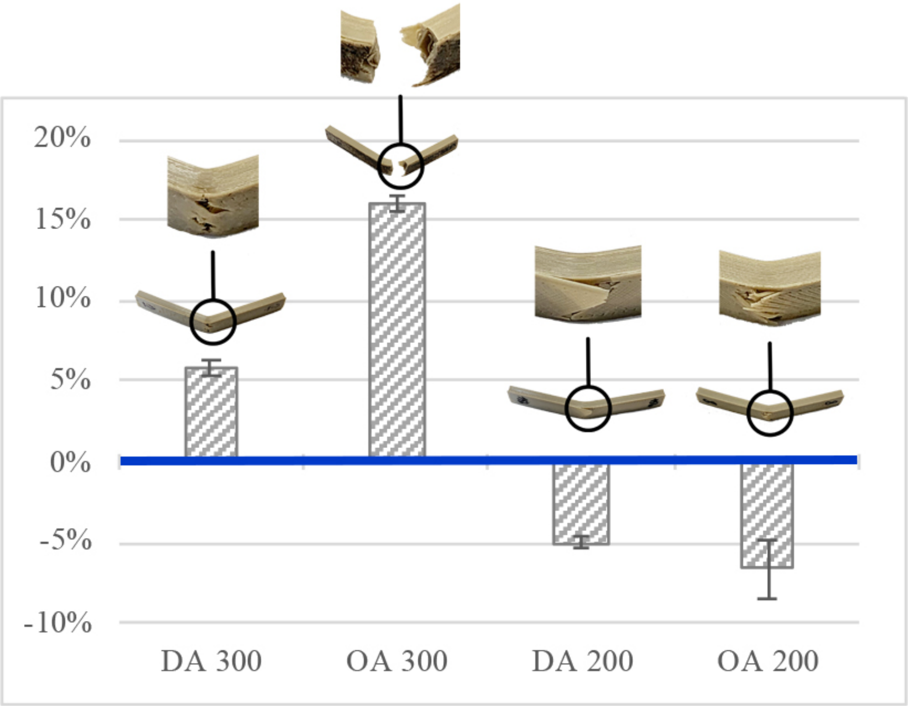

Figure 29. Percentage values of flexural strength of heat-treated specimens compared to untreated specimens (0%).

However, it is noteworthy that the specimens subjected to OA300 exhibited a more brittle behavior, with 66% of the specimens experiencing failure. Conversely, all the other samples did not reach specimen failure by the conclusion of the test. As opposed to the OA300 specimens, the specimens that underwent direct annealing treatment at 300°C (DA300) did not reach the same level of flexural strength. In compared to the untreated specimens, they showed a slight improvement in flexural strength of about

6%, giving them an average flexural strength of 131.77 MPa and a standard deviation of 3.30 MPa.

On the other hand, the specimens heated to 200°C showed a decline in mechanical qualities. Particularly, the characteristics of the specimens that underwent oven treatment at 200°C decreased by 6.5%, yielding an average flexural strength of 116.2 MPa and a standard deviation of 19.41 MPa. A 5% drop in characteristics was also seen in the directly treated specimens at 200°C, with an average flexural strength of 118.3 MPa. Results are shown in Figure 30.

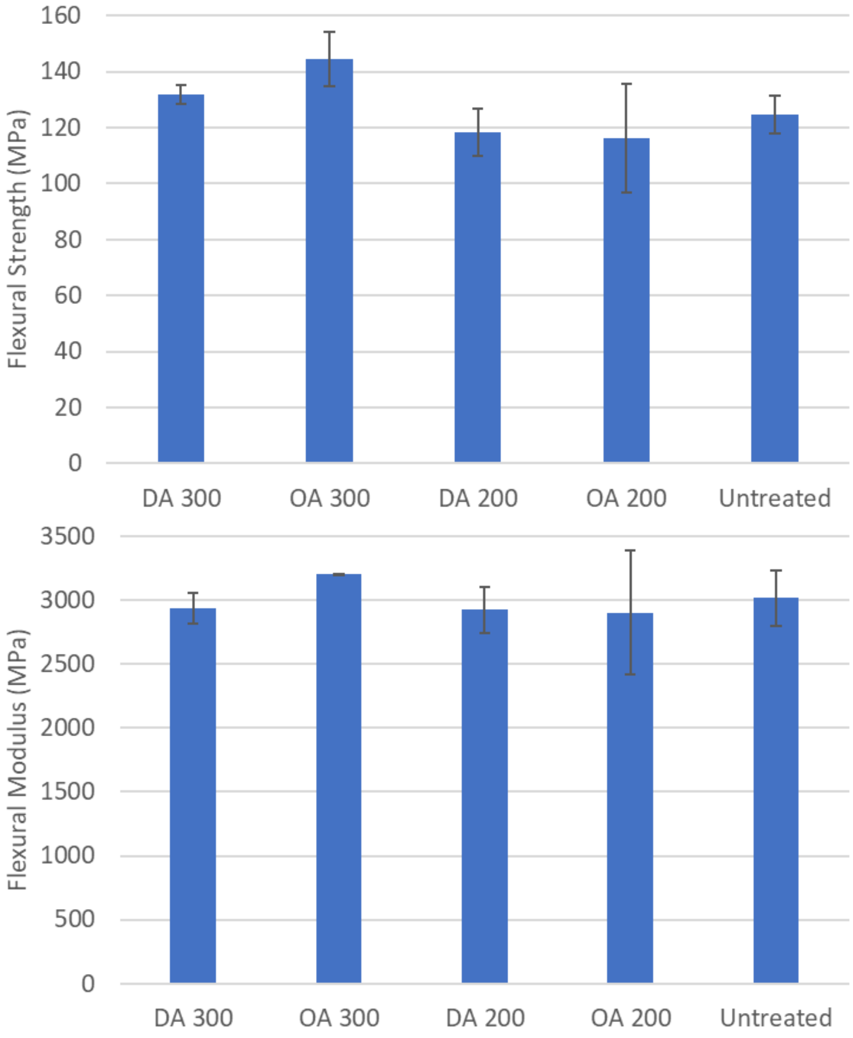

Figure 30. Flexural strength test avg results plot

Statistical analysis

To determine how treatment and treatment temperature affected the mechanical properties, statistical analysis was done. Studies [72] and [76] from the analyzed literature have shown a particular interest in running annealing cycles at 200°C and 300°C. Analysis was done on the data pertaining to the Flexural Strength of the 12 specimens, which were heat treated and received from earlier mechanical tests.

Only the treatment's temperature showed a significant influence in the ANOVA analysis with a 95% confidence interval (p-value 0.016). The main effects plot (Figure 31) supports this conclusion and shows that the type of treatment had a negligible effect on flexural strength. In contrast, it was discovered that the treatment's temperature had a considerable impact, in line with patterns reported in earlier literature [72], [74], and [81].

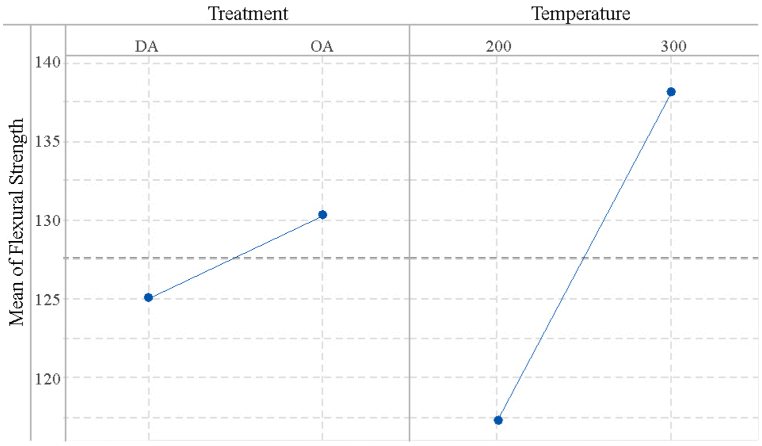

Figure 31. Main effects plot for flexural strength.

SEM analysis

The annealing-induced changes to the material structure were examined using a scanning electron microscope (SEM), as shown on Figure 32. The bonding between layers improved during direct and oven annealing at 300°C, confirming the results of the mechanical testing and verifying previous research. The behavior of the bending test specimens examined in this investigation was consistent, highlighting the main issue of layer separation brought on by the forces exerted during the bending test. Areas of layer discontinuity between specimens with lower flexural strength were visible as delaminations and voids. For reference, Figure 32 shows the untreated (UNT) specimen before mechanical testing; the printing process had reduced the adhesion between its layers. Following mechanical testing, cross-sectional photographs of specimens treated directly and in an oven are shown in Figure 32.

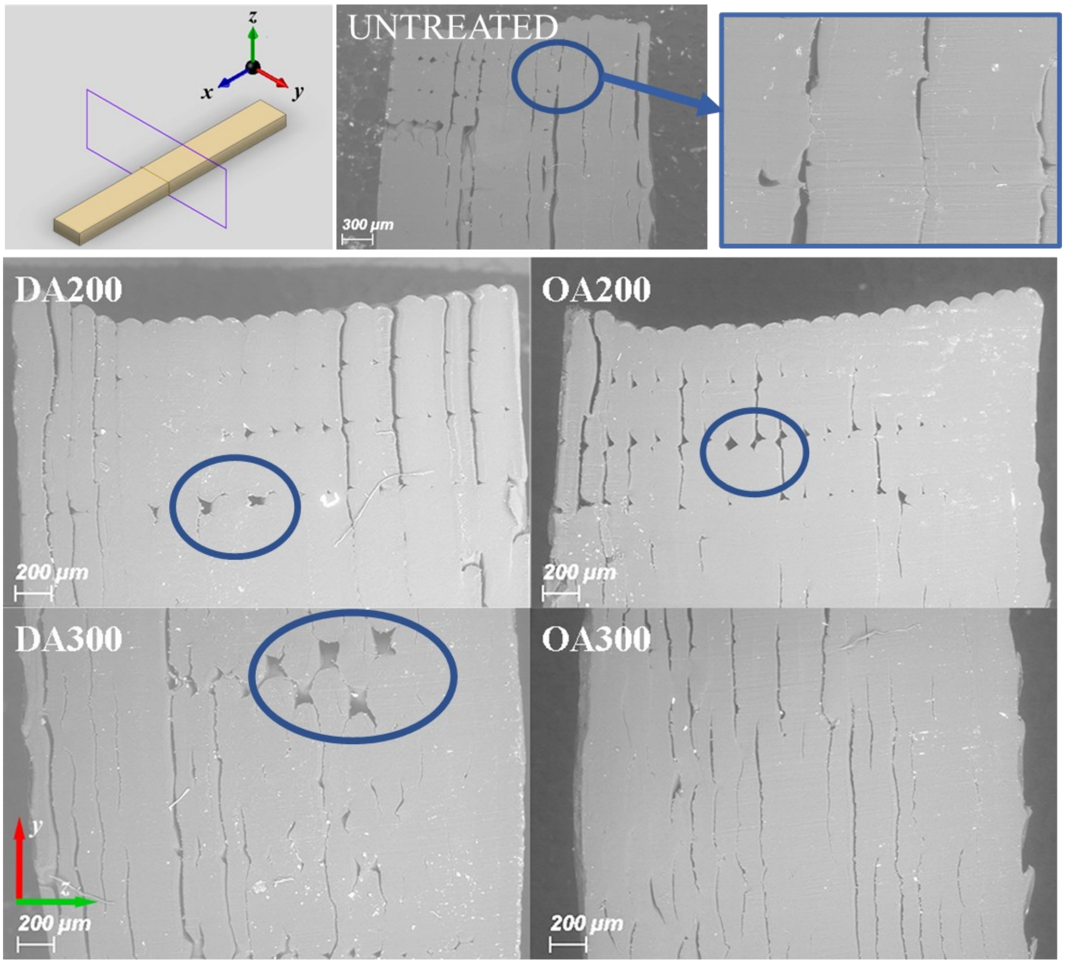

Figure 32. Scheme of printing orientation with highlighted cross-section and SEM images of specimen cross-sections after flexural tests.

Since DA200 was very similar to the UNT specimen, it is possible that the treatment had little to no impact and, in the case studied, reduced flexural strength. It can be concluded that gaps between layers, which are increased by bending, are the main cause of the decline in bending properties. The results of the mechanical tests, which demonstrated increased flexural characteristics, were consistent with the findings of the treatment at 300°C, as the specimens showed greater compactness. Less space existed between the layers in these samples. While certain holes in the DA300 material affected the test results, the most compact material, OA300, produced the best flexural strength results while exhibiting less deformation before failure. Notably, compared to DA300 and OA300, the disparities in DA200 and OA200 were larger and deeper.

3.3 Conclusions

This chapter compares oven annealing to direct annealing and analyzes the mechanical characterization of PEEK under the impact of direct annealing. The data showed that the direct and oven treatment methods had little effect on flexural strength, with temperature being the main determining factor. According to the analysis, the best therapy took place at 300°C. For both oven annealing and direct annealing, the flexural strength showed a noticeable improvement of 16% and 6%, respectively. In comparison to direct annealing, the oven treatment at 300°C increased mechanical performance by 10% but required manufacturing processes (printing and oven annealing) that were almost 3.5 times longer. When production time was merely the time it took to print a product, direct annealing (DA300) became the more cost-effective option. In general, the direct annealing system's adoption resulted in benefits for the PEEK printing process. When compared to untreated components, direct annealing at 300°C significantly increased printing quality, better bonding adhesion, and flexural strength with a minor cost increase related to variations in electrical consumption.

Chapter 4

THERMO-PHYSICAL CHARACTERIZATION OF CARBON FIBER REINFORCED POLYMERS

When MEX is combined with composites, it produces strong, lightweight, useful pieces with unique features. The thermal, rheological, and mechanical characteristics of Onyx, a high-performance nylon-based material reinforced with chopped carbon fiber, are examined in this chapter. The study examines the material's flow behavior and thermal properties using rotational rheometry and differential scanning calorimetry, respectively. Tensile and flexural tests are also used in the study to assess the material's mechanical characteristics under various loading scenarios and infill patterns. The findings demonstrate that the kind and approach of the infill design have a significant impact on the mechanical properties of onyx. This study offers a thorough grasp of the characteristics of the onyx material, which will aid in enhancing its performance in a variety of applications.

4.1 Materials and methods

Due to its superior mechanical qualities, Onyx (Markforged Inc., USA), a proprietary material with a 1.75mm filament diameter, was chosen. Onyx was a nylon-based substance that contained chopped carbon microfibre at a notional density of 1.2 g/cm^3. The length of the chopped fiber varies widely within the micrometer (168 ± 37 μm). For items with a premium surface finish and high heat tolerance, it gave exceptional strength, toughness, and chemical resistance. The provider claimed an Ultimate Tensile Strength (UTS) of 70MPa when printed with 100% filler, according to its technical datasheet [102].

HAAKE Mars III rheometer (Thermo Fisher Scientific Inc., MA, USA) with parallel-plate geometry and a plate diameter of 20 mm was used to examine the material's viscosity at the printing temperature as well as its thermal properties. To confirm rheological behavior in the linear viscoelastic area, frequency sweep tests were carried out with a strain amplitude of 1.0% while altering frequencies from 0.1 to 100 s^{-1}. As a precaution against heat degradation, the rheological characteristics of the Onyx were assessed at various temperatures, ranging from 230 to 270 °C, beginning 120 seconds after the sample was inserted between the plates. Five tests lasting three minutes each were conducted on all the measurements in the air to ensure repeatability. The morphology of Onyx was stable during these experimental settings, as shown by measurements taken both before and after. At the investigated temperature of 275°C, the time-temperature superposition (TTS) principle shifted frequency data into a single master curve.

The samples were created by Mark Two (Markforged Inc., USA)[100]. The spool was a highly hygroscopic material, so it was kept in a dry box to prevent moisture absorption. The primary characteristics of this desktop series printer, based on FFF and CFR technology, were a fully enclosed build volume of 320 × 132 × 154 mm^3 and the presence of two extrusion nozzle, one intended for FFF printing and one for CFR printing. On the other hand, there were some important drawbacks with this printer, such as the fact that the printing speed and nozzle temperature were fixed and could not be altered. Heating of the build platform was not possible. The printer also made use of the exclusive, user-friendly slicer Eiger^{TM}. For this study, the slicer software's fixed parameters were:

- The diameter of the FFF nozzle was 0.4 mm.

- The layer height was 0.125 mm.

- The number of wall layers was equal to 2.

- The number of top/bottom layers was equal to 2.

- The infill percentage was greater than 60%.

The decision to establish the infill percentage was made with the knowledge that infill density frequently influences the part's strength. Standard 3D components were created with an infill percentage ranging from 15% to 50% and were intended for mild duty and low strength applications. The goal was to give some strength by strengthening the part's structure within this infill density range without significantly affecting the part's weight or print time. A higher infill density, often greater than 50%, was required for functional sections designed to bear greater pressures and loads to minimize pressure-related ruptures. Although choosing a 100% infill density had the disadvantage of taking longer to fabricate the part and using more material, it produced the best performance. On the other side, lower infill percentages meant less material was used, which decreased the part's overall cost.

According to UNI EN ISO 178 [143], prismatic samples measuring 80 mm x 10 mm x 3 were utilized for flexural tests. Following UNI EN ISO 527 [145], tensile tests were performed on type 1B specimens. Measurements are shown in Figure 33.

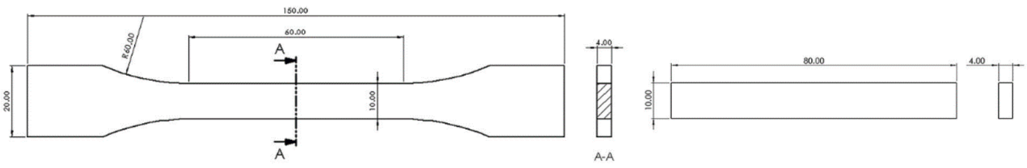

Figure 33. Tensile specimen (left) and flexural specimens (right) (all dimension in mm).

All specimens received inspection using visual and contact techniques before mechanical testing to evaluate their dimensional quality. The RH-2000 (Hirox Europe, Limonest, France) digital microscope, with a 1,920 by 1,200 pixel CMOS camera, collected images at a rate of 50 frames per second, making it easier to quantify deposited lines and assess the samples' quality of inner structure. In addition, the specimens' macro geometry was measured using a Coordinate Measurement Machine (CMM) DeMeet 400 (Schut Geometrische Meettechniek bv, The Netherlands), outfitted with a typical Renishaw TP20 system and a 2mm diameter stylus. To ensure a maximum temperature fluctuation of 0.5 °C from the ambient temperature, all measurements were done in a temperature-controlled setting. An eSun 10 universal testing device (Galdabini, Italy) with a 100 kN load cell was used to conduct the mechanical tests.

The effect of particular characteristics on the mechanical behavior of specimens was investigated using a mixed Design of Experiment (DoE). The printing orientation, which had two levels: XY (flat) and XZ (on-edge), and the infill pattern, which had four levels: gyroid, hexagonal, rectangular, and triangular, were among the elements considered. For the tensile tests, 24 specimens and the flexural tests, 24, each of these combinations was repeated three times (Figure 34). The samples were subjected to a variety of evaluations, including weight measurements and dimensional accuracy tests, which were first carried out using a caliper and then with a Coordinate Measuring Machine (CMM). Based on the actual weight and plastic volume, the infill density for both the tensile (Table 14) and flexural (

Table 15) samples was calculated. The Eiger slicer computed the plastic volume, which represents the amount of material utilized to build the specimen. It is interesting that the various filling cell choices made for the testing led to variances in sample weight and plastic consumption. These variations were also seen in the mechanical tests, where some infill designs displayed higher mechanical properties while using less material. Notably, different filling cells required different amounts of material, leading to these differences, even at the same infill density. Variations in the top and bottom layers' extensions were connected to the weight discrepancies that were attributed to the printing orientation. Analysis of fully dense flexural samples, where the weight difference was 0.44 grams, made this phenomenon particularly clear.

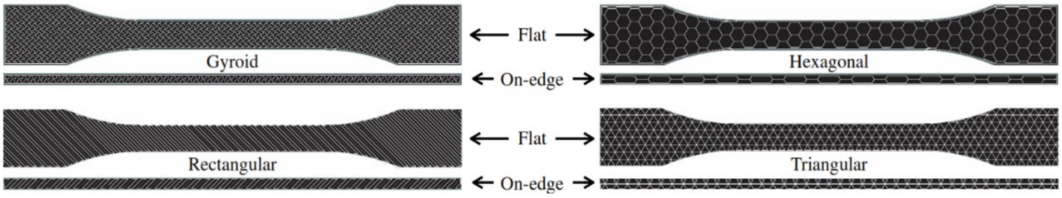

Figure 34. Detail of printing orientation and infill strategies.

Table 14. Tensile specimens

Specimen ID	Build	Plastic volume	Weight	Infill density
Full XY	flat	8.27	9.92	100.00
Full XZ	on-edge	8.81	10.57	100.00
Gyroid XY	flat	5.37	6.44	64.93
Gyroid XZ	on-edge	5.68	6.82	64.47
Hexagonal XY	flat	5.43	6.52	65.56
Hexagonal XZ	on-edge	5.56	6.67	63.11
Rectangular XY	flat	5.38	6.46	65.06
Rectangular XZ	on-edge	5.52	6.62	62.66
Triangular XY	flat	5.32	6.38	64.33
Triangular XZ	on-edge	5.54	6.65	62.88

Table 15. Flexural specimens.

Specimen ID	Build	Plastic volume	Weight	Infill density
Full XY	flat	3.22	3.86	100.00
Full XZ	on-edge	4.10	3.42	100.00
Gyroid XY	flat	2.07	2.48	64.29
Gyroid XZ	on-edge	2.19	2.58	62.87
Hexagonal XY	flat	2.03	2.44	63.04
Hexagonal XZ	on-edge	2.19	2.63	64.04
Rectangular XY	flat	2.09	2.51	64.91
Rectangular XZ	on-edge	2.17	2.60	63.45
Triangular XY	flat	2.09	2.51	64.91
Triangular XZ	on-edge	2.09	2.51	61.11

DSC and rheological analysis

Numerous processing factors, such as humidity, temperature, shear rates, and processing time, had a substantial impact on the characteristics of onyx. Both DSC analysis and rheometry were used to assess the Onyx material's thermal and flow properties during the MEX process. To prevent material decomposition at elevated temperatures, the maximum temperature for the DSC analysis was maintained at 320 °C, and the cycle was repeated twice. The degree of crystallinity (X_c) was subsequently determined through the following formula:

$$X_c = \frac{\Delta H_m - \Delta H_{cc}}{\Delta H_{m0}} \tag{1}$$

where ΔH_m is the melting enthalpy at the melting temperature T_m, ΔH_{cc} is the cold crystallization enthalpy, and ΔH_{m0} is the melting enthalpy for a complete crystalline material at the reference temperature T_{m0}. This final value of enthalpy was equal to 196 J·g^{-1}. The filament's DSC thermograms are shown in Figure 35. The melting temperature T_m was 201.5 °C, while the glass transition temperature T_g was 100.2 °C. A 48% crystallinity and a melting enthalpy of 38.57 J·g^{-1} were recorded. There was no sign of cold crystallization. Crystallization temperature T_c was 160.3 °C.

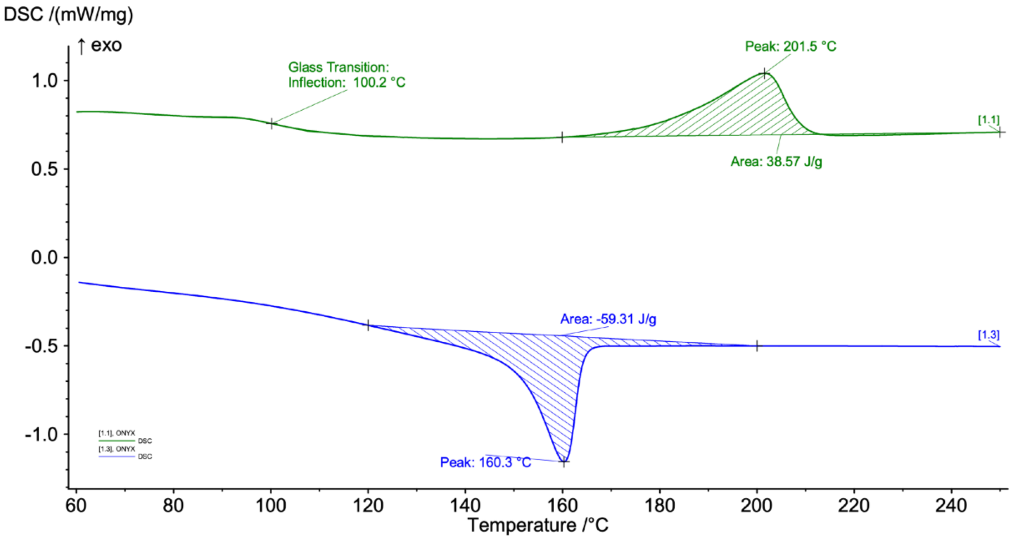

Figure 35. DSC thermograms (heat flux vs temperature).

According to the DSC test results, the thermal behavior of Onyx had an impact on the deposition and, consequently, the performance of the finished component in the dynamic MEX scenario. The material maintained its thermal stability for the two successive runs and was deemed to be fully melted at the 275 °C extrusion temperature. There were no detectable changes in the primary thermal properties.

The purpose of the rheological characterization was to gather pertinent data for assessing the MEX procedure. The melt extrusion through the nozzle and the subsequent welding of the deposited layers were both influenced by the polymer's viscoelastic nature. From 230 to 290 °C, viscoelastic parameters including storage modulus G', loss modulus G'', and apparent viscosity η^* were determined (Figure 36). The substance appeared to follow the linear viscoelasticity predictions, with G' and G'' being proportional to ω^2 and ω^1, respectively, at low ω. Over the testing frequency and temperature ranges, the material displayed nearly linear Newtonian melt behavior, typical of a PA6. Particularly at high shear rates, the temperature had a significant impact on the rheological properties. The apparent viscosity η^* significantly but steadily decreased over the investigated frequency range. The stiff carbon fibers in the nylon matrix most likely helped the polymer chain entanglements to become disorganized under shear force, which led to the severe shear thinning behavior. The master curve was then calculated at the reference temperature of 275 °C after these curves had been fitted (see Figure 37). It was possible to locate the intersection of G' and G'' for an angular frequency of 628 rad/s.

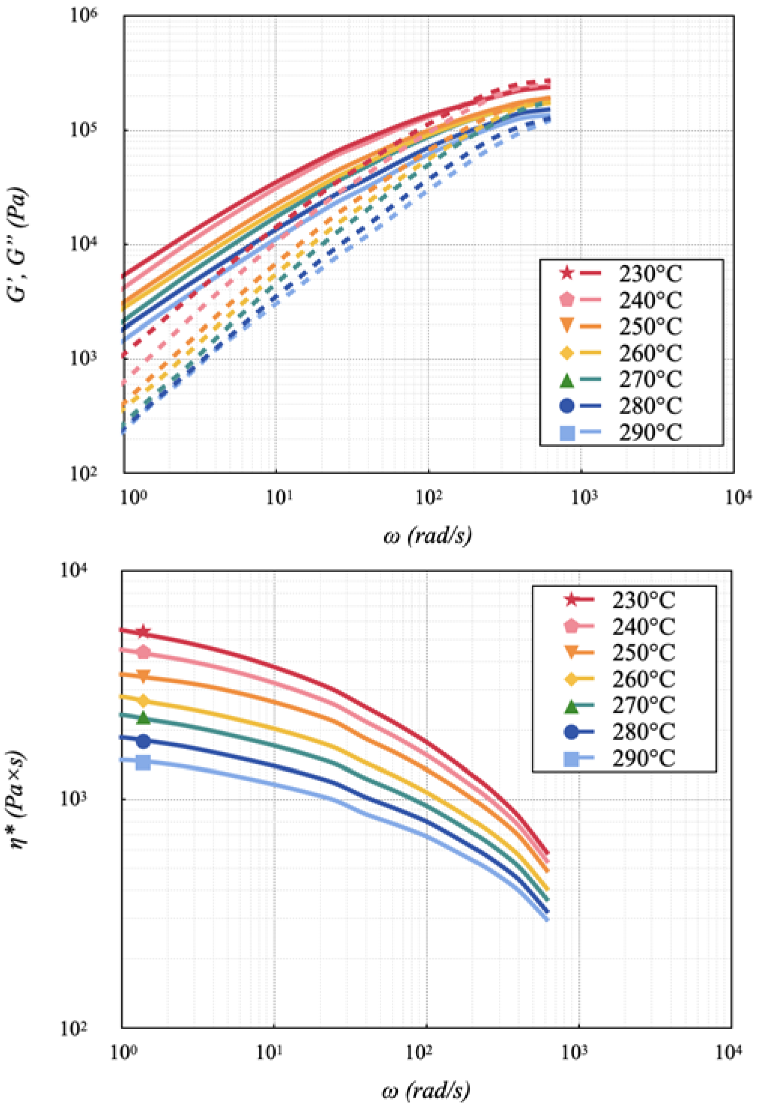

Figure 36. Storage G', loss G'' moduli and apparent viscosity η^*.

In order to cover a frequency range more significant than the narrow range of the single sweep tests, the other individual frequency data sets at various temperatures were shifted horizontally and vertically in the direction of the reference temperature. This was especially true for higher angular frequencies. The extrusion shear rate with a printing speed of 25 mm/s was 200 s^{-1}. Onyx had a viscosity of 750 Pa × s at the printing temperature of 275°C, which was higher than that of PLA, which had a viscosity of 200 Pa × s. This value of shear rate was lower than that of ABS, which had a viscosity of 1,000 Pa × s.

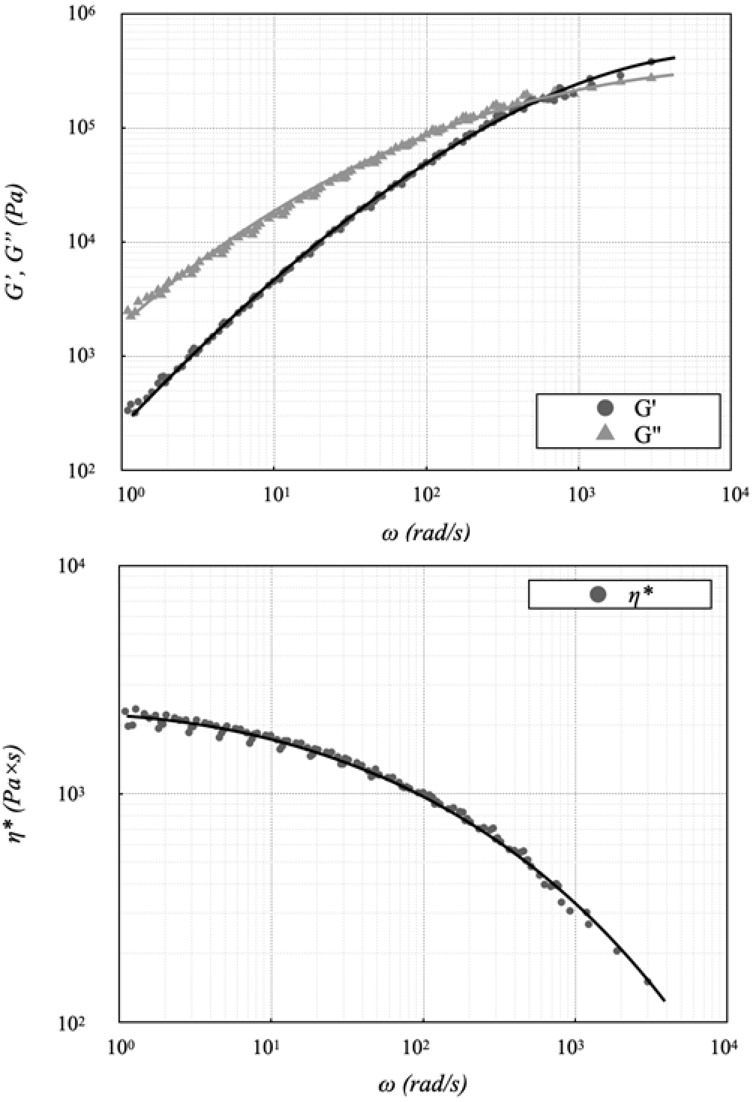

Figure 37. Master curves at 275°C computed with TTS.

Dimensional analysis

$40 \times 4 \times 15$ mm^3 prismatic specimens were produced in the same batch on the machine platform to guarantee dimensional stability. The samples were measured using a caliper to nearly match the dimensions after waiting for eight hours to reach the conditioned state. A more accurate measurement was made using a CMM after confirming the lack of printing errors and an error of less than 2% on all primary dimensions. Using the average of five replicates, the total volume of a printed sample was determined based on its real geometry. The dimensions and geometry of these pieces frequently had systematic flaws. To create the physical portion, the perimeters were repeatedly filled with layers of a specific thickness. The surface polish was subpar since the entire thing was built up layer by layer and the part surfaces were approximated into two-dimensional planer sections and layers. Volumetric error $V_{\%}$, calculated as the difference between the volumes of the deposited component V_p and the digital model V_d, was a volume deviation in MEX parts.

$$V_{\%} = \frac{V_p - V_d}{V_d} \times 100 \tag{2}$$

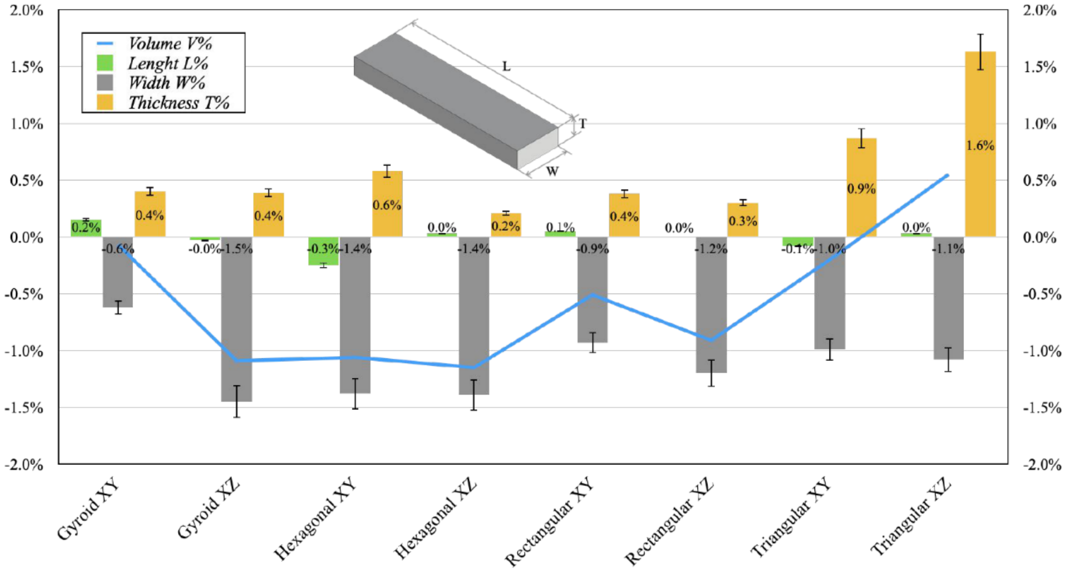

Figure 38. Dimensional analysis.

Figure 38 presents a curve for the results of the $V_{\%}$ of the printed specimens. The length L, width W, and thickness T deviations are shown by the bars in the same graph. According to the findings, dimensional accuracy was quite high, falling between +0.5% and -1.5% for $V_{\%}$ and below 2% for each dimension. The on-edge hexagonal infill was the least precise instance, and the flat gyroid infill was the most correct. The breadth dimension's large inaccuracy was unrelated to the build orientation. To evaluate the accuracy of the sample patterns, dimensional analyses were expanded. The 2D schemes for the various infill patterns are shown in Figure 39, along with the kinds of lines that were calculated using a digital microscope. The line thickness represented by the deposited line was between 80-120% of the nozzle diameter. When the FFF nozzle's diameter, depicted in Figure 40, was measured, an average of five measurements yielded a value of 430 ± 3.5 μm. Individual lines (shown in green) were used to build the infill, while two adiacent lines were used to create the perimeter walls (shown in red).

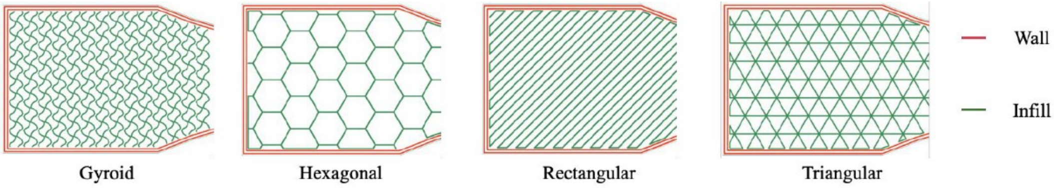

Figure 39. Designation of the wall and infill lines for the various infill patterns.

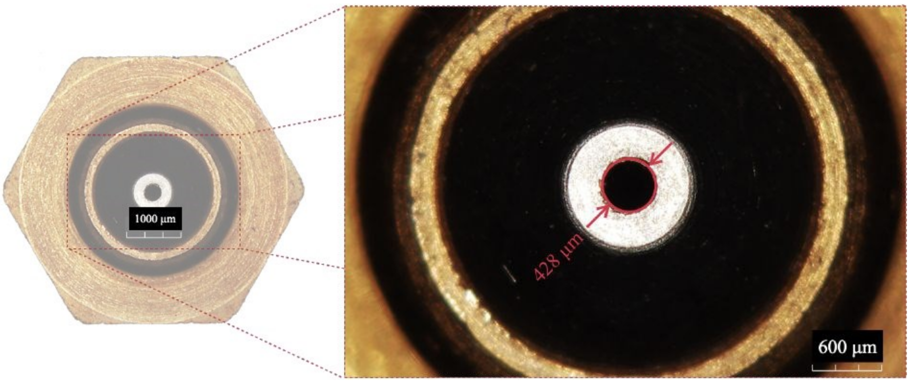

Figure 40. Diameter of FFF nozzle.

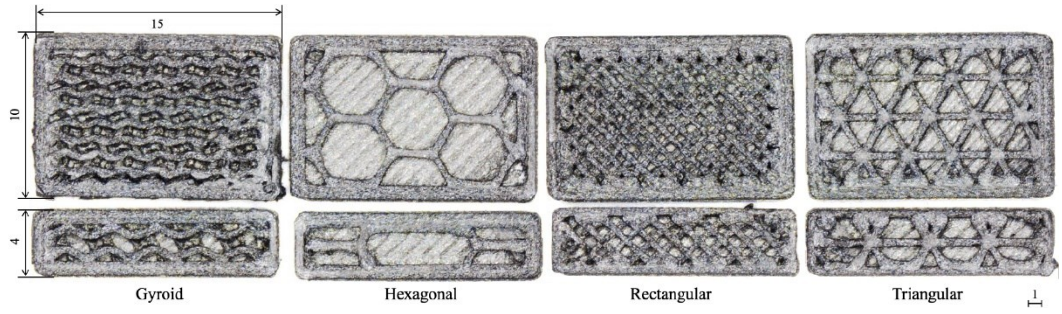

Figure 41. Dimensional analysis of the infill patterns (all dimensions in mm).

The flat specimen's filling patterns were all controlled, resulting in good dimensional precision in the perimeter and inner structure (Figure 41). With a maximum value of less than 8%, the deposition line width variation was hardly noticeable for any infill pattern. The largest value of the angle variation was 0.5%, which is extremely low. Due to the smaller section on the *XY* plane, the situation for the specimens that were on edges changed. Due to internal flow rate modifications made by the slicer, all infills had flattened cell shapes and thinner perimeters. Gyroid patterns were least affected, whereas hexagonal patterns were most deformed.

Investigations were also conducted on the material's chopped carbon fiber. The configuration of the chopped fiber in the filament prior to deposition is shown in Figure 42-a. The fibers had a non-uniform distribution in the polymer phase and were oriented in the extrusion direction parallel to the filament axis. They had a diameter of 8.70 ± 0.13 μm and a length of 168 ± 37 μm. Some regions had a high concentration of fibers, whereas others just showed the polymer matrix. This inhomogeneous distribution across the cross-section contributed to the disparity in local fiber volume fraction. After deposition, minor modifications were found, as shown in Figure 42-b. The air gaps between the deposition lines in a deposited layer were represented by the black spaces. Most of the fibers were pointed in the direction of movement (red arrow). The deposition line had a 0.408 mm thickness and an irregular distribution of fibers, with polymer-rich parts alternating with high fiber density regions.

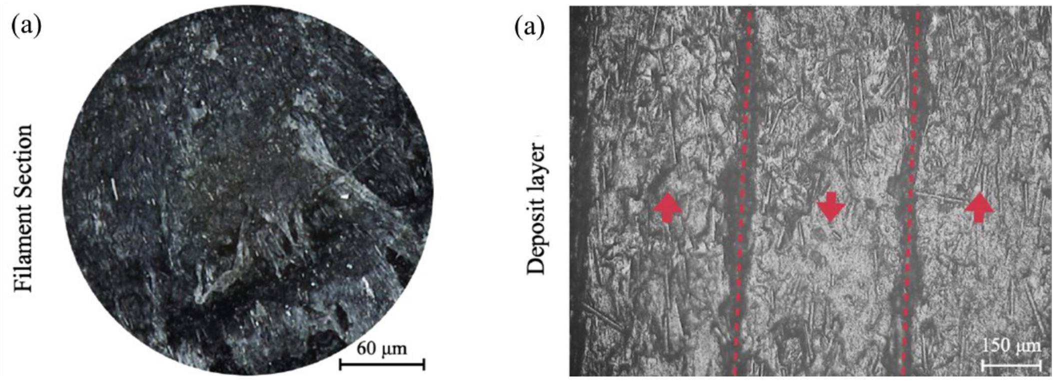

Figure 42. (a) Filament section and (b) specimen section observed with an optical microscope.

Time and cost analysis

The trade-off with mechanical attributes was examined using a cost and production time analysis. The ultimate cost of the printed sample was calculated using a straightforward cost evaluation approach. The whole cost included expenses for labor, materials, operations, and electricity. The price of materials was specified as

$$Material\ Cost = M \times p = \rho \times \pi \times (d/2)^2 \times L \times p \tag{3}$$

where M was the part mass, p was the filament cost per kilogram, ρ the material density and d and L were the filament diameter and deposited length. The labor cost was defined as

$$Labor\ Cost = t_{design} \times hlr \tag{4}$$

where t_{design} was the time to orient the part, set up printing parameters and slicing, and hlr was the hourly labor rate. The operation cost was defined as

$$Operation\ Cost = t_{printing} \times hoc \tag{5}$$

where $t_{printing}$ was the time needed to realize the part, and hoc was the hourly operation charge. The electricity cost was

$$Operation\ Cost = t_{printing} \times Pow \times lec \tag{6}$$

where *Pow* was the rated power of the MEX printer, and *lec* the local electricity cost. Table 16 reports the cost adopted.

Table 16. Cost specifications.

Cost	Abbreviation	Value	Unit
Material price	*P*	287.5	USD/kg
Hourly labor rate	*hlr*	30	USD/h
Hourly operation charge	*Hoc*	1	USD/h
Local electricity cost	*lec*	0.15	USD/kW

The rectangular infill required a minimum printing time of 52 minutes, and the gyroid infill required a maximum printing time of 67 minutes for the tensile specimens printed along the XY plane. The cost variation was minimal because the weight was very similar, varying between the triangular specimen's minimum (7.7 USD) and the gyroid's maximum (8.0 USD). For samples printed along the XZ plane, the minimum printing time for the triangular was 75 minutes, and the maximum printing time for the gyroid was 92 minutes. Furthermore, the cost variance in this example was minor, with varied times being greater than the printing costs, regardless of specimen printing orientation. The totally dense data between the rectangular minimum (8.2 USD) and the gyroid maximum (8.5 USD). The graph also showed the difference in printing specimens, with the flat specimen taking 72 minutes and 9.1 USD and the on-edge sample taking 111 minutes and 9.9 USD. All data are depicted in Figure 43-left. Flexural specimens followed the same pattern as tensile specimens, with an average cost reduction of roughly 10% for practically all configurations to fully dense specimens. The flat specimen took 25 minutes to print and cost 6.13 USD, whereas the on-edge specimen took 30 minutes and cost 6.26 USD. All data are depicted in Figure 43-right.

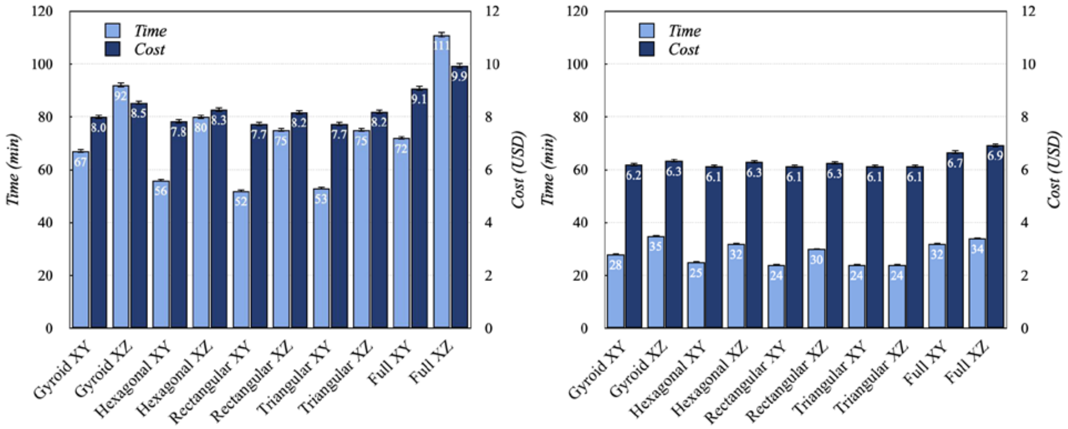

Figure 43. Time and cost analysis graph of tensile (left) and flexural (right) specimens.

4.2 Experimental results and discussion

Tensile tests

Tensile testing was performed in two steps in accordance with UNI EN ISO 527 [145]. To determine Young's modulus and yield point, a strain gauge was used in a first phase that was performed at a slower speed (1 mm/min). A second phase, which was completed at a faster speed (5 mm/min), was used to test the material until failure. The specimen and the extensometer mounting are shown in Figure 44. Extensometers measured strain on the specimen directly, removing measurement influences from other testing components and boosting accuracy. This data was required to compare the effect of the infill scheme. The summary of tensile modulus E, yield strength σ_Y, and Ultimate Tensile Strength UTS is reported in Table 4.

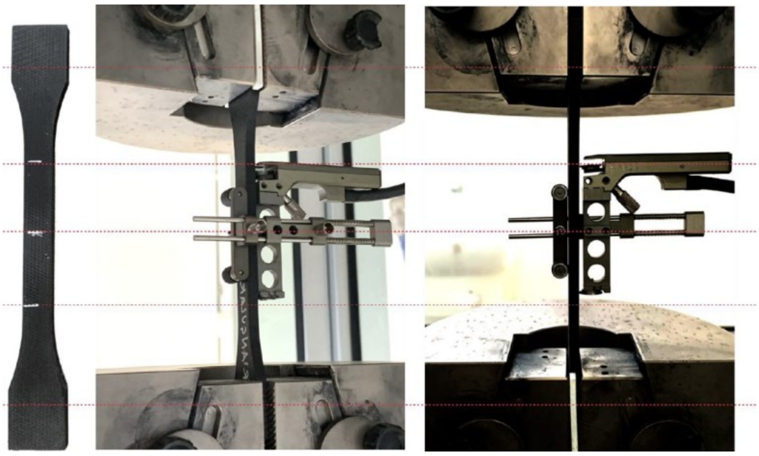

Figure 44. Specimen mounted on the tensile test machine with the longitudinal extensometer.

Table 17. Tensile tests data.

Specimen ID	Build	Tensile modulus *E*	Yield	UTS
Gyroid XY	flat	871	18.29	51.30
Gyroid XZ	on-edge	1,944	22.91	65.86
Hexagonal XY	flat	1,015	10.66	26.20
Hexagonal XZ	on-edge	2,101	18.38	29.51
Rectangular XY	flat	961	11.53	28.19
Rectangular XZ	on-edge	1,835	21.58	47.87
Triangular XY	flat	901	12,61	26.16
Triangular XZ	on-edge	1,660	26.13	45.93

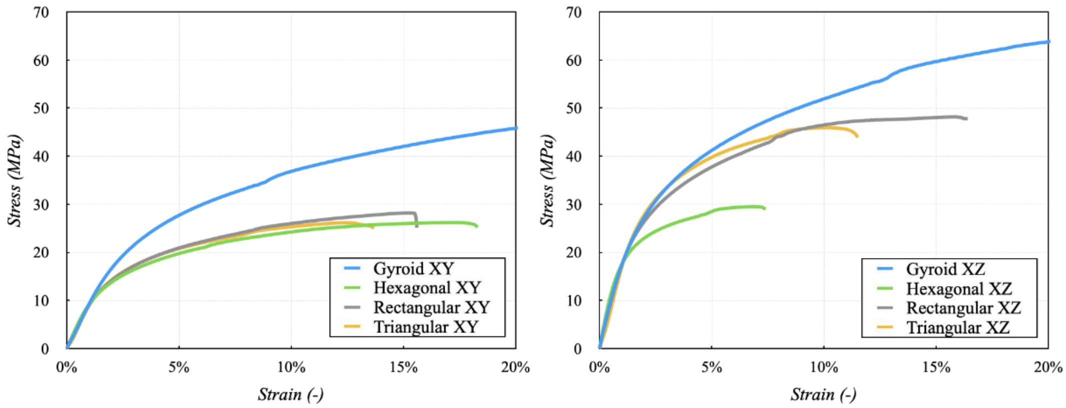

Figure 45. Tensile test results for (left) flat and (right) on-edge specimens.

In comparison, the tensile test curves of flat and on-edge specimens at a maximum strain of 20% are shown in Figure 45. A preliminary examination revealed that the strength of on-edge specimens was greater than that of flat specimens with the identical infill patterns, validating the analyzed literature. Tensile specimens with the gyroid infill outperformed other infill patterns in terms of yield σ_Y and ultimate tensile strengths *UTS* in both orientations. This behavior may be explained by the intricate gyroid infill pattern and interconnecting spiral forms that provide strength and support in all directions. As a result, the printed product was less prone to warping and could withstand larger loads without rupturing. The hexagonal infill, on the other hand, had the lowest performance. The rectangular and triangular infills were nearly identical, yielding intermediate outcomes. Young modulus *E* showed a similar trend in the *XY* printing orientation, varying between 871 MPa (gyroid) and 1,015 MPa (hexagonal). In the *XZ* printing orientation, young modulus values doubled, ranging from 1,660 MPa (triangular) to 2,100 MPa (hexagonal). The tensile characteristics of the different printing orientations varied due to two types of failures: layer separation and slippage and single-layer breakage. During the test, the specimens printed along the *XY* and *XZ* directions have a build direction parallel to the load. All experimental modulus and strength values were 50% lower than samples with 100% infill. The data's Analysis of Variance (ANOVA) demonstrated that printing orientation and infill patterns were both influential, with p-values less than 0.05. The plots of the main effects and interactions for the analyzed response variables *E*, *Y*, and *UTS* are shown in Fig. 14. The measured value was represented by a design point, while the predicted point was determined by the ANOVA model. The coefficient of determination R^2 was greater than 98%, indicating that measurements and forecasts were in excellent agreement. By printing the sample in the *XZ* direction with the gyroid infill pattern, optimal results could be obtained for two of each response variable.

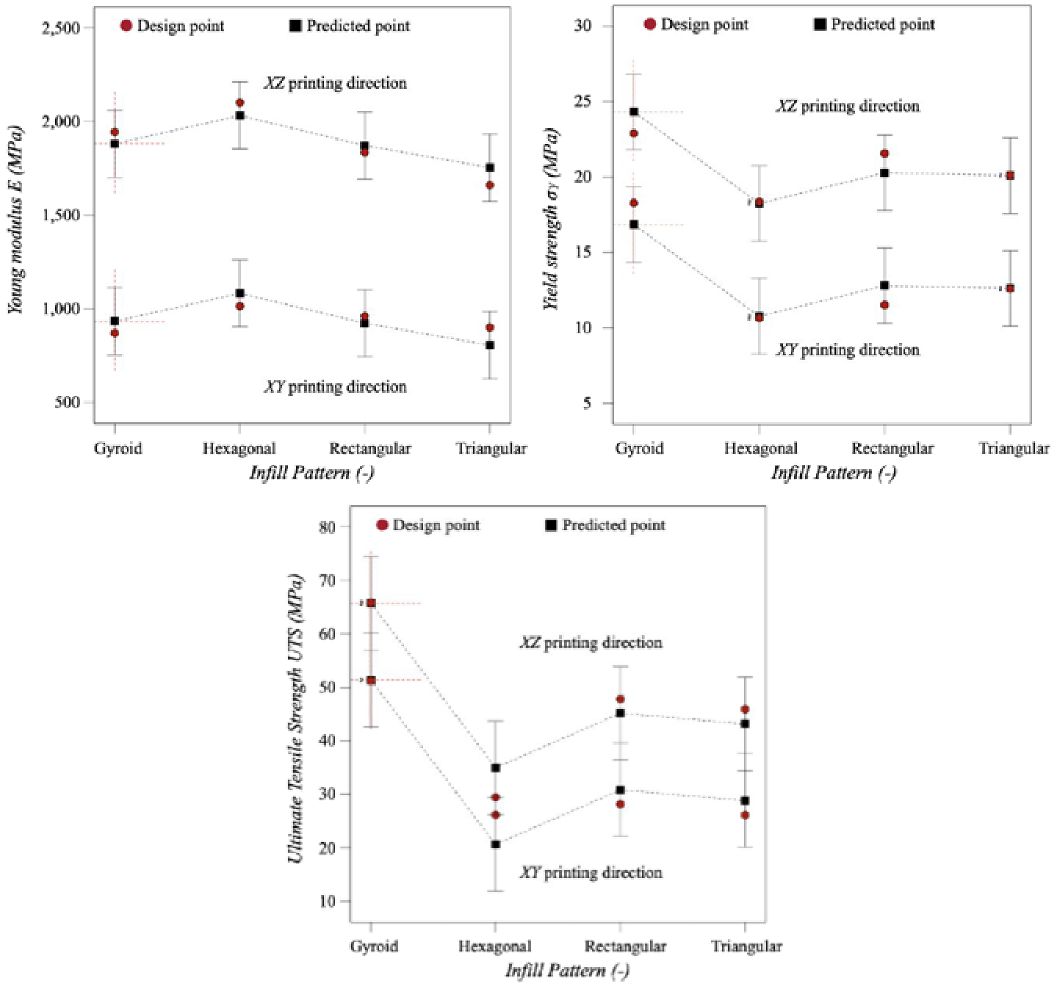

Figure 46. Main effect and interaction plots of Young modulus (left-up), yield strength (right-up), and ultimate tensile strength (center-down).

Flexural tests

The flexural tests (Figure 47) were performed in accordance with UNI EN ISO 178 [143]. The specimen had dimensions of 80 × 10 × 4 mm^3 and was mounted with a span L between supports of 60 mm. Flexural strain and stress were :

$$\varepsilon_f = \frac{6 \times s \times h}{L^2} \tag{7}$$

$$\sigma_f = \frac{3 \times F \times L}{2 \times b \times h^2} \tag{8}$$

where s is deflection, h is thickness, and F is applied force. The flexural modulus E_f was computed using a linear regression applied to the stress-strain curve between the two flexural couples (ε_{f1}, σ_{f1}) and (ε_{f2}, σ_{f2}) with $\varepsilon_{f1} = 5\times10^{-3}$ and $\varepsilon_{f2} = 25\times10^{-3}$.

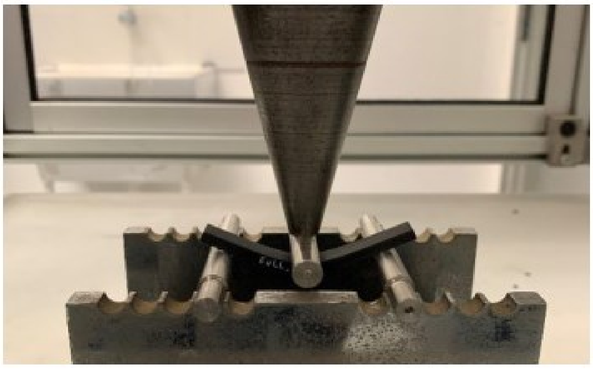

Figure 47. Flexural test

Table 18 summarizes the flexural modulus E_f and flexural strength σ_f. In comparison, the curves of the flexural testing of flat and on-edge specimens at a maximum strain of 12% are shown in Figure 48.

Table 18. Flexural tests data.

Specimen ID	Build	Flexural modulus E_f	Flexural stress σ_f
Gyroid XY	flat	1,128	37.84
Gyroid XZ	on-edge	1,774	47.23
Hexagonal	flat	941	29.81
Hexagonal	on-edge	1,754	37.08
Rectangular	flat	938	27.23
Rectangular	on-edge	1,367	34.66
Triangular	flat	873	27.47
Triangular	on-edge	1,188	30.36

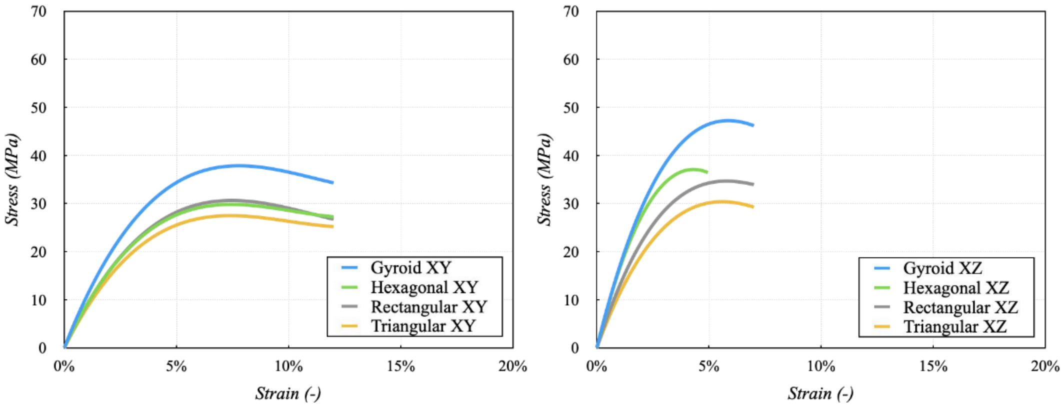

Figure 48. Flexural test results for (left) flat and (right) on-edge specimens.

A preliminary investigation revealed that the strength of on-edge specimens was larger than that of flat specimens with the identical infill patterns, corroborating the results of tensile tests. For both orientations, the flexural strength σ_f of specimens with gyroid infill was greater than that of other infill techniques. This response validated the effectiveness of the complicated gyroid infill pattern and interconnecting spiral forms, which provide strength and support in all directions. The triangular infill, on the other hand, had the lowest performance. The hexagonal and rectangular infills were almost identical, yielding intermediate outcomes. Flexural modulus E_f varied between 873 MPa (triangular) and 1,128 MPa (gyroid) in the *XY* printing orientation. In the *XZ* printing orientation, modulus values ranged from 1,118 MPa (triangular) to 1,774 MPa (gyroid). All experimental modulus and strength values were 50% lower than samples with 100% infill. The above data's Analysis of Variance (ANOVA) demonstrated that printing orientation and infill patterns interact for the analyzed response variables E_f and σ_f. A design point reflected the measured value, whereas both were influential, with p-values less than 0.05. The plots of the major effects and the ANOVA model computed the anticipated point are shown in Figure 49. The coefficient of determination R^2 was greater than 98%, indicating that measurements and forecasts were in excellent agreement. It is possible to attain optimal results. Printing the sample in the *XZ* direction with the gyroid infill pattern produced the best results.

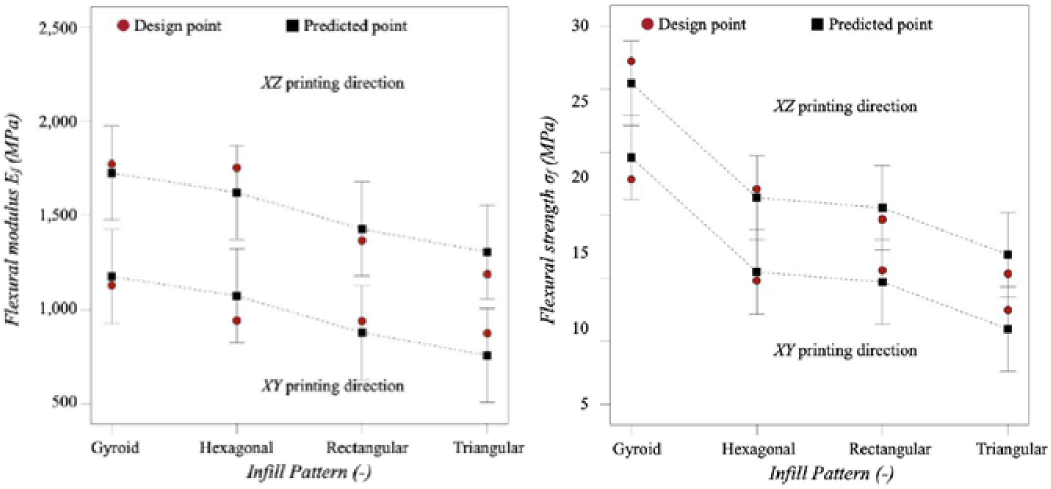

Figure 49. Main effect and interaction plots of (left) flexural modulus and (right) flexural strength.

4.3 Conclusions

The purpose of this investigation was to examine the tensile and flexural performance of Onyx specimens with various filling patterns and printing orientations, as well as the impact of these patterns on production time and cost. Tensile testing revealed that the gyroid-type infill had the highest tensile strength, both in the case of print orientation along the *XY* and *XZ* planes. The rectangular infill had a 1% lower tensile strength in the printing orientation along *XY* and an 11% lower tensile strength in the printing orientation along *XZ* than the gyroid infill. Flexural testing indicated no significant differences in flexural strength, indicating that the specimen with gyroid infill performed well in both orientations. The ones with triangular infill patterns performed the worst. Furthermore, printing durations and manufacturing prices were discovered to vary based on the infill pattern chosen, with gyroid infill being an ideal option to rectangular infill due to its lower printing costs, higher mechanical properties, and somewhat longer printing periods. The gyroid infill was superior to the others because it was symmetrical on all three axes, resulting in specimens that were 3% lighter than rectangular specimens on the *XY* plane and 14% lighter on the *XZ* plane. Overall, this research has improved our understanding of the performance of various filling patterns and printing orientations in Onyx printing, as well as provided significant insights into the trade-offs between mechanical qualities, cost, and time. The findings can be used to influence the selection of infill patterns and printing orientations for various applications, as well as to improve the Onyx printing production process.

Chapter 5

THERMO-PHYSICAL CHARACTERIZATION OF ZIRCONIA FEEDSTOCK

This chapter examines a novel approach to manufacture ceramic components with filament-based Material Extrusion additive manufacturing (MEX), along with debinding and sintering. A commercial ZrO_2 filament was selected and examined using IR spectroscopy, rheology, and thermo-gravimetry. To determine an effective printing and sintering strategy, the effects of the print parameters (layer thickness, flow rate multiplier, printing speed) and sintering cycle were examined. A typical flexural strength of 871 MPa with a Weibull modulus of 4.9, a Vickers hardness of 12.90 ± 0.3 GPa, a sintered density > 99% of the theoretical density, 20% linear sintering shrinkage, and a thermal conductivity of 3.62 W/mK are all displayed by optimized samples. To demonstrate, gyroids structures were printed.

5.1 Materials and methods

Feedstock materials

A 1.75 mm-diameter filament made of 3 mol% yttria-stabilized zirconia (3Y-TZP) was purchased from 3DCeram Sinto Tiwari GmbH in Germany. For low environmental impact and reduced hazard, only solutions using chemical and/or heat debinding with low toxicity were taken into consideration when using commercially available filaments. To ensure precise material feeding during printing, the diameter distribution of the filament was examined using a laser diameter gauge (DGK2015, Proton Products). The binder was characterized using Fourier transformed infrared spectroscopy (FT-IR, 4200 of Jasco Co (Tokyo, Japan)) in the ATR mode with a resolution of 4 cm^{-1}. Each sample underwent several FT-IR-ATR tests at random locations, and the average spectrum was calculated. To assist in defining appropriate thermal debinding and sintering strategies, thermogravimetric analysis (TGA) and differential scanning calorimetry (DSC) were carried out on the filament using the SDT Q600 from TA Instruments at a constant heating rate of 10 °C/min up to 1000 °C in pure Ar gas (Liquid Argon > 99.998%, O_2 1.5 ppm). Using a rotational rheometer (Thermo Scientific Haake Mars III) with parallel plate geometry, rheology properties of the material were assessed in its green condition. To mimic the rheological conditions during printing and produce adequate torque values, tests using plates with a diameter of 20 mm were used, and they were carried out at 180 °C under controlled shear rate settings between 1 and 300 s^{-1}. Five times each, all measurements were made in the open air. During the testing, there was no evidence of heat deterioration. Measurements taken before and after the experiment showed that the polymer suspension's morphology was stable. SEM, Vega3 LMH, Tescan, and optical microscopy were both used to examine the cross sections of the filament.

3D Printing, Debinding and Sintering

Printing was done on a Prusa i3 MK3s, particularly with the direct drive configuration that steadily feeds the brittle filament without breaking. To guarantee smooth extrusion, a nozzle diameter of 0.4 mm was chosen because it is more than ten times larger than the zirconia particle size that was the subject of this study. In addition, a nozzle made of hardened steel was employed to prevent abrasion. To find an acceptable process window, screening experiments were carried out. Therefore, during sample production, the following print parameters were held constant: nozzle temperature 180 °C, bed temperature 60 °C, fan cooling on at 25% from the fifth layer, strand width 0.4 mm, double contour, and 100% infill with alternating +/- 45° patterns; however, a full factorial DoE 3^3 (see Table 19, 3 repetitions per experiments) was used to examine the main and interaction effects of the layer thickness, printing speed, and flow rate multiplier.

Table 19. Full factorial design of experiments.

Factors	Unit	Levels		
Printing speed	mm/s	10	30	50
Layer thickness	mm	0.1	0.2	0.3
Flow rate multiplier	%	90	100	110

Selected printed samples were subjected to post-processing in the following order: solvent debinding, heat debinding, and pressureless sintering. These techniques were paired with the appropriate print parameters in an effort to build best-practice manufacturing strategies. Based on the findings of the TGA studies and internal testing, post-processing was developed. As a result, during solvent debinding, the components were submerged in a 40 °C, magnetically stirred acetone bath for 48 hours. After a 24-hour period, new acetone was used as the solvent. The parts were then left outside for 12 hours to allow any remaining acetone to evaporate. 8.6% of the overall weight was lost after solvent debinding. The leftover binder was thermally released in an air-muffled muffle furnace (Carbolite, model RHF 1200). The components were heated to 150 °C at a rate of 1.3 °C/min and dwelled for 1 hour. The pieces were then heated for 1 hour at a temperature range of 150 to 450 degrees Celsius. 5 °C/min of cooling was used to reach room temperature. 5.7% of the weight was lost due to thermal debinding. The parts were then sintered in air using a Nabertherm HT16/17 after being heated to 1000 °C at 4 °C/min and 1475 °C at 2 °C/min with a dwell time of 2 h.

Characterization

Using an analytical balance (Quintix 224-1S, Sartorius), the density of filament, green, and sintered parts was determined in accordance with the Archimedes technique (ISO 18754:2020[146]). Scanning electron microscopy (SEM, XL30FEG, FEI) microstructural investigations were carried out on mirror-polished and platinum-coated cross-sectioned sintered parts. The best-practice production technique for mechanical testing was used to create two populations of 30 disc samples with a thickness of 1.2 mm and a diameter of 14 mm. To account for sintering shrinkage, grinding, and polishing that were necessary during sample preparation, a 20% disc oversize was established during printing. Specifically, an Instron 5567 with a crosshead speed of 1 mm/s underwent biaxial flexural tests in accordance with ISO 6872:2015 [147]. Weibull statistics were used to examine the strength data, which allowed for the quantification of the characteristic strength—the strength at which 63.2% of the samples fracture—and the Weibull modulus, which measures the strength distribution. After gold coating, the fracture surfaces were studied by SEM (nanoSEM, FEI). The Vickers hardness (HV) of polished prismatic components manufactured utilizing best-practice manufacturing techniques was measured (Model FV700, Future Tech Corp, Tokyo, Japan) with a load of 98 N applied for 10 seconds. Each portion had five indentations put in it. A Modified Transient Plane Source (MTPS) (ASTM D7984

[148]) single-sided sensor (Trident, C-Therm Technologies Ltd, Frederiction, Canada) was used to measure the thermal conductivity at room temperature on cylinders (ø24.3 mm × 2.1 mm) made following one of the finest production practices. To make a point, complicated gyroids were created.

5.2 Results and discussion

Feedstock characterization

The diameter of the filament as it was delivered was measured to be 1.753 ± 0.004 mm. With $\sigma = 0.0042$ and $\mu = 1.753$, the measured distribution (shown in Figure 50-a) follows a roughly normal distribution. Zirconia particles in the nanoscale range are visible in cross-sections of the filament after SEM inspection (Figure 50-b).

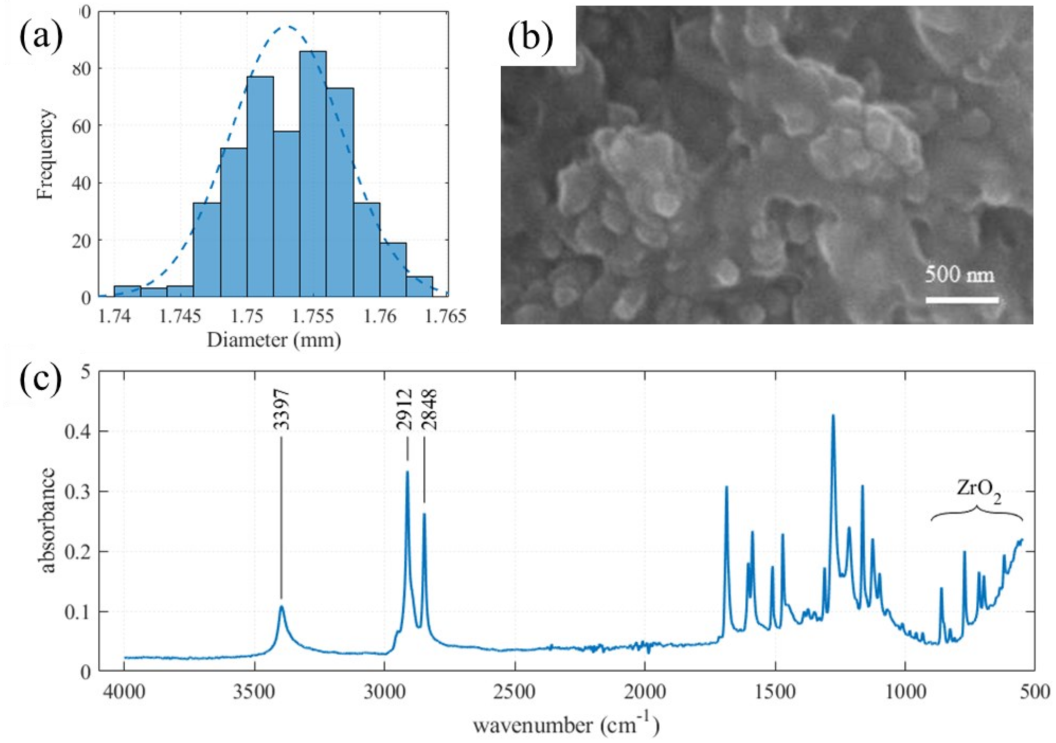

Figure 50. (a) Histogram of the measured diameter distribution of the zirconia filament. (b) SEM picture of a cross-sectional area of the zirconia filament. (c) FT-IR spectrum of the as-purchased zirconia filament.

The significant peaks at 2912 and 2848 cm in the zirconia-based filament's absorbance FT-IR spectra enabled for the identification of polyethylene as the filament's main polymer (Figure 50-c). Primary aliphatic amine was linked to an extra peak in the 3397 cm^{-1} range [149]. The 900 and 500 cm^{-1} regions included the characteristic zirconia particle peaks. According to the TGA data (Figure 51-a), a total weight loss of 14.49% was observed, which corresponds to a feedstock powder load (weight ratio) of 85.51 %wt. Furthermore, with start decomposition temperatures of 170 °C, 385 °C, and > 500 °C, respectively, it is possible to discern between the presence of three different types of binders in various ratios. The melting of a binder, thought to be paraffin wax, is indicated by an endothermic peak in the DSC curve (Figure 51-a) at 55.1 °C. The temperature for thermal debinding is later determined to be between 150 and 450 °C, when most of the weight loss takes place. 14.49% of the total weight is lost, which is the same amount as the weight loss experienced following solvent and heat debinding (see section 7.1).

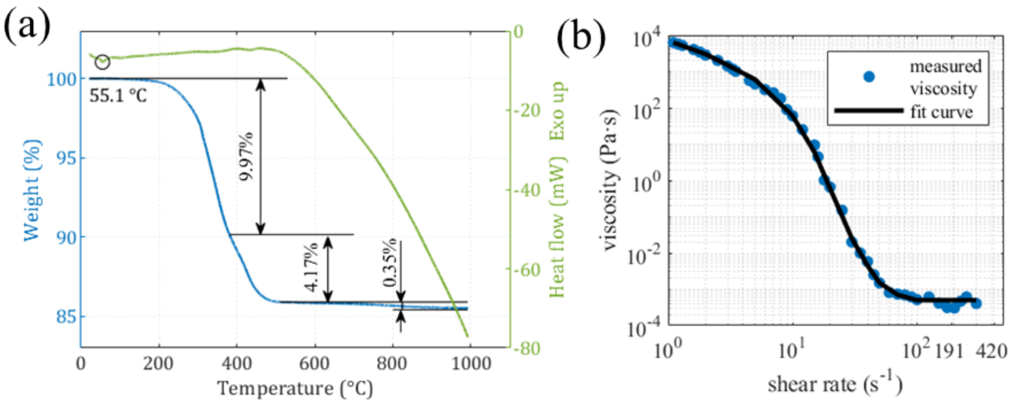

Figure 51. (a) TGA (blue) and DSC (green) curve of the zirconia filament. (b) Viscosity of the feedstock melt at 180 °C as a function of shear rate and its spline fit curve.

The rheological information (Figure 51-b) shows that the viscosity rapidly decreases by eight orders of magnitude from the lowest to the highest shear regime, reaching an infinite-shear viscosity of 5×10^{-4} Pa·s, which is equivalent to the shear rate used during printing (share rates under printing > 102 s^{-1}). This infinite-shear viscosity is especially low when compared to conventional MEX filament polymeric data (in-house testing and analyzed literature data), most likely because the right binder system allowed for well-dispersing the nanometric zirconia particles.

3D printing

For an achievable printing speed of 30 mm/s, Figure 52 shows a color map of the relative green density of ZrO_2 printed samples as a function of the flow rate multiplier and layer thickness. High density printed objects benefit from decreasing the layer thickness and increasing the flow rate multiplier; regardless of the other parameters, relative green densities > 98% are easily attainable with a flow rate multiplier > 100%. According to statistics, the flow rate multiplier, layer thickness, and their interaction are the most important variables, whereas the relevance of printing speed is minimal (Table 20). The coefficient (R^2) of the regression model is 0.91.

Table 20 . Results of the Analysis of Variance (ANOVA) of the effect of printing factors on the green part densities.

Source	Sum Sq.	p-value
Layer thickness	0.02892	2.83×10^{-06}
Printing speed	0.00156	4.30×10^{-01}
Flowrate multiplier	0.43473	8.41×10^{-30}
Layer thickness * printing speed	0.00485	2.70×10^{-1}
Layer thickness * flowrate multiplier	0.03315	7.87×10^{-06}
Printing speed * flowrate multiplier	0.00286	5.42×10^{-1}
Error	0.05669	
Total	0.56726	

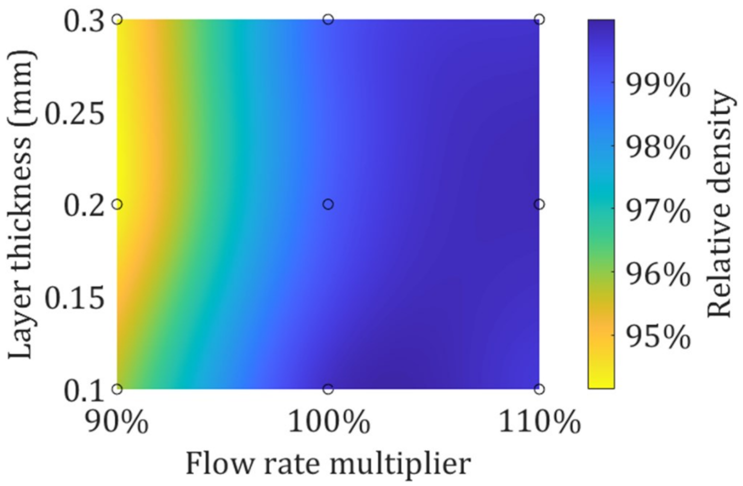

Figure 52. Colour map of relative densities of zirconia printed green samples as a function of flow rate multiplier and layer thickness at a representative printing speed of 30 mm/s (interpolated data). The circles represent the location of the experimental data points.

These patterns are in line with how the MEX process using filament feedstock is generally understood. Particularly in the case of low viscosity melts, a high flow rate multiplier causes over-extrusion of material, which is advantageous to fill the gaps of printing. Due to the increased porosity of the printed item brought on by the deposition of strands with nearly circular cross sections, this contribution becomes even more significant when printing with high layer thickness (or, more accurately, with layer height closer to the nozzle diameter). In contrast, a lower layer thickness in relation to the nozzle diameter is somewhat in favor of flat strand deposition with nearly rectangular cross-sectional profiles, which reduces the space between consecutive strands and overlapping layers and, consequently, the porosity of the printed object [150]. The low viscosity of the feedstock utilized can also be blamed for the negligible printing speed.

From the post-processing technique outlined in section 7.1, the prismatic samples produced at 30 mm/s were then chosen for post-printing processing via solvent, heat debinding, and sintering. As a result, Table 21's summary of two best-practice production strategies could be found. They were used to produce samples and biaxial flexural discs. They were distinguished by a green relative density > 98% and a sintered relative density > 99%.

Table 21. Best-practice manufacturing strategies.

	01_100_30	02_110_30
Layer thickness (mm)	0.1	0.2
Flow rate multiplier	100%	110%
Printing speed (mm/s)	30	30
Green relative density[1]	98.87 ± 0.03%	98.84 ± 0.02%
Sintered relative density[2]	99.99 ± 0.14%	99.38 ± 0.06%

[1] Normalised to the density of the zirconia filament, 3.55 g/cm^3

[2] Normalised to the theoretical density of zirconia (3Y-TZP), 6.05 g/cm^3

Characterization of sintered parts

Table 22 provides a summary of the physical and mechanical parameters of the sintered samples. The cross-sections of example sintered prismatic parts produced using best-practice production procedures 01_100_30 (a) and 02_110_30 (b) are shown in BSE images in Figure 53. The cross-sections demonstrate a microstructure that is nearly completely dense and has few aligned and randomly scattered pores. Particularly, in the cross-sections of pieces 01_100_30 and 02_110_30, elongated and layer-aligned residual holes with maximum lengths of 60 m and 120 m, respectively, were found. Inhomogeneity in the material feedstock, air bubbles in the low viscosity melt, or printing flaws can all be blamed for the occurrence of pores. The wider inter-filament space caused by the thicker printing layer in the 02_110_30 samples may be the cause of the samples' larger fault sizes.

While the flexural strength varied significantly between the two manufacturing methods, the measured Vickers hardness was comparable for both. Weibull modulus was 2.66 and characteristic strength was 730 MPa for the discs produced with printing strategy 01_100_30, while these values were 4.91 and 871 MPa for the discs printed with printing strategy 02_110_30.

Table 22. Mechanical and thermal characteristics of 3Y-TZP discs and samples realised with best-practice manufacturing strategies.

Best-practice manufacturing strategies	01_100_30	02_110_30
Vickers hardness (GPa)	12.98 ± 0.03	12.90 ± 0.33
Weibull modulus	2.66	4.91
Characteristic strength (MPa)	730	871
Thermal conductivity (W/mK)	/	3.62 ± 0.08

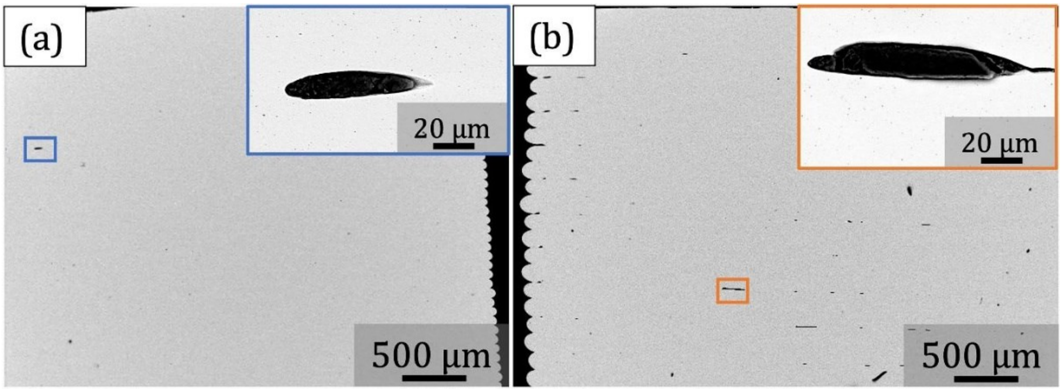

Figure 53. Backscattered Electron (BSE) images of representative cross-sections of sintered prismatic parts realised via best-practice manufacturing strategies 01_100_30 (a) and 02_110_30 (b).

In comparison to the 01_100_30 approach, the higher Weibull modulus found with the 02_110_30 strategy should be attributed to the presence of a double printing layer thickness, which implies printing half as many layers and a lower probability of generating printing errors. The achieved characteristic flexural strength is acceptable and on par with the reported 702 MPa for conventional ceramic processing [151] as well as other additive manufacturing technologies, such as 778-1071 MPa for stereolithography [152,153] and 1061 MPa for material jetting [154]. However, the Weibull modulus is still small compared to the studies described above, which range from 6.5 to 16.3, most likely because the MEX process employing filament feedstock has a greater intrinsic defect-inducing character.

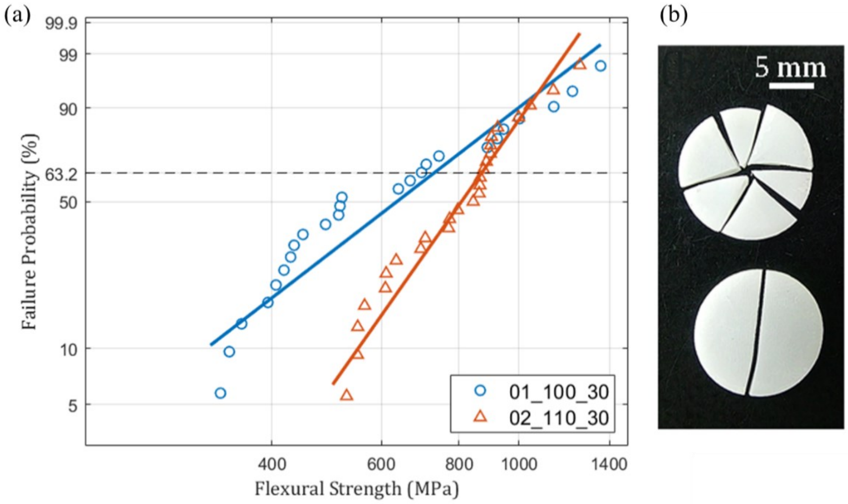

Figure 54. (a)Weibull plot of the biaxial flexural strength of 3Y-TZP. (b)fractured discs after mechanical testing (bottom = low strength, top = high strength).

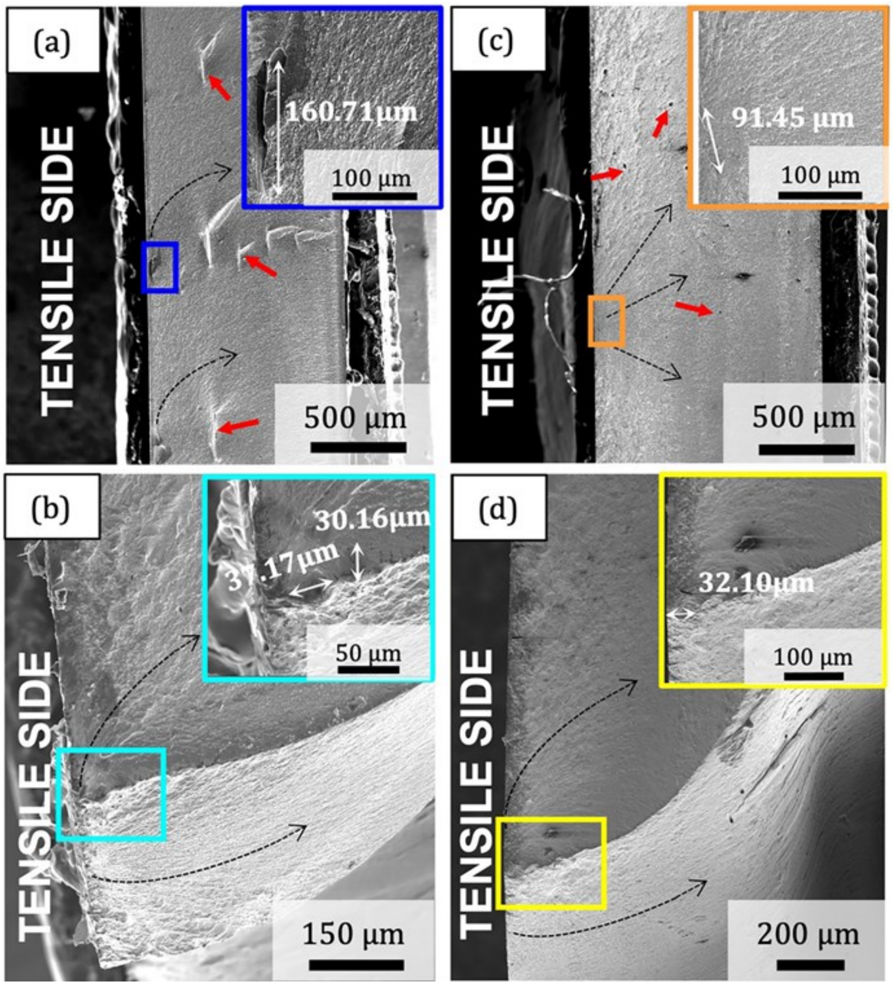

Figure 55. Secondary electron (SE) images of the biaxial fracture surface of 3Y-TZP discs manufactured by MEX using printing strategy 01 100 30 (a,b) and 02 110 30 (c,d). Indicative measurements of the critical flaw size.

Figure 55 depicts the fractography examination of several biaxially broken discs. Two 01_100_30 discs with flexural strengths of 630 MPa and 1130 MPa (Figure 55-a and -b, respectively) and two 02_110_30 discs with the same strengths (630 MPa and 1130 MPa, respectively) were examined (Figure 55-c and -d, respectively). The black arrows with a dash depict the direction in which the discovered significant faults caused the observed cracks to propagate on the fracture surface. On the flat surfaces that were subjected to tensile loads during testing, the fracture initiation locations were all evident. The fracture initiation site for the low strength 01_100_30 portion was determined to be an elongated void that was indicatively 160 m long, orientated with the printing direction, as shown in the magnified image (blue box in Figure 55-a). Interlayer flaws were responsible for a number of pores of the same type that were seen scattered across the whole fracture surface (shown by the red arrows). On the other hand, the essential flaw for the low strength 02_110_30 part (Figure 55-c) was found to be a printing-induced defect that was smaller in size and (nearly) spherical in shape (as indicated by the orange box in Figure 55-c). On the fracture surface, spherical isolated pores (shown by red arrows) were also found. The fracture surface was examined for the high-strength portions at low (Figure 55-b and -d) and high magnification (light blue and yellow box). While the latter made it possible to measure the size of the pores from which the crack originated, the former indicated the direction of the crack. The essential flaws are spherical in nature and roughly the same size in both situations. Spherical pores should develop in the filament in relation to air bubbles or particle-free ZrO_2 polymer aggregates. Finally, the fabrication of cylinders for thermal characterization was chosen using strategy 02_110_30. The published value of 3.2 W/mK for normally pressed and sintered fully dense 3Y-TZP [155] is in good agreement with the measured thermal conductivity of 3.620.08 W/mK at room temperature (Table 22).

Gyroid demonstrator

To demonstrate the shaping potential of the MEX technology, gyroid components (green size 30 × 30 × 7 mm^3) were manufactured (Figure 56). It was discovered that there was an 18% linear sintering shrinkage, which is consistent with the 19.89 ± 0.62% shrinkage observed on prismatic pieces during the experimental campaign. The shrinkage value is in good agreement with the linear shrinkage of ceramic using MEX and injection molding in other studies analyzed in the state of the art section- between 18% and 21%. There was no evidence of warpage or distortion in the printed portions. Gyroid components (30 × 30 × 7 mm^3, green)

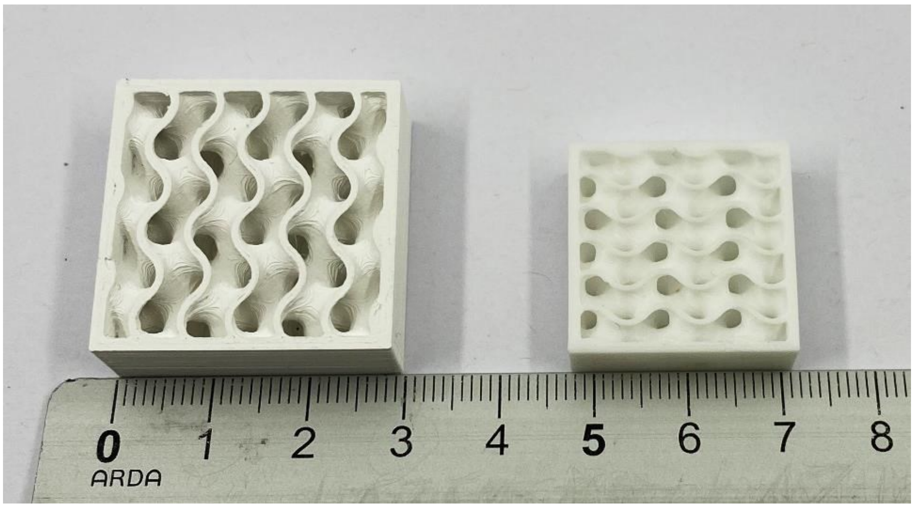

Figure 56. Green (left) and sintered (right) zirconia gyroid structures.

5.3 Conclusions

The ability to print highly dense zirconia components (relative densities > 99%) with acceptable mechanical properties (Vickers hardness of 12.90 GPa, characteristic flexural strength up to 871 MPa, and Weibull modulus of 4.9) and typical low thermal conductivity (3.62 W/mK at room temperature was demonstrated using material extrusion-based additive manufacturing using ceramic filament feedstock. At the printing-specific shear rates (510 Pa at 102 s–4), the commercially available filament feedstock was distinguished by having a very low viscosity. The printing parameters' DoE and ANOVA tests revealed that the layer thickness and flow rate multiplier had a substantial impact on the green density. Critical flaws of varying size (indicatively in the range of 30 to 160 m) of both spherical and elongated character, related to inhomogeneities in the filament and interfilament spacing printing faults, respectively, were discovered by analysis of the fractured surfaces. Successful demonstration model production was accomplished. The approach that combines statistical analysis of the printing process (DoE, ANOVA) with filament characterization (TGA, SEM, rheology, etc.) also succeeds and can be applied to other commercial filaments, regardless of the filler type and precise binder formulation.

Chapter 6

CONCLUSIONS

This research is situated within a broader global context, aimed at proposing experimental methodologies for characterizing filament-based Material Extrusion Additive Manufacturing (MEX) processes. The primary goal is to enhance the mechanical and thermal properties of components intended for industrial, aerospace, and aviation applications. The study spans a wide range of materials, progressing from commodity polymers to techno-polymers, composites, and ceramics. This diversity allows for a comprehensive exploration of the technology's potential benefits across diverse industrial and aerospace scenarios.

The investigation into thermal conductivity characteristics, particularly focusing on PLA samples, yielded significant insights. By maintaining other process variables while varying infill percentage and layer count, the study revealed a direct relationship between thermal conductivity and the number of layers and infill percentage. This understanding is vital for optimizing additive manufacturing procedures, particularly in applications demanding precise internal thermal properties and heat management.

A comparative analysis was conducted to evaluate the impact of annealing methods on PEEK. It was observed that both oven annealing and direct annealing had a limited effect on flexural strength, with temperature being the predominant factor. Notably, 300°C emerged as the most effective treatment temperature. While oven annealing led to higher mechanical performance, it also entailed significantly longer manufacturing times. In contrast, direct annealing at 300°C proved to be more cost-effective when considering production time as just the printing duration, offering advantages for the PEEK printing process.

The study investigating the performance of Onyx specimens with various infill patterns and printing orientations yielded valuable results. Tensile testing indicated the superiority of gyroid-type infill in terms of tensile strength, regardless of print orientation. In flexural testing, all infill patterns performed similarly, highlighting the reliability of the gyroid infill. Moreover, variations in printing durations and manufacturing costs were identified based on the chosen infill pattern, making gyroid infill the preferred choice due to its balanced characteristics.

Lastly, the research demonstrated the capability to produce highly dense zirconia components with exceptional mechanical properties and low thermal conductivity through material extrusion-based additive manufacturing using ceramic filament feedstock. The importance of specific printing parameters, including layer thickness and flow rate multiplier, was highlighted in achieving the desired green density. Additionally, an analysis of fractured surfaces revealed critical flaws associated with inhomogeneities in the filament and interfilament spacing printing faults.

In summary, this research represents a pivotal advancement in our comprehension of filament-based material extrusion processes and their applicability across a wide spectrum of materials, spanning from polymers to ceramics. The findings not only provide valuable insights but underscore the critical importance of a comprehensive understanding of material properties, including thermal and rheological characteristics, as well as the precise parameters governing the manufacturing process.

This understanding serves as the linchpin for optimizing manufacturing processes, aiding in judicious material selection, and fine-tuning essential parameters. This optimization is especially crucial when considering the stringent demands of industries such as aerospace, aeronautics, naval, automotive, and more. The research outcomes directly contribute to the augmentation of mechanical and thermal properties in additive manufacturing, thereby enabling the creation of components tailored to meet the exacting standards of these industries.

REFERENCES

[1] S.A.M. Tofail, E.P. Koumoulos, A. Bandyopadhyay, S. Bose, L. O'Donoghue, C. Charitidis, Additive manufacturing: scientific and technological challenges, market uptake and opportunities, Materials Today 21 (2018) 22–37. https://doi.org/10.1016/j.mattod.2017.07.001.

[2] L.M. Galantucci, M.G. Guerra, M. Dassisti, F. Lavecchia, Additive Manufacturing: New Trends in the 4th Industrial Revolution, in: Lecture Notes in Mechanical Engineering, Springer International Publishing, 2019: pp. 153–169. https://doi.org/10.1007/978-3-030-18180-2_12.

[3] L.M. Galantucci, M.G. Guerra, M. Dassisti, F. Lavecchia, Additive Manufacturing: New Trends in the 4th Industrial Revolution, in: 2019: pp. 153–169. https://doi.org/10.1007/978-3-030-18180-2_12.

[4] I. Campbell, D. Bourell, I. Gibson, Additive manufacturing: rapid prototyping comes of age, Rapid Prototyp J 18 (2012) 255–258. https://doi.org/10.1108/13552541211231563.

[5] ASTM/ISO 52900:2021 - Additive manufacturing - General principles, (2021).

[6] N. Jones, Science in three dimensions: The print revolution, Nature 487 (2012) 22–23. https://doi.org/10.1038/487022a.

[7] B.P. Conner, G.P. Manogharan, A.N. Martof, L.M. Rodomsky, C.M. Rodomsky, D.C. Jordan, J.W. Limperos, Making sense of 3-D printing: Creating a map of additive manufacturing products and services, Addit Manuf 1–4 (2014) 64–76. https://doi.org/10.1016/j.addma.2014.08.005.

[8] T.D. Ngo, A. Kashani, G. Imbalzano, K.T.Q. Nguyen, D. Hui, Additive manufacturing (3D printing): A review of materials, methods, applications and challenges, Compos B Eng 143 (2018) 172–196. https://doi.org/10.1016/j.compositesb.2018.02.012.

[9] S.C. Altıparmak, V.A. Yardley, Z. Shi, J. Lin, Extrusion-based additive manufacturing technologies: State of the art and future perspectives, J Manuf Process 83 (2022) 607–636. https://doi.org/10.1016/j.jmapro.2022.09.032.

[10] B.N. Turner, S.A. Gold, A review of melt extrusion additive manufacturing processes: II. Materials, dimensional accuracy, and surface roughness, Rapid Prototyp J 21 (2015) 250–261. https://doi.org/10.1108/RPJ-02-2013-0017.

[11] H. Hur, Y. Jin Park, D.H. Kim, J. Wan Ko, Material extrusion for ceramic additive manufacturing with polymer-free ceramic precursor binder, Mater Des 221 (2022) 110930. https://doi.org/10.1016/J.MATDES.2022.110930.

[12] R. Chen, A. Bratten, J. Rittenhouse, M.C. Leu, H. Wen, Additive manufacturing of continuous carbon fiber-reinforced SiC ceramic composite with multiple fiber bundles by an extrusion-based technique, Ceram Int 49 (2023) 9839–9847. https://doi.org/10.1016/J.CERAMINT.2022.11.157.

[13] J.K. Bagwan, B.B. Ahuja, Understanding and investigating rheological properties of HA/β-TCP bio-ceramic composite ink for extrusion-based additive manufacturing process to fabricate bone scaffold, Mater Today Proc 72 (2023) 911–917. https://doi.org/10.1016/J.MATPR.2022.09.090.

[14] S. Whyman, K.M. Arif, J. Potgieter, Design and development of an extrusion system for 3D printing biopolymer pellets, The International Journal of Advanced Manufacturing Technology 96 (2018) 3417–3428. https://doi.org/10.1007/s00170-018-1843-y.

[15] N. Volpato, D. Kretschek, J.A. Foggiatto, C.M. Gomez da Silva Cruz, Experimental analysis of an extrusion system for additive manufacturing based on polymer pellets, The International Journal of Advanced Manufacturing Technology 81 (2015) 1519–1531. https://doi.org/10.1007/s00170-015-7300-2.

[16] N. Kumar, P.K. Jain, P. Tandon, P.M. Pandey, Extrusion-based additive manufacturing process for producing flexible parts, Journal of the Brazilian Society of Mechanical Sciences and Engineering 40 (2018) 143. https://doi.org/10.1007/s40430-018-1068-x.

[17] J. Gonzalez-Gutierrez, S. Cano, S. Schuschnigg, C. Kukla, J. Sapkota, C. Holzer, Additive Manufacturing of Metallic and Ceramic Components by the Material Extrusion of Highly-Filled Polymers: A Review and Future Perspectives, Materials 11 (2018) 840. https://doi.org/10.3390/ma11050840.

[18] J. Gonzlez-Gutirrez, G. Beulke, I. Emri, Powder Injection Molding of Metal and Ceramic Parts, in: Some Critical Issues for Injection Molding, InTech, 2012. https://doi.org/10.5772/38070.

[19] Z. Lotfizarei, A. Mostafapour, A. Barari, A. Jalili, A.E. Patterson, Overview of debinding methods for parts manufactured using powder material extrusion, Addit Manuf 61 (2023) 103335. https://doi.org/10.1016/j.addma.2022.103335.

[20] L. Gorjan, C. Galusca, M. Sami, T. Sebastian, F. Clemens, Effect of stearic acid on rheological properties and printability of ethylene vinyl acetate based feedstocks for fused filament fabrication of alumina, Addit Manuf 36 (2020) 101391. https://doi.org/10.1016/j.addma.2020.101391.

[21] F. Cerejo, D. Gatões, M.T. Vieira, Optimization of metallic powder filaments for additive manufacturing extrusion (MEX), The International Journal of Advanced Manufacturing Technology 115 (2021) 2449–2464. https://doi.org/10.1007/s00170-021-07043-0.

[22] K.E. Hrdina, J.W. Halloran, Dimensional changes during binder removal in a mouldable ceramic system, J Mater Sci 33 (1998) 2805–2815. https://doi.org/10.1023/A:1017577517999.

[23] S.C. Danforth, Fused deposition of ceramics: a new technique for the rapid fabrication of ceramic components, Materials Technology 10 (1995) 144–146. https://doi.org/10.1080/10667857.1995.11752614.

[24] I. Özden, A. Iveković, A. Kocjan, Additive manufacturing of ceramics from thermoplastic feedstocks, Open Ceramics 6 (2021) 100129. https://doi.org/10.1016/j.oceram.2021.100129.

[25] Z. Chen, Z. Li, J. Li, C. Liu, C. Lao, Y. Fu, C. Liu, Y. Li, P. Wang, Y. He, 3D printing of ceramics: A review, J Eur Ceram Soc 39 (2019) 661–687. https://doi.org/10.1016/j.jeurceramsoc.2018.11.013.

[26] J. Abel, U. Scheithauer, T. Janics, S. Hampel, S. Cano, A. Müller-Köhn, A. Günther, C. Kukla, T. Moritz, Fused Filament Fabrication (FFF) of Metal-Ceramic Components, Journal of Visualized Experiments (2019). https://doi.org/10.3791/57693.

[27] L. Auffray, P.-A. Gouge, L. Hattali, Design of experiment analysis on tensile properties of PLA samples produced by fused filament fabrication, The International Journal of Advanced Manufacturing Technology 118 (2022) 4123–4137. https://doi.org/10.1007/s00170-021-08216-7.

[28] J.M. Chacón, M.A. Caminero, E. García-Plaza, P.J. Núñez, Additive manufacturing of PLA structures using fused deposition modelling: Effect of process parameters on mechanical properties and their optimal selection, Mater Des 124 (2017) 143–157. https://doi.org/10.1016/j.matdes.2017.03.065.

[29] G.D. Goh, Y.L. Yap, H.K.J. Tan, S.L. Sing, G.L. Goh, W.Y. Yeong, Process–Structure–Properties in Polymer Additive Manufacturing via Material Extrusion: A Review, Critical Reviews in Solid State and Materials Sciences 45 (2020) 113–133. https://doi.org/10.1080/10408436.2018.1549977.

[30] E. Cuan-Urquizo, E. Barocio, V. Tejada-Ortigoza, R.B. Pipes, C.A. Rodriguez, A. Roman-Flores, Characterization of the Mechanical Properties of FFF Structures and Materials: A Review on the Experimental, Computational and Theoretical Approaches, Materials 2019, Vol. 12, Page 895 12 (2019) 895. https://doi.org/10.3390/MA12060895.

[31] S. Garzon-Hernandez, D. Garcia-Gonzalez, A. Jérusalem, A. Arias, Design of FDM 3D printed polymers: An experimental-modelling methodology for the prediction of mechanical properties, Mater Des 188 (2020) 108414. https://doi.org/10.1016/J.MATDES.2019.108414.

[32] V.M. Akhil, S.L. Aravind, R. Kiran, S. S P, S. Mohan, Experimental investigations on the effect of infill patterns on PLA for structural applications, Mater Today Proc (2022). https://doi.org/10.1016/j.matpr.2022.10.292.

[33] C. Lubombo, M.A. Huneault, Effect of infill patterns on the mechanical performance of lightweight 3D-printed cellular PLA parts, Mater Today Commun 17 (2018) 214–228. https://doi.org/10.1016/J.MTCOMM.2018.09.017.

[34] M.L. Dezaki, M.K.A.M. Ariffin, A. Serjouei, A. Zolfagharian, S. Hatami, M. Bodaghi, Influence of infill patterns generated by cad and fdm 3d printer on surface roughness and tensile strength properties, Applied Sciences (Switzerland) 11 (2021). https://doi.org/10.3390/app11167272.

[35] K. Wang, X. Xie, J. Wang, A. Zhao, Y. Peng, Y. Rao, Effects of infill characteristics and strain rate on the deformation and failure properties of additively manufactured polyamide-based composite structures, Results Phys 18 (2020). https://doi.org/10.1016/j.rinp.2020.103346.

[36] J. Ghorbani, P. Koirala, Y.-L. Shen, M. Tehrani, Eliminating voids and reducing mechanical anisotropy in fused filament fabrication parts by adjusting the filament extrusion rate, J Manuf Process 80 (2022) 651–658. https://doi.org/10.1016/j.jmapro.2022.06.026.

[37] N. Dialami, M. Chiumenti, M. Cervera, U. Chasco, G. Reyes-Pozo, M.A. Pérez, A hybrid numerical-experimental strategy for predicting mechanical response of components manufactured via FFF, Compos Struct 298 (2022) 115998. https://doi.org/10.1016/j.compstruct.2022.115998.

[38] J. Djokikj, O. Tuteski, E. Doncheva, B. Hadjieva, Experimental investigation on mechanical properties of FFF parts using different materials, Procedia Structural Integrity 41 (2022) 670–679. https://doi.org/10.1016/j.prostr.2022.05.076.

[39] A. Ramalho, D. Freitas, H. Almeida, The anisotropy and friction effect in the design of 3D printed PLA parts – A case study, Mater Today Proc (2023). https://doi.org/10.1016/j.matpr.2023.08.196.

[40] X. Gao, S. Qi, X. Kuang, Y. Su, J. Li, D. Wang, Fused filament fabrication of polymer materials: A review of interlayer bond, Addit Manuf 37 (2021) 101658. https://doi.org/10.1016/j.addma.2020.101658.

[41] S. Ahn, M. Montero, D. Odell, S. Roundy, P.K. Wright, Anisotropic material properties of fused deposition modeling ABS, Rapid Prototyp J 8 (2002) 248–257. https://doi.org/10.1108/13552540210441166.

[42] S.F. Costa, F.M. Duarte, J.A. Covas, Estimation of filament temperature and adhesion development in fused deposition techniques, J Mater Process Technol 245 (2017) 167–179. https://doi.org/10.1016/j.jmatprotec.2017.02.026.

[43] N. Zohdi, R. (Chunhui) Yang, Material Anisotropy in Additively Manufactured Polymers and Polymer Composites: A Review, Polymers (Basel) 13 (2021) 3368. https://doi.org/10.3390/polym13193368.

[44] F. Bähr, E. Westkämper, Correlations between Influencing Parameters and Quality Properties of Components Produced by Fused Deposition Modeling, Procedia CIRP 72 (2018) 1214–1219. https://doi.org/10.1016/j.procir.2018.03.048.

[45] S. Bardiya, J. Jerald, V. Satheeshkumar, Effect of process parameters on the impact strength of fused filament fabricated (FFF) polylactic acid (PLA) parts, Mater Today Proc 41 (2021) 1103–1106. https://doi.org/10.1016/J.MATPR.2020.08.066.

[46] J. Wang, Polyether Ether Ketone, in: Handbook of Engineering and Speciality Thermoplastics: Polyethers and Polyesters, 2011: pp. 55–95. https://doi.org/10.1002/9781118104729.ch3.

[47] R. Singh, G. Singh, J. Singh, R. Kumar, 3D Printing of Polyether-Ether-Ketone Functional Prototypes for Engineering Applications, Elsevier Ltd., 2020. https://doi.org/10.1016/b978-0-12-803581-8.11543-7.

[48] Y. Zhao, K. Zhao, Y. Li, F. Chen, Mechanical characterization of biocompatible PEEK by FDM, J Manuf Process 56 (2020) 28–42. https://doi.org/10.1016/j.jmapro.2020.04.063.

[49] M. Vaezi, S. Yang, Extrusion-based additive manufacturing of PEEK for biomedical applications, Virtual Phys Prototyp 10 (2015) 123–135. https://doi.org/10.1080/17452759.2015.1097053.

[50] Y. Wang, W.D. Müller, A. Rumjahn, F. Schmidt, A.D. Schwitalla, Mechanical properties of fused filament fabricated PEEK for biomedical applications depending on additive manufacturing parameters, J Mech Behav Biomed Mater 115 (2021) 104250. https://doi.org/10.1016/J.JMBBM.2020.104250.

[51] A. El Magri, S. Vaudreuil, Effects of physical and chemical ageing on 3D printed poly (ether ether ketone)/poly (ether imide) [PEEK/PEI] blend for aerospace applications, J Mater Sci 58 (2023) 1465–1479. https://doi.org/10.1007/S10853-022-08068-W/FIGURES/9.

[52] B. Valentan, Ž. Kadivnik, T. Brajlih, A. Anderson, I. Drstvenšek, Processing poly(ether etherketone) on a 3d printer for thermoplastic modelling, Materiali in Tehnologije 47 (2013) 715–721.

[53] P. Geng, J. Zhao, W. Wu, W. Ye, Y. Wang, S. Wang, S. Zhang, Effects of extrusion speed and printing speed on the 3D printing stability of extruded PEEK filament, J Manuf Process 37 (2019) 266–273. https://doi.org/10.1016/j.jmapro.2018.11.023.

[54] M.F. Arif, S. Kumar, K.M. Varadarajan, W.J. Cantwell, Performance of biocompatible PEEK processed by fused deposition additive manufacturing, Mater Des 146 (2018) 249–259. https://doi.org/10.1016/j.matdes.2018.03.015.

[55] P. Wang, B. Zou, H. Xiao, S. Ding, C. Huang, Effects of printing parameters of fused deposition modeling on mechanical properties, surface quality, and microstructure of PEEK, J Mater Process Technol 271 (2019) 62–74. https://doi.org/10.1016/j.jmatprotec.2019.03.016.

[56] J. Pu, C. McIlroy, A. Jones, I. Ashcroft, Understanding mechanical properties in fused filament fabrication of polyether ether ketone, Addit Manuf 37 (2021) 101673. https://doi.org/10.1016/J.ADDMA.2020.101673.

[57] A. Pulipaka, K.M. Gide, A. Beheshti, Z.S. Bagheri, Effect of 3D printing process parameters on surface and mechanical properties of FFF-printed PEEK, J Manuf Process 85 (2023) 368–386. https://doi.org/10.1016/J.JMAPRO.2022.11.057.

[58] M. Rinaldi, T. Ghidini, F. Cecchini, A. Brandao, F. Nanni, Additive layer manufacturing of poly (ether ether ketone) via FDM, Compos B Eng 145 (2018) 162–172. https://doi.org/10.1016/j.compositesb.2018.03.029.

[59] Victrex, High Performance Paek Polymers. VICTREX ® PEEK 450P datasheet. 2014., (n.d.). https://www.victrex.com/en/datasheets (accessed July 6, 2023).

[60] H.X. Nguyen, H. Ishida, Poly(aryl-ether-ether-ketone) and its advanced composites: A review, Polym Compos 8 (1987) 57–73. https://doi.org/10.1002/PC.750080202.

[61] J.K. Fink, Handbook of Engineering and Speciality Thermoplastics, Handbook of Engineering and Speciality Thermoplastics 1 (2010). https://doi.org/10.1002/9780470881712.

[62] D.P. Jones, D.C. Leach, D.R. Moore, Mechanical properties of poly(ether-ether-ketone) for engineering applications, Polymer (Guildf) 26 (1985) 1385–1393. https://doi.org/10.1016/0032-3861(85)90316-7.

[63] X. Deng, Z. Zeng, B. Peng, S. Yan, W. Ke, Mechanical Properties Optimization of Poly-Ether-Ether-Ketone via Fused Deposition Modeling, Materials 11 (2018) 216. https://doi.org/10.3390/ma11020216.

[64] A.R. Zanjanijam, I. Major, J.G. Lyons, U. Lafont, D.M. Devine, Fused Filament Fabrication of PEEK: A Review of Process-Structure-Property Relationships, Polymers (Basel) 12 (2020) 1665. https://doi.org/10.3390/polym12081665.

[65] M.F. Arif, S. Kumar, K.M. Varadarajan, W.J. Cantwell, Performance of biocompatible PEEK processed by fused deposition additive manufacturing, Mater Des 146 (2018) 249–259. https://doi.org/10.1016/J.MATDES.2018.03.015.

[66] W. Wu, P. Geng, G. Li, D. Zhao, H. Zhang, J. Zhao, Influence of Layer Thickness and Raster Angle on the Mechanical Properties of 3D-Printed PEEK and a Comparative Mechanical Study between PEEK and ABS, Materials 2015, Vol. 8, Pages 5834-5846 8 (2015) 5834–5846. https://doi.org/10.3390/MA8095271.

[67] C. Yang, X. Tian, D. Li, Y. Cao, F. Zhao, C. Shi, Influence of thermal processing conditions in 3D printing on the crystallinity and mechanical properties of PEEK material, J Mater Process Technol 248 (2017) 1–7. https://doi.org/10.1016/j.jmatprotec.2017.04.027.

[68] C. Basgul, T. Yu, D.W. Macdonald, R. Siskey, M. Marcolongo, S.M. Kurtz, Structure-property relationships for 3D-printed PEEK intervertebral lumbar cages produced using fused filament fabrication, J Mater Res 33 (2018) 2040–2051. https://doi.org/10.1557/JMR.2018.178/FIGURES/8.

[69] A. El Magri, S. Vaudreuil, K. El Mabrouk, M.E. Touhami, Printing temperature effects on the structural and mechanical performances of 3D printed Poly-(phenylene sulfide) material, IOP Conf Ser Mater Sci Eng 783 (2020). https://doi.org/10.1088/1757-899X/783/1/012001.

[70] A. El Magri, S. Vanaei, S. Vaudreuil, An overview on the influence of process parameters through the characteristic of 3D-printed PEEK and PEI parts, High Perform Polym 33 (2021) 862–880. https://doi.org/10.1177/09540083211009961.

[71] A. El Magri, S. Vaudreuil, A. Ben Ayad, A. El Hakimi, R. El Otmani, D. Amegouz, Effect of printing parameters on tensile, thermal and structural properties of <scp>3D</scp> -printed poly (ether ketone ketone) <scp>PEKK</scp> material using fused deposition modeling, J Appl Polym Sci 140 (2023). https://doi.org/10.1002/app.54078.

[72] A. El Magri, K. El Mabrouk, S. Vaudreuil, H. Chibane, M.E. Touhami, Optimization of printing parameters for improvement of mechanical and

thermal performances of 3D printed poly(ether ether ketone) parts, J Appl Polym Sci 137 (2020) 1–14. https://doi.org/10.1002/app.49087.

[73] L. Jin, J. Ball, T. Bremner, H.J. Sue, Crystallization behavior and morphological characterization of poly(ether ether ketone), Polymer (Guildf) 55 (2014) 5255–5265. https://doi.org/10.1016/j.polymer.2014.08.045.

[74] C.Y. Liaw, J.W. Tolbert, L.W. Chow, M. Guvendiren, Interlayer bonding strength of 3D printed PEEK specimens, Soft Matter 17 (2021) 4775–4789. https://doi.org/10.1039/d1sm00417d.

[75] A. Lee, M. Wynn, L. Quigley, M. Salviato, N. Zobeiry, Effect of temperature history during additive manufacturing on crystalline morphology of PEEK, Advances in Industrial and Manufacturing Engineering 4 (2022) 100085. https://doi.org/10.1016/j.aime.2022.100085.

[76] C. Basgul, T. Yu, D.W. MacDonald, R. Siskey, M. Marcolongo, S.M. Kurtz, Does annealing improve the interlayer adhesion and structural integrity of FFF 3D printed PEEK lumbar spinal cages?, J Mech Behav Biomed Mater 102 (2020) 103455. https://doi.org/10.1016/j.jmbbm.2019.103455.

[77] Z. Jiang, P. Liu, H.J. Sue, T. Bremner, Effect of annealing on the viscoelastic behavior of poly(ether-ether-ketone), Polymer (Guildf) 160 (2019) 231–237. https://doi.org/10.1016/j.polymer.2018.11.052.

[78] K. Rodzeń, E. Harkin-Jones, M. Wegrzyn, P.K. Sharma, A. Zhigunov, Improvement of the layer-layer adhesion in FFF 3D printed PEEK/carbon fibre composites, Compos Part A Appl Sci Manuf 149 (2021) 106532. https://doi.org/10.1016/j.compositesa.2021.106532.

[79] T.J. Hoskins, K.D. Dearn, S.N. Kukureka, Mechanical performance of PEEK produced by additive manufacturing, Polym Test 70 (2018) 511–519. https://doi.org/10.1016/j.polymertesting.2018.08.008.

[80] C. Basgul, F.M. Thieringer, S.M. Kurtz, Heat transfer-based non-isothermal healing model for the interfacial bonding strength of fused filament fabricated polyetheretherketone, Addit Manuf 46 (2021) 102097. https://doi.org/10.1016/J.ADDMA.2021.102097.

[81] M. Regis, A. Bellare, T. Pascolini, P. Bracco, Characterization of thermally annealed PEEK and CFR-PEEK composites: Structure-properties relationships, Polym Degrad Stab 136 (2017) 121–130. https://doi.org/10.1016/j.polymdegradstab.2016.12.005.

[82] P. Rendas, L. Figueiredo, M. Geraldo, C. Vidal, B.A. Soares, Improvement of tensile and flexural properties of 3D printed PEEK through the increase of

interfacial adhesion, J Manuf Process 93 (2023) 260–274. https://doi.org/10.1016/J.JMAPRO.2023.03.024.

[83] Apium, PEEK 450 Natural Datasheet, (n.d.). https://apiumtec.com/download/apium-peek-450-datasheet (accessed July 9, 2023).

[84] C. Shemelya, A. De La Rosa, A.R. Torrado, K. Yu, J. Domanowski, P.J. Bonacuse, R.E. Martin, M. Juhasz, F. Hurwitz, R.B. Wicker, B. Conner, E. MacDonald, D.A. Roberson, Anisotropy of thermal conductivity in 3D printed polymer matrix composites for space based cube satellites, Addit Manuf 16 (2017) 186–196. https://doi.org/10.1016/j.addma.2017.05.012.

[85] S.F. Costa, F.M. Duarte, J.A. Covas, Estimation of filament temperature and adhesion development in fused deposition techniques, J Mater Process Technol 245 (2017) 167–179. https://doi.org/10.1016/J.JMATPROTEC.2017.02.026.

[86] S.-Y. Chung, D. Stephan, M.A. Elrahman, T.-S. Han, Effects of anisotropic voids on thermal properties of insulating media investigated using 3D printed samples, Constr Build Mater 111 (2016) 529–542. https://doi.org/10.1016/j.conbuildmat.2016.02.165.

[87] D. Ravoori, L. Alba, H. Prajapati, A. Jain, Investigation of process-structure-property relationships in polymer extrusion based additive manufacturing through in situ high speed imaging and thermal conductivity measurements, Addit Manuf 23 (2018) 132–139. https://doi.org/10.1016/j.addma.2018.07.011.

[88] H. Prajapati, D. Ravoori, R.L. Woods, A. Jain, Measurement of anisotropic thermal conductivity and inter-layer thermal contact resistance in polymer fused deposition modeling (FDM), Addit Manuf 21 (2018) 84–90. https://doi.org/10.1016/j.addma.2018.02.019.

[89] L. Bai, X. Zhao, R.-Y. Bao, Z.-Y. Liu, M.-B. Yang, W. Yang, Effect of temperature, crystallinity and molecular chain orientation on the thermal conductivity of polymers: a case study of PLLA, J Mater Sci 53 (2018) 10543–10553. https://doi.org/10.1007/s10853-018-2306-4.

[90] P. Roudný, T. Syrový, Thermal conductive composites for FDM 3D printing: A review, opportunities and obstacles, future directions, J Manuf Process 83 (2022) 667–677. https://doi.org/10.1016/j.jmapro.2022.09.026.

[91] S.A. Ghodbane, N.S. Murthy, M.G. Dunn, J. Kohn, Achieving molecular orientation in thermally extruded 3D printed objects, Biofabrication 11 (2019) 045004. https://doi.org/10.1088/1758-5090/ab1d44.

[92] W.M.H. Verbeeten, R.J. Arnold-Bik, M. Lorenzo-Bañuelos, Print Velocity Effects on Strain-Rate Sensitivity of Acrylonitrile-Butadiene-Styrene Using

Material Extrusion Additive Manufacturing, Polymers (Basel) 13 (2021) 149. https://doi.org/10.3390/polym13010149.

[93] W.M.H. Verbeeten, M. Lorenzo-Bañuelos, P.J. Arribas-Subiñas, Anisotropic rate-dependent mechanical behavior of Poly(Lactic Acid) processed by Material Extrusion Additive Manufacturing, Addit Manuf 31 (2020) 100968. https://doi.org/10.1016/j.addma.2019.100968.

[94] J. Liu, W. Li, Y. Guo, H. Zhang, Z. Zhang, Improved thermal conductivity of thermoplastic polyurethane via aligned boron nitride platelets assisted by 3D printing, Compos Part A Appl Sci Manuf 120 (2019) 140–146. https://doi.org/10.1016/j.compositesa.2019.02.026.

[95] X. Wang, M. Jiang, Z. Zhou, J. Gou, D. Hui, 3D printing of polymer matrix composites: A review and prospective, Compos B Eng 110 (2017) 442–458. https://doi.org/10.1016/j.compositesb.2016.11.034.

[96] T. Hofstätter, D.B. Pedersen, G. Tosello, H.N. Hansen, State-of-the-art of fiber-reinforced polymers in additive manufacturing technologies, Journal of Reinforced Plastics and Composites 36 (2017) 1061–1073. https://doi.org/10.1177/0731684417695648.

[97] J. Saroia, Y. Wang, Q. Wei, M. Lei, X. Li, Y. Guo, K. Zhang, A review on 3D printed matrix polymer composites: its potential and future challenges, International Journal of Advanced Manufacturing Technology 106 (2020) 1695–1721. https://doi.org/10.1007/S00170-019-04534-Z/FIGURES/19.

[98] L.G. Blok, M.L. Longana, H. Yu, B.K.S. Woods, An investigation into 3D printing of fibre reinforced thermoplastic composites, Addit Manuf 22 (2018) 176–186. https://doi.org/10.1016/j.addma.2018.04.039.

[99] R.R. Fernandes, A.Y. Tamijani, M. Al-Haik, Mechanical characterization of additively manufactured fiber-reinforced composites, Aerosp Sci Technol 113 (2021) 106653. https://doi.org/10.1016/j.ast.2021.106653.

[100] Markforged, Mark Two Datasheet, (n.d.). https://s3.amazonaws.com/mf.product.doc.images/Datasheets/F-PR-2027.pdf (accessed August 20, 2023).

[101] G. Wypych, PA-6 polyamide-6, Handbook of Polymers (2012) 209–214. https://doi.org/10.1016/B978-1-895198-47-8.50069-2.

[102] Markforged, Composites Data Sheet, (2021) 0–1. http://static.markforged.com/downloads/composites-data-sheet.pdf (accessed August 20, 2023).

[103] A.R. Prajapati, H.K. Dave, H.K. Raval, Effect of fiber reinforcement on the open hole tensile strength of 3D printed composites, Mater Today Proc 46 (2021) 8629–8633. https://doi.org/10.1016/j.matpr.2021.03.597.

[104] D. Krzikalla, J. Měsíček, R. Halama, J. Hajnyš, M. Pagáč, T. Čegan, J. Petrů, On flexural properties of additive manufactured composites: Experimental, and numerical study, Compos Sci Technol 218 (2022). https://doi.org/10.1016/j.compscitech.2021.109182.

[105] C. Lubombo, M.A. Huneault, Effect of infill patterns on the mechanical performance of lightweight 3D-printed cellular PLA parts, Mater Today Commun 17 (2018) 214–228. https://doi.org/10.1016/j.mtcomm.2018.09.017.

[106] M.J. Prajapati, A. Kumar, S.C. Lin, J.Y. Jeng, Multi-material additive manufacturing with lightweight closed-cell foam-filled lattice structures for enhanced mechanical and functional properties, Addit Manuf 54 (2022). https://doi.org/10.1016/j.addma.2022.102766.

[107] L. Grigolato, S. Rosso, R. Meneghello, G. Concheri, G. Savio, Design and manufacturing of graded density components by material extrusion technologies, Addit Manuf 57 (2022) 102950. https://doi.org/10.1016/J.ADDMA.2022.102950.

[108] M.J. Prajapati, A. Kumar, S.C. Lin, J.Y. Jeng, Multi-material additive manufacturing with lightweight closed-cell foam-filled lattice structures for enhanced mechanical and functional properties, Addit Manuf 54 (2022) 102766. https://doi.org/10.1016/J.ADDMA.2022.102766.

[109] M.J. Prajapati, A. Kumar, S.C. Lin, J.Y. Jeng, Reducing mechanical anisotropy in material extrusion process using bioinspired architectured lattice structures, Addit Manuf 66 (2023) 103480. https://doi.org/10.1016/J.ADDMA.2023.103480.

[110] F. Dorčiak, M. Vaško, M. Handrik, F. Bárnik, J. Majko, Tensile test for specimen with different size and shape of inner structures created by 3D printing, Transportation Research Procedia 40 (2019) 671–677. https://doi.org/10.1016/j.trpro.2019.07.095.

[111] F. Bárnik, M. Vaško, M. Handrik, F. Dorčiak, J. Majko, Comparing mechanical properties of composites structures on Onyx base with different density and shape of fill, Transportation Research Procedia 40 (2019) 616–622. https://doi.org/10.1016/j.trpro.2019.07.088.

[112] M. Ahmadifar, K. Benfriha, M. Shirinbayan, J. Fitoussi, A. Tcharkhtchi, Mechanical behavior of polymer-based composites using fused filament fabrication under monotonic and fatigue loadings, Polymers and Polymer

Composites 30 (2022) 096739112210824. https://doi.org/10.1177/09673911221082480.

[113] R. Pipalla, J. Schuster, Y.P. Shaik, Experimental Analysis on 3d Printed Onyx Specimens with Honeycomb Infill Structure, Journal of Advanced Materials Science and Engineering 1 (2021). https://doi.org/10.33425/2771-666x.1003.

[114] Z. Ali, Y. Yan, H. Mei, L. Cheng, L. Zhang, Effect of infill density, build direction and heat treatment on the tensile mechanical properties of 3D-printed carbon-fiber nylon composites, Compos Struct 304 (2023). https://doi.org/10.1016/j.compstruct.2022.116370.

[115] J.C. Wang, H. Dommati, S.J. Hsieh, Review of additive manufacturing methods for high-performance ceramic materials, International Journal of Advanced Manufacturing Technology 103 (2019) 2627–2647. https://doi.org/10.1007/s00170-019-03669-3.

[116] M. Dadkhah, J.-M. Tulliani, A. Saboori, L. Iuliano, Additive manufacturing of ceramics: Advances, challenges, and outlook, J Eur Ceram Soc 43 (2023) 6635–6664. https://doi.org/10.1016/j.jeurceramsoc.2023.07.033.

[117] D. Nötzel, T. Hanemann, New feedstock system for fused filament fabrication of sintered alumina parts, Materials 13 (2020) 1–12. https://doi.org/10.3390/ma13194461.

[118] D. Nötzel, R. Eickhoff, C. Pfeifer, T. Hanemann, Printing of zirconia parts via fused filament fabrication, Materials 14 (2021). https://doi.org/10.3390/ma14195467.

[119] C. Tosto, M. Bragaglia, F. Nanni, G. Recca, G. Cicala, Fused Filament Fabrication of Alumina/Polymer Filaments for Obtaining Ceramic Parts after Debinding and Sintering Processes, Materials 15 (2022). https://doi.org/10.3390/ma15207399.

[120] N. Furong, Y. Xiaole, L. Yuanbing, G. Jinyu, L. Peng, X. Zhipeng, Y. Xianfeng, Fused deposition modeling of Si3N4 ceramics: A cost-effective 3D-printing route for dense and high performance non-oxide ceramic materials, J Eur Ceram Soc 42 (2022) 7369–7376. https://doi.org/10.1016/j.jeurceramsoc.2022.08.041.

[121] M. Orlovská, Z. Chlup, Bača, M. Janek, M. Kitzmantel, Fracture and mechanical properties of lightweight alumina ceramics prepared by fused filament fabrication, J Eur Ceram Soc 40 (2020) 4837–4843. https://doi.org/10.1016/j.jeurceramsoc.2020.02.026.

[122] M. Orlovská, M. Hain, M. Kitzmantel, P. Veteška, Z. Hajdúchová, M. Janek, M. Vozárová, Bača, Monitoring of critical processing steps during the production

of high dense 3D alumina parts using Fused Filament Fabrication technology, Addit Manuf 48 (2021). https://doi.org/10.1016/j.addma.2021.102395.

[123] V. Truxová, J. Šafka, J. Sobotka, J. Macháček, M. Ackermann, Alumina Manufactured by Fused Filament Fabrication: A Comprehensive Study of Mechanical Properties and Porosity, Polymers (Basel) 14 (2022) 1–13. https://doi.org/10.3390/polym14050991.

[124] Z. Guan, X. Yang, P. Liu, X. Xu, Y. Li, X. Yang, Additive manufacturing of zirconia ceramic by fused filament fabrication, Ceram Int 49 (2023) 27742–27749. https://doi.org/10.1016/j.ceramint.2023.05.230.

[125] A. Hadian, B. Morath, M. Biedermann, M. Meboldt, F. Clemens, Selected design rules for material extrusion-based additive manufacturing of alumina based nozzles and heat exchangers considering limitations in printing, debinding, and sintering, Addit Manuf 75 (2023) 103719. https://doi.org/10.1016/j.addma.2023.103719.

[126] G. Wang, S. Wang, X. Dong, Y. Zhang, W. Shen, Recent progress in additive manufacturing of ceramic dental restorations, Journal of Materials Research and Technology 26 (2023) 1028–1049. https://doi.org/10.1016/j.jmrt.2023.07.257.

[127] S. Cano, T. Lube, P. Huber, A. Gallego, J.A. Naranjo, C. Berges, S. Schuschnigg, G. Herranz, C. Kukla, C. Holzer, J. Gonzalez-Gutierrez, Influence of the Infill Orientation on the Properties of Zirconia Parts Produced by Fused Filament Fabrication, Materials 13 (2020) 3158. https://doi.org/10.3390/ma13143158.

[128] Tosoh Corporation, Advanced Ceramics: Zirconia Powders., (n.d.). https://www.tosoh.com/ourproducts/advanced-materials/zirconia-powders (accessed July 5, 2023).

[129] D. Nötzel, R. Eickhoff, T. Hanemann, Fused Filament Fabrication of Small Ceramic Components, Materials 11 (2018) 1463. https://doi.org/10.3390/ma11081463.

[130] D. Nötzel, T. Hanemann, R. Eickhoff, Charakterisierung additiv gefertigter keramischer Bauteile via FFF-Verfahren, Keramische Zeitschrift 71 (2019) 56–61. https://doi.org/10.1007/s42410-019-0074-7.

[131] A. Hadian, M. Fricke, A. Liersch, F. Clemens, Material extrusion additive manufacturing of zirconia parts using powder injection molding feedstock compositions, Addit Manuf 57 (2022) 102966. https://doi.org/10.1016/j.addma.2022.102966.

[132] A. Hadian, L. Koch, P. Koberg, F. Sarraf, A. Liersch, T. Sebastian, F. Clemens, Material extrusion based additive manufacturing of large zirconia structures

using filaments with ethylene vinyl acetate based binder composition, Addit Manuf 47 (2021) 102227. https://doi.org/10.1016/j.addma.2021.102227.

[133] N. Travitzky, A. Bonet, B. Dermeik, T. Fey, I. Filbert-Demut, L. Schlier, T. Schlordt, P. Greil, Additive Manufacturing of Ceramic-Based Materials, Adv Eng Mater 16 (2014) 729–754. https://doi.org/10.1002/adem.201400097.

[134] F. Clemens, F. Sarraf, A. Borzì, A. Neels, A. Hadian, Material extrusion additive manufacturing of advanced ceramics: Towards the production of large components, J Eur Ceram Soc 43 (2023) 2752–2760. https://doi.org/10.1016/j.jeurceramsoc.2022.10.019.

[135] L. Morfini, N. Gurrado, Spina R., Effect of process parameters on the thermal properties of material extruded AM parts, in: Italian Manufacturing Association Conference, 2023: pp. 225–231. https://doi.org/10.21741/9781644902714-27.

[136] UNI EN ISO 22007-2:2022 - Plastics - Determination of thermal conductivity and thermal diffusivity - Part 2: Transient plane heat source (hot disc) method, (2022).

[137] U. Hammerschmidt, V. Meier, New Transient Hot-Bridge Sensor to Measure Thermal Conductivity, Thermal Diffusivity, and Volumetric Specific Heat, Int J Thermophys 27 (2006) 840–865. https://doi.org/10.1007/s10765-006-0061-2.

[138] J. Gaiser, M. Stripf, F. Henning, Enhanced Transient Hot Bridge Method Using a Finite Element Analysis, Int J Thermophys 40 (2019) 12. https://doi.org/10.1007/s10765-018-2476-y.

[139] UNI EN ISO 21920:2021 Geometrical product specifications (GPS) - Surface texture: Profile, (2021).

[140] Ö. ÖZDİLLİ, Comparison of the Surface Quality of the Products Manufactured by the Plastic Injection Molding and SLA and FDM Method, Uluslararası Muhendislik Arastirma ve Gelistirme Dergisi (2021) 428–437. https://doi.org/10.29137/umagd.762942.

[141] L. Morfini, M.G. Guerra, F. Lavecchia, R. Spina, L.M. Galantucci, Preliminary test on the effect of direct annealing on additive manufactured PEEK bending properties, Procedia CIRP 118 (2023) 705–710. https://doi.org/10.1016/j.procir.2023.06.121.

[142] Solvay Specialty Polymers USA, KetaSpire ® MS NT1 AM Filament, (2019) 1–2. https://www.solvayamshop.com/ccrz__ProductDetails?sku=Z58-39681 (accessed September 29, 2021).

[143] UNI EN ISO 178:2019 - Plastics - Determination of flexural properties, (2019).

[144] J. Butt, R. Bhaskar, Investigating the effects of annealing on the mechanical properties of FFF-printed thermoplastics, Journal of Manufacturing and Materials Processing 4 (2020) 1–20. https://doi.org/10.3390/jmmp4020038.

[145] UNI EN ISO 527:2019 - Determination of tensile properties, (2019).

[146] UNI EN ISO 18754:2020 - Fine ceramics (advanced ceramics, advanced technical ceramics) - Determination of density and apparent porosity, (2020).

[147] UNI EN ISO 6872:2015 - Dentistry - Ceramic materials, (2015).

[148] ASTM D7984-21 - Standard Test Method for Measurement of Thermal Effusivity of Fabrics Using a Modified Transient Plane Source (MTPS) Instrument, (2021).

[149] S.B. Patel, N. Baker, I. Marques, A. Hamlekhan, M.T. Mathew, C. Takoudis, C. Friedrich, C. Sukotjo, T. Shokuhfar, Transparent TiO 2 nanotubes on zirconia for biomedical applications, RSC Adv 7 (2017) 30397–30410. https://doi.org/10.1039/C7RA03940A.

[150] M.P. Serdeczny, R. Comminal, D.B. Pedersen, J. Spangenberg, Experimental validation of a numerical model for the strand shape in material extrusion additive manufacturing, Addit Manuf 24 (2018) 145–153. https://doi.org/10.1016/J.ADDMA.2018.09.022.

[151] S.M. Cokic, J. Vleugels, B. Van Meerbeek, B. Camargo, E. Willems, M. Li, F. Zhang, Mechanical properties, aging stability and translucency of speed-sintered zirconia for chairside restorations, Dental Materials 36 (2020) 959–972. https://doi.org/10.1016/j.dental.2020.04.026.

[152] H. Nakai, M. Inokoshi, K. Nozaki, K. Komatsu, S. Kamijo, H. Liu, M. Shimizubata, S. Minakuchi, B. Van Meerbeek, J. Vleugels, F. Zhang, Additively Manufactured Zirconia for Dental Applications, Materials 14 (2021) 3694. https://doi.org/10.3390/ma14133694.

[153] Y. Lu, Z. Mei, J. Zhang, S. Gao, X. Yang, B. Dong, L. Yue, H. Yu, Flexural strength and Weibull analysis of Y-TZP fabricated by stereolithographic additive manufacturing and subtractive manufacturing, J Eur Ceram Soc 40 (2020) 826–834. https://doi.org/10.1016/J.JEURCERAMSOC.2019.10.058.

[154] E. Willems, M. Turon-Vinas, B. Camargo dos Santos, B. Van Hooreweder, F. Zhang, B. Van Meerbeek, J. Vleugels, Additive manufacturing of zirconia ceramics by material jetting, J Eur Ceram Soc 41 (2021) 5292–5306. https://doi.org/10.1016/j.jeurceramsoc.2021.04.018.

[155] K.W. Schlichting, N.P. Padture, P.G. Klemens, Thermal conductivity of dense and porous yttria-stabilized zirconia, J Mater Sci 36 (2001) 3003–3010. https://doi.org/10.1023/A:1017970924312/METRICS.